CATÓLICA

UNIVERSIDADE CATÓLICA PORTUGUESA | PORTO

Escola Superior de Biotecnologia

TWO PHOTON POLYMERIZATION-DERIVED MICRO 3D STRUCTURES FOR APPLICATION IN REGENERATIVE MEDICINE

By:

Paulo Jorge Mesquita Queirós Castro Dias

November 2015

CATÓLICA
UNIVERSIDADE CATÓLICA PORTUGUESA | PORTO
Escola Superior de Biotecnologia

TWO PHOTON POLYMERIZATION-DERIVED MICRO 3D STRUCTURES FOR APPLICATION IN REGENERATIVE MEDICINE

Thesis presented to *Escola Superior de Biotecnologia* of the *Universidade Católica Portuguesa* to fulfil the requirements of Master of Science degree in Biomedical Engineering.

By:

Paulo Jorge Mesquita Queirós Castro Dias

Supervisors:

Pamela Habibovic (MIRA, University of Twente)

David Barata (MIRA, University of Twente)

November 2015

This work was done in collaboration with:

University of Twente

UNIVERSITY OF TWENTE.

MIRA – Institute for biomedical technology and technical medicine

MIRA
BIOMEDICAL TECHNOLOGY
AND TECHNICAL MEDICINE

RESUMO

Substratos com topografias artificiais têm demonstrado serem capazes de influenciar o comportamento celular. No entanto, dependendo da aplicação pretendida, a sua fabricação pode ser complexa. De modo a ultrapassar as limitações de tecnologias convencionais, utilizou-se um processo de fotolitografia, capaz de criar objetos 3D a uma escala nanométrica, baseada no conceito de fotopolimerização induzida pela absorção simultânea de dois fotões *(TPP-Two Photon Polymerization)*.

A fase inicial do projeto caracterizou-se pelo desenvolvimento das competências técnicas necessárias. No decorrer do processo de aprendizagem, foram também avaliadas algumas das limitações do sistema, nomeadamente longos tempos de fabrico. De modo a contornar a situação, demonstrou-se a possibilidade de replicar objetos, previamente fabricados por TPP, em polistireno (PS) e ácido poliláctico (PLA), usando para tal um elastómero para criar moldes que permitem produção em massa.

Após uma série de otimizações e alterações de *design*, vários padrões com características, micro (vigas) e nanométricas (traços) assim como topografias baseadas em pilares cilíndricos com diferentes alturas (uniforme: 5µm, 13µm; variável: 3 a 15µm) foram desenvolvidos e replicadas em PS de modo a avaliar o seu efeito na forma e orientação de uma linhagem celular pré-osteoblástica, MG-63.

Os resultados dos substratos com pilares sugerem a existência de um valor limite a partir do qual o tamanho dos pilares induz o alinhamento celular e mudança de forma. Células expandidas durante 72 horas só mostram alterações morfologias em superfícies com estruturas superiores a 6µm tendo adquirido uma forma alongada e orientando-se preenchendo os espaços entre pilares. O padrão das vigas e traços visou avaliar o efeito simultâneo de duas topografias com escalas distintas numa só amostra. A sua análise após 72 horas mostrou uma clara influência das estruturas micrométricas (vigas) e ausência de efeito por parte traços, promovendo o alinhamento celular numa direção paralela às estruturas assim como tendência a formar uma conformação tipo tecido entre as vigas.

Como trabalho futuro foram sugeridas outras possíveis aplicações, nomeadamente a nível de análise de células individuais e estudos de invasão celular. Por fim, testaram-se para uso em TPP, diversas composições de um biopolímero baseado em PLA que teve como resultados mais positivos uma formulação de PLA/NVP (N-vinilpirrolidona) usando 5%Wt. de um fotoiniciador derivado de benzofenona.

ABSTRACT

Patterned surfaces have been shown to be capable of influencing cellular behaviour. However, depending on the intended application their assembly may be a complex process. To overcome the limitations of common fabrication processes, a laser lithography technique based on the two-photon absorption effect, was used to construct several micro and nanostructures.

Initial stages of the project were devoted to developing the technical skills and assessing the limitations of the two photon polymerization (TPP) fabrication process. It was additionally shown, the possibility of mass producing TPP constructs by replicating them, via soft lithography, in polystyrene (PS) and polylactic acid (PLA) imprints, without losing the original geometry.

Following a series of optimizations and design alterations, two classes of patterned surfaces were fabricated, replicated in PS and seeded with a pre-osteoblastic stem cell lineage, MG-63, for 72 hours.

The first class, was developed to explore the effect of micro (beams) and nano (dashes) structures within the same sample. The 72 hour timepoint analysis has shown a significant influence of the micrometric structures (beams), as opposed to the dashes, in inducing cell orientation and migration following a direction parallel to the beams as well as a tendency to form a tissue like conformation in the spaces between beams.

The second class of patterns included two uniform cylinder based pillar topographies, with different heights (low: 5μm and high: 13μm) and a ramp-like structure with variable pillar height (3 to 15μm). Contrary to cells expanded in the smaller pillars, both the high and variable height patterns promoted an elongated shape, with cells orientated across the pillar spaces. The height gradient created by the variable pillars, suggested the existence of a height threshold capable of inducing morphological change, since only cells within the patterned region where pillar height is greater than 6μm, exhibit similar behaviour to the high pillars topography.

As future work, it was also suggested that this fabrication technique may find wide application in single cell analysis and migration studies. Lastly, several custom PLA-based biopolymers were developed\optimized, for two photon fabrication. The best formulation was obtained for a 50/50 ratio of a PLA\NVP (N-vinylpyrrolidone) monomer mixture and 5%Wt. of a Benzophenone derivative photoinitiator.

ACKNOWLEDGEMENTS

I would like to extend my gratitude to everyone that, in some way or another, contributed to the development of this work.

To my supervisor from University of Twente, Pamela Habibovic, for the opportunity to join her research group, and for encouraging the discussion of ideas with an open mind. Thank you also to the other members of the group, for the enjoyable work environment, and support.

To David Barata, my daily supervisor, for the support, availability and for pushing me to think outside the box.

To Huib van Vossen, from University of Twente | MESA+ NanoLab, for the assistance inside the cleanroom and willingness to trade ideas.

To Sébastien Blanquer from department of Biomaterials Science and Technology (BST), University of Twente, for the collaboration opportunity and assistance.

To my fellow students at the master table in Twente University, thank you for all the great shared moments.

To my colleague and roommate in Enschede, Pedro Sousa.

To my classmates from the Master course at Universidade Católica Portuguesa for their enthusiasm and moments together.

To all my friends and family in Portugal, thank you for all the patience and continued support during all these years.

TABLE OF CONTENTS

LIST OF TABLES

LIST OF FIGURES

SYMBOLS AND ABBREVIATIONS

2.5D	Two-and-a-half-dimensional
2D	Two-Dimensional
2PP	Two Photon Polymerization
3D	Three-Dimensional
AFM	Atomic Force Microscope
AOM	Acousto-Optical Modulator
Bio-Polymer	Methacrylate-Poly-Lactic Acid
BSA	Bovine Serum Albumin
CAD	Computer Aided Design
DAPI	4',6-DiAmidino-2-PhenylIndole
ECM	Extra Cellular Matrix
FBS	Fetal Bovine Serum
FITC	Fluorescein IsoThioCyanate
FOTS	Fluoroctatrichlorosilane
fs	Femtosecond
GWL	General Writing Language
h	Plank constant
HMDS	HexaMethylDiSilazane
i	Light intensity
I	Photoinitiator
IPA	IsoPropyl Alcohol
k_d	Rate constant for catalyst dissociation
M	Monomer
MEMS	Micro Electro Mechanical System
MSC	Mesenchymal Stem Cells
NA	Numerical Aperture
NIR	Near Infrared
NSOM	Near-Field Scanning Optical Microscope
NVP	N-vinylpyrrolidone
ORMCER	Organically Modified Ceramics
PBS	Phosphate Buffered Saline
PC	Propylene Carbonate
PDMS	Poly(DiMethyl-Siloxane)
PGA	Poly(Glycolic Acid)
PGMEA	Propylene-Glycol-Methyl-Ether-Acetate
PLA	Poly(Lactic Acid)
PLGA	Poly(Lactic-co-Glycolic Acid)
PS	Poly(Styrene)
PTMC	Poly(trimethylene carbonate
$R^{\cdot}$	Radical
RM	Regenerative Medicine
RP	Rapid Prototyping
S	Energy level
SE	Secondary Electron
SEM	Scanning Electron Microscope
SLA	Stereolithography
STL	Standard Tessellation Language
STM	Scanning Tunnelling Microscope
TPA	Two Photon Absorption
TPE	Two Photon Excitation
TPP	Two Photon Polymerization
TR	Tissue Regeneration
UV	Ultra-Violet
Voxel	Volumetric Pixel
α-MEM	Minimum Essential Medium α
λ	Wavelength
μ-SLA	Microstereolithography
υ	Wave Frequency

INTRODUCTION

1. REGENERATIVE MEDICINE

A number of organs in the human body, possess an innate, albeit limited, ability of self-regeneration in the event of injury[1,2]. The underlying mechanism of this regeneration is not, as of yet, fully comprehended, but has clear therapeutic potential for human applications [3].

When tissue integrity is compromised, a coordinated response is triggered involving cellular components of the immune system, blood coagulation factors and inflammatory pathways. These mechanisms, enhance recovery and ensure homeostasis restoration by promoting cell proliferation, differentiation and migration[4,5]. Notwithstanding the complexity of the wound repair process, uncontrolled and malignant transformation of these cells is a rather uncommon event[6].

Following injury or degeneration, recovery is possible via two processes: scar formation and regeneration. The first, is characterized by the substitution, of once functional tissue, by a patch of cells (mainly fibroblasts) and disorganized extracellular matrix (mainly collagen) to re-establish continuity of the injured organ[2,7]. The second, involves recreating the injured organ, by reactivating the developmental pathways that originally led to its creation[7]. This ability to completely recreate complex structures is present in some lower species and (to a limited extent) in human foetus, but it is lost during adult life[2,8].

Understanding how complex regeneration occurs in nature, entails knowledge from different technological areas. Thus, by combining cell transplantation, tissue engineering (TE) and stem cell biology under one unifying concept - regeneration of living tissues and organs - the regenerative medicine (RM) field emerged[9].

2. TISSUE ENGINEERING

As one of the major components of regenerative medicine, the tissue engineering (TE) field studies non-mammalian and human development, using tools from cell biology, genetics, materials science and bioengineering, to restore, replace or regenerate the reparative pathways of defective tissues[2,10–12]. This may be achieved either by,

injecting functional cells into a non-functional site to stimulate regeneration and/or employing biocompatible materials (biomaterials) to create new tissues and organs[13,14].

Current efforts to improve and increase therapeutic options, rely on using a diversity of biomaterials and stem cells. However, apart from a few cases of successful clinical application[9,14–17], modern TE technologies still face several limitations[16,18,19]. Amongst them, the inadequate understanding of the underlying biological mechanisms, technical problems (*i.e.* large scale expansion of, exogenously manipulated, stem cells) and also regulatory issues regarding costs and safety[20].

2.1. CELL TYPES FOR TISSUE ENGINEERING APPLICATION

In many tissues/organs, such as the hematopoietic system, intestine, and epidermis, cells have a short life span and rely on stem and progenitor cells for continuous homeostatic maintenance (or tissue turnover) and tissue repair/regeneration[21].

Given their unique regenerative abilities, stem cells possess the potential for treating many diseases such as diabetes[22], and heart disease[23]. However, cell-based techniques aimed at tissue and organ replacement are hindered by the inherent difficulty of growing specific cell types in large quantities. Many loose critical phenotypic traits with increasing time in culture, however, advances in cell biology have allowed the discovery of culture conditions that favour the proliferation of cells *in vitro* under conditions that allow maintenance or recovery of cell phenotype[10].

2.1.1. STEM CELLS AND OTHER PLURIPOTENT CELL TYPES

Stem cells are distinguished from other cell types by two important characteristics. They are unspecialized cells capable of self-renewal (through cell division) and under certain physiologic or experimental conditions, are capable of differentiation into tissue or organ-specific cells[24].

There are two main types of stem cells, embryonic and non-embryonic. Embryonic stem cells are blastocyst derived with the potential to develop into cells and tissues of the three primary germ layers: ectoderm, mesoderm and endoderm[25].

Within non-embryonic stem cells, fetal stem cells are derived from the amniotic fluid or umbilical cord tissue and adult cells may originate from different body tissues. These stem cell types are mainly multipotent and thus have a limited ability to differentiate[9,25].

However, it is possible to reprogram adult somatic cells to an embryonic-like state by transfer of nuclear contents into oocytes or by fusion with embryonic stem (ES) cells. These cells, designated as induced pluripotent stem cells (iPSCs), exhibit the morphology, growth properties and express cell marker genes of embryonic stem cells [23,26,27].

2.1.2. NATIVE PROGENITOR CELLS

Typically, stem cells generate an intermediate cell type or types before they achieve a fully differentiated state. Native targeted progenitor cells, also known as primary cells, are tissue-specific, unipotent cells, already programmed to become a specific cell type which can be expanded and used in the same patient without rejection, in an autologous manner[25].

This limited differentiation ability however may not be as irreversible as once thought since it has recently been shown that it is possible to reprogram them into a multipotent state (iMPC- induced multipotent progenitor cells)[28,29].

It is often difficult to distinguish adult, tissue-specific stem cells from progenitor cells. However there are certain key differences between them[30]:

Table 1 – *Main distinctive characteristics between adult stem cells and progenitor cells.*

Characteristics	Adult Stem Cell	Progenitor Cell
Self-renewal in vivo	Unlimited	Limited
Self-renewal in vitro	Unlimited	Limited
Potentiality	Multipotent\ Pluripotent	Unipotent\ Multipotent
Maintenance of self-renewal	Yes	No
Population	Reaches maximum number of cells before differentiating	Does not reach maximum population

Using stem cell based research possesses numerous advantages over primary cells such as scalability, stability, purity, reproducibility and others. While certain experimental demands may only be met by the use of primary cells, the advantages of stem cell derived cells for understanding basic biological processes are clear, however the choice of which type to use dependent on the question being asked[31].

2.1.3. PLASTICITY

Several ideas have been put forward to explain stem cell lineage determination. One current line of research is focused on the stem cells 3D microenvironment, or niche,

which is thought to influence/control genes and properties that define "stemness" of the stem cells [32]. Additionally, several studies have shown that differentiated adult cells are capable can be converted into another cell lineage when implanted into a different niche, potentially differentiating into cell types similar to those found in the new environment. This phenomenon is referred to as plasticity or transdifferentiation[33].

Stem cell differentiation may be induced in the presence of the appropriate culture medium, containing growth factors and cytokines. However, these soluble factors and factor-mediated signalling pathways do not explain all the mechanism leading to lineage and fate determination[34,35].

It was shown that stem cells are able to sense, transduce, and respond to stimuli such as shear stress[36], mechanical strain[37], matrix topography[38], and rigidity[39]. This led to a shift on research areas to focus not only on chemical factors but also on the physical cues provided by the cells microenvironment[40]. This includes signalling molecules, inter-cellular contact and the interaction between stem cells and their neighbouring extracellular matrix[41,42].

The mechanism through which a living organism responds to its mechanical environment, *e.g.* physical force and hemodynamic shear stress is referred to as mechanotransduction[43,44]. While responses in stem cells vary, these processes typically modulate fundamental behaviours of stem cells including lineage regulation.

Despite the significance of these interactions in fundamental developmental biology and the biomedical applications such as stem cell therapy, their widespread incorporation in biological techniques is limited, and comprehension of the mechanism of mechanotransduction still remains poorly understood. However, with the establishment of microscale fabrication technologies and new materials it is possible to create a more accurate and controlled biomechanical environment and therefore investigate the effect of biomechanical regulation in stem cells[30,43]

3. BIOMATERIALS

Apart from blood cells, most, if not all other, normal cells in human tissues, are anchorage-dependent and reside in a solid matrix known as extracellular matrix (ECM). In tissue engineering, biomaterials can be used to replicate the biologic and mechanical function of this matrix, providing a three-dimensional space for cells to attach, grow and

respond to bioactive cues\signals and migrate forming new tissues with appropriate structure and function[9,45].

These biomimetic ECM structures, known as scaffolds, are typically comprised of polymeric biomaterials and can generally be divided into three classes: synthetic polymers, such as polylactic acid (PLA), polyglycolic acid (PGA) and their copolymer, poly(lactic-*co*-glycolic acid) (PLGA)[46,47] ; naturally derived materials, such as collagen and alginate[48,49] and finally decellularized tissues matrices[9,50].

Each class of biomaterial has its own merits. The use of synthetic polymers as matrices and templates have the advantage of large scale reproducible production with controlled properties of strength, degradation rate, and microstructure[51,52]. However, naturally derived materials and acellular tissue matrices have the potential advantage of biologic recognition. Furthermore, acellular tissue matrices are of particular interest when attempting to recreate vascular networks capable of nutrient and gas exchange[53]. Using decellularization protocols, it is possible to develop models for simple systems such as blood vessels[54,55], urinary bladder[56] and trachea[56]. Even larger, more complex models such as heart[56–58], lung[59–61], liver[53,62,63] and kidney[64–68], have been applied to pre-clinical *in vivo* studies using small animal models.

Even though the technology to fully regenerate a tissue, that does not already possess the capability to spontaneously regenerate (*e.g.* bone), or to produce complex organs *de novo*, is not yet available[69], it is still possible to enhance the body's innate regeneration ability by replacing sections of tissue[70,71].

4. SCAFFOLD BASED TISSUE REGENERATION

The current strategy for tissue engineering typically entails the *ex vivo e*xpansion of multipotential cell populations, followed by their transplantation into damaged areas[72].

In this regard, *in vitro* tissue screening still plays a pivotal role supplying valuable insight to not only the structural organization but also the cellular and molecular composition of a native tissue. It is of particular importance to study the interactions of cells with absorbable matrices (cell proliferation and biosynthesis of matrix molecules) and environmental factors required for tissue formation[73].

Cell expansion in 3D environments assumes the use of ECM (extracellular matrix) biomimetic scaffolds, acting as space-holders to prevent intrusion of tissues from the immediate vicinity into the affected site. They also provide a temporary support

structure for the tissue that they are intended to replace[74]. Fabrication of scaffold structures that can facilitate cell-matrix interactions is not only crucial for cellular growth behaviour, but is also a critical prerequisite for the success of engineering physiologically functional tissues[9,74].

4.1. SCAFFOLD FABRICATION PROCESSES

Given the importance of the role played by biomimetic ECM structures, it is not surprising that some of the most important technological advances are the ones been made regarding their fabrication processes[10]. A wide variety of 3D scaffold fabrication technique are readily available and can be classified into two main categories: conventional techniques and rapid prototyping (RP) methods, based on the micro-architectures they create[75].

Conventional processes usually create scaffolds with a continuous, uninterrupted pore network and include techniques such as: particulate leaching[76–79], gas foaming[78–81], fibre networking[82,83], phase separation[84,85], melt moulding[86,87], emulsion freeze drying[88,89], solution casting[90,91], freeze drying[92–94], and combinations of those.

Still, these techniques lack precise control over pore size, interconnectivity, porosity and spatial distribution within the scaffold as well as heterogeneous mechanical strength and difficulty in manufacturing patient specific implants (control over external geometry is limited)[75,95]. Additionally, because of their fabrication process, they usually have a limited ability to incorporate cells and proteins as they are normally implemented under harsh conditions such as high temperature or in the presence of organic solvents[75].

4.1.1. RAPID PROTOTYPING

To overcome the disadvantages of traditional methods, Rapid Prototyping, has been introduced to facilitate the fabrication of customized three-dimensional scaffolds. These constructs are usually assembled using computer-aided design (CAD) technology to control the shape, internal architecture and to systematically deposit biomaterial/cells in a layer-by-layer fashion.

Every technique has a lower technical limit for the size of its smallest reproducible detail (*i.e.* resolution). That said, there is usually a clear relationship between structure size and feasibility, the higher the resolution of the smallest details, the smaller will be its maximum object size[96].

The following table represents an overview of common RP techniques for biomedical applications, classified according to three working principles: nozzle-based, printer-based and laser-based systems[97]:

.**Table 2 -** *Rapid prototyping techniques overview for Tissue Regeneration*

Technology	3D mechanism	Material state	Resolution	References
Nozzle based				
Fused deposition Modelling	Cool to solidify	Semi-molten	250-1000µm	98–100
Precision Extrusion Deposition	Cool to solidify	Semi-molten	-	101,102
Precision Extrusion Manufacturing	Cool to solidify	Semi-molten	-	103
Multiphase Jet Solidification	Cool to solidify	Semi-molten	200mm	104–106
3D Fibre Deposition	Cool to solidify	Semi-molten	-	107,108
Pressure Assisted Micro-Syringe	Solvent evaporation	Liquid	7-500mm	109
Low Temperature Deposition Modelling	Lower temp. frozen	Slurry	300-500µm	110,111
Multi-Nozzle Deposition Manufacturing	Lower temp. frozen	Liquid	300-500µm	112,113
3D-Bioplotter	Moisture curing	Colloid	45-1600µm	114
Direct Ink Writing	High yield stress	Slurry	5-100µm	115
Printer based				
3D-PrintingTM	Crosslink	Liquid, paste	100µm	116
Inkjet printing	Crosslink	Liquid	50-250µm	117–119
Laser based				
Selective Laser Sintering	Material fuse	Solid	-	100,120
Stereolithography	Photopolymerization	Liquid	30µm	100,121
Micro-Stereolithography	Photopolymerization	Liquid	1µm	97,122,123
Two photon polymerization	Photopolymerization	Liquid	<100nm	-

NOZZLE-BASED SYSTEMS

Nozzle-based systems are very diverse and can either be heat-independent or melting processes. They allow fabrication using computer assisted deposition of material and the dimensions of the finished object are only dependent of material viscosity, deposition speed, tip diameter and the applied pressure. These were specifically developed to produce scaffolds for soft tissue engineering thus allowing the system to process thermally sensitive bio-components and even cells[124].

PRINTER-BASED SYSTEMS

Printer-based systems implement inkjet technology as a scaffold manufacturing technique. They can either be drop-on-demand, where individual droplets are controlled, or continuous ejection types. In this mode, “ink” is continuously deposited from a nozzle under pressure, the jet then breaks up into a train of droplets whose direction is controlled by electrical signals[125]. Like the nozzle-based systems, building a construct occurs in an additional computer-controlled layer-by-layer sequence with deposition of material.

They include techniques that allow fabrication of parts in a wide variety of materials, including ceramic, metal and metal-ceramic composite as well as various polymers.

LASER-BASED SYSTEMS

Unlike the nozzle- and printer-based systems that sequentially deposit materials, in this subclass, parts are built from photocurable materials undergoing a photopolymerization process.

Stereolithography (SLA) is one of the most commonly used technique in this subset and uses a computer controlled laser, capable of XY-movement and a fabrication platform (for vertical plane movement), to cure several types of photosensitive materials[100,121]. These systems have been commercially available since the late 80's and allow the creation of 3D parts with resolution down to approximately 30 micrometres[97]. Although sufficient for industrial design, this restricted miniaturization usually precludes fabrication of more advanced micro and nanostructures for tissue engineering applications[126]. To overcome this limitation, microstereolithography (μ-SLA) was introduced in 1993, allowing fabrication processes capable of building, very accurately (~1μm), objects of several cubic centimetres[97,122,123].

In 2009, NanoScribe (GmbH Germany) released a commercial μ-SLA apparatus based on two photon polymerization.

5. TWO PHOTON POLYMERIZATION (TPP)

Two photon-polymerization (TPP or 2PP) is a laser-based fabrication technique that uses the effect of two photon absorption (TPA) to trigger a polymerization reaction, of a photosensitive material, in order to fabricate three-dimensional structures[127,128]. It offers unique advantages, when compared with other methods, as it has no topological constraints and is capable of achieving sub-diffraction limit resolutions, to create reproducible micro/nano-sized objects, with feature sizes of less than 100nm[129].

5.1. TWO PHOTON ABSORPTION

The first scientific reports of multiphoton absorption induced photopolymerization date more than fifty years[130]. However, it was with the work by Kawata et al., (1997) and other fundamental experiments[131–133], that two photon polymerization was regarded as an established fabrication technique for 3D micro-structure fabrication.

The two photon absorption (TPA) effect is a nonlinear optical process, first predicted by Maria Göppert-Mayer (1931) in her doctoral dissertation[134]. However,

experimental confirmation was only possible 30 years later by Kaiser and Garret (1960)[135], after the invention of laser.

The effect is based on the assumption that a molecule can reach an excitation state by either absorption of one photon (of energy $h\upsilon$) or by the simultaneous absorption of two photons ($h\upsilon_1, h\upsilon_2$), each having half the energy required for the transition, as seen on equation 5.1-1, where h is the plank constant and υ frequency.

$$h\upsilon = \frac{1}{2}h\upsilon_1 + \frac{1}{2}h\upsilon_2 \qquad (5.1\text{-}1)$$

5.1.1. ONE PHOTON EXCITATION

When at ground state (S_0), a fluorophore can be excited into a higher energy level (S_1) by absorbing one photon. After a short period of time, it will relax back to its fundamental state by emitting a photon of light. To efficiently excite the fluorophore, the excitation photon should have a wavelength (λ_{1p}) that corresponds to an energy which matches the energy of the excited state of the fluorophore (E_{S1})[136].

5.1.2. TWO PHOTON EXCITATION

Two-photon excitation is accomplished by simultaneous absorption of two photons during a single event. Each photon has half the energy as in the corresponding single-photon absorption event[137].

The energy of a photon is inversely proportional to its wavelength, therefore in two-photon excitation, the photons should have a wavelength (λ_{2p}) of approximately twice that of the photons required to achieve an equivalent transition under one-photon excitation.

A fluorophore absorbing light at 390nm can be excited by two simultaneous photons at approximately 780nm (Figure 1). The resulting excited state from which emission occurs is the same singlet state as that excited during conventional one-photon absorption. Thus, the fluorescence emission after two-photon excitation is exactly the same as that generated in normal one-photon excitation[136,138].

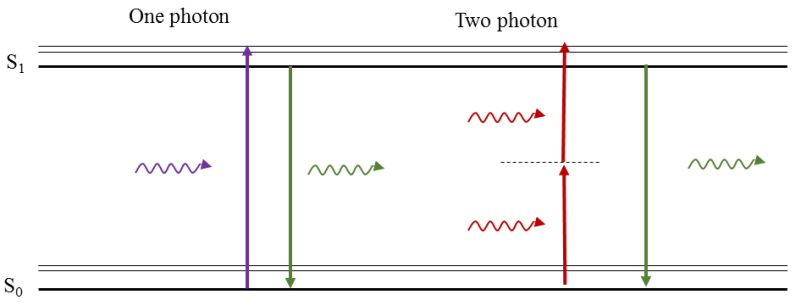

Figure 1- Jabłoński diagram of one-photon excitation (left) and two-photon excitation (right). In each case, the absorption of photon(s) generates an excited state from which the molecule can relax by emitting a fluorescent photon.

The probability of ***n***-photon absorption is proportional to the n^{th} power of the photon flux density. As a result, while the rate of single-photon absorption scales linearly with intensity, i, of the incident radiation, the rate of TPA scales quadratically[139].

To achieve significant probability of absorption, the two photons should be incident on the fluorophore almost simultaneously, i.e. $\sim 10^{-18}$s. This requires a much higher photon flux ($\sim 10^{6}$ times more) than one-photon excitation which is achieved by tight focusing of an ultra-short pulsed laser source rather than a high powered continuous wave laser. The shorter the pulse, the greater the concentration of photons in time and thus the higher the peak power when compared to the average power. This allows for significant probability of two-photon absorption occurring while still maintaining low incident power[126,136–138].

5.1.3. ONE PHOTON VS. TWO PHOTON POLYMERIZATION

Figure 2 illustrates the different photon absorption per transverse section of a focused laser beam, in one-photon (dashed line) and two-photon (continuous line) photon.

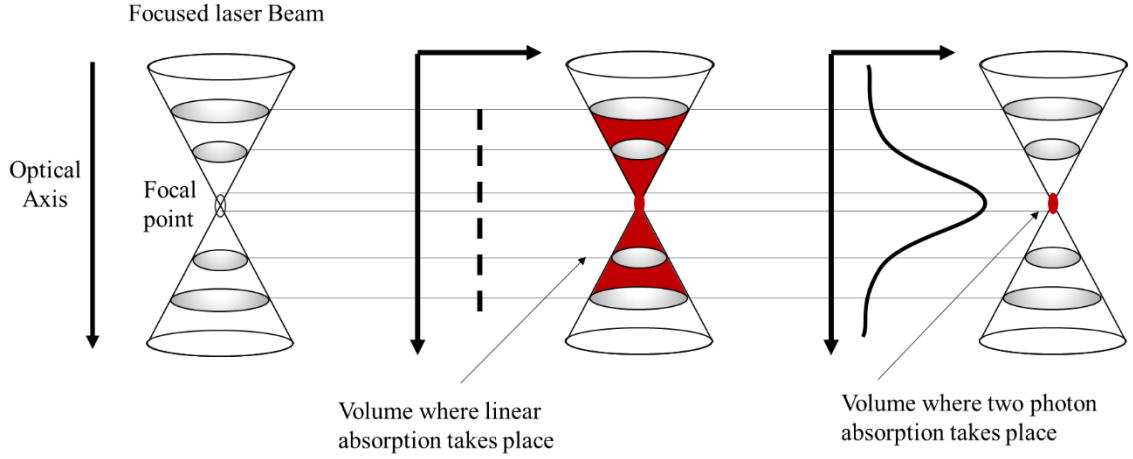

Figure 2- Integration of the intensity (- - -) and intensity square (——) in each transverse section of the focused laser beam along the optical axis. While the probability of one photon absorption is always the same, for two photon polymerization absorption is highest at the focal point.

Single photon excitation has a linear response and therefore the absorption probability is the same along the optical axis. As a result, the absorbing molecules are inadvertently excited outside the focal point which result in a decreased resolution. Conversely, in two photon absorption, given its quadratic dependency, sufficient photon flux density is only achieved within the focal point, where the absorption reaches a maximum. This ensures an enhancement in resolution since the only molecules reacting are located within the focal point[140].

5.2. PHOTORESIST

Two photon polymerization and other light based lithography techniques, require the use of photosensitive materials known as photoresists (also designated as resists or resins) to create an object. They are mainly composed of monomers (or oligomers) and photoinitiators. Additionally, other components can be added, such as inhibitors, to prevent uncontrolled polymerization (*e.g.* during storage), or photosensitizers to improve the resin's sensitivity to specific wavelengths and dyes[126,140,141].

The solubility change of photoresists is a fundamental part of the lithographic process. As such, they can be classified in two types: positive or negative. The following schematic illustrates the differences generated by using positive or negative resists during a photolithography process:

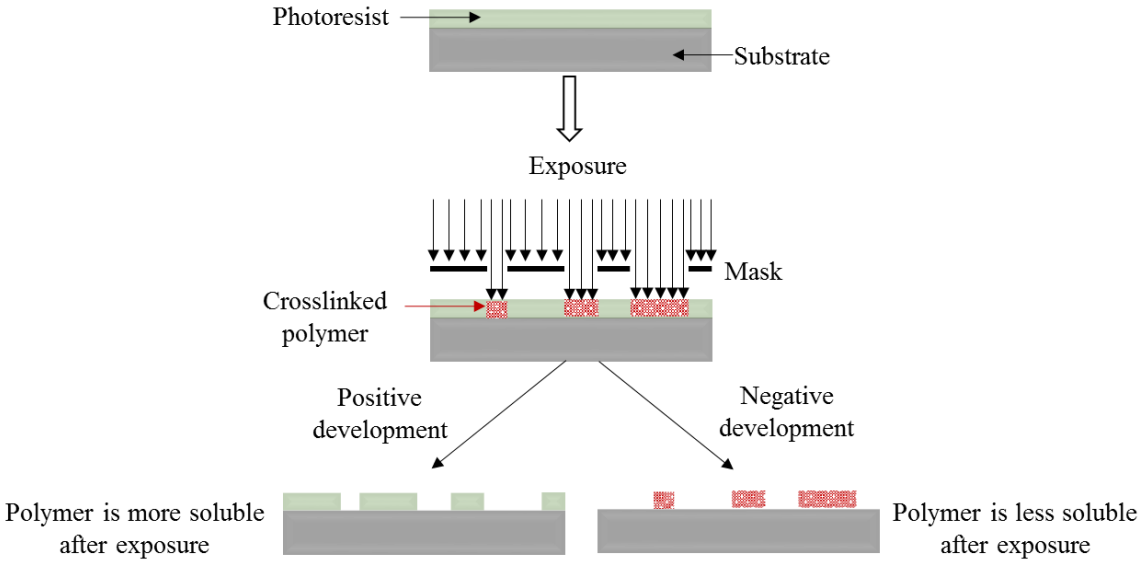

Figure 3 - Schematic representation of masked photolithography fabrication using positive or negative photoresists. Positive resists become more soluble after exposure and exposed areas are easily removed by a solvent resulting in a structure with the same features as the mask. Alternatively, negative toned resists become crosslinked upon exposure and are therefore less soluble, unexposed areas of resists are soluble and are washed away by a developer agent, the final structure is the opposite of the mask.

For positive resists, the photochemical reaction triggered by energy exposure, causes the unprotected areas (gaps in the photomask, Figure 3) to become more soluble thus easily removed by development or rinsed away. Since the protected areas do not undergo polymerization, the final object is comprised of the original photoresist. Conversely, upon irradiation, negative toned resists undergo cross-linking which lowers their solubility and allows for the unexposed material to be dissolved or rinsed away[142]. Despite being an inherently maskless process, this concept still applies to TPP which commonly employs epoxy or acrylate-based negative photoresists.

Some commercially available epoxy-based resists include SU-8® or CAR44® and acrylate formulations such as ORMCER® (Organically modified Ceramics), SR500® (JSR, Japan), or NanoScribe's IP resists are amongst the most used[143,144].

For applications in which empty volumes such as 3D tubes, tunnels or moulds are required, *e.g.* microfluidics, positive photoresists such as the AZ® series (AZ Electronic Materials) may be used[145].

Two photon fabrication is by no means limited to commercially available resists and most often, "in-house" prepared formulations are used in order to better suit the researchers need and it is even possible to use moulding and casting techniques for replication into other materials of interest[141].

5.2.1. MONOMERS

Acrylates are one of the most common resins for TPP due to their large range of commercially available formulations, with different functionalities, sizes, and compositions[146]. Furthermore, given their high polymerization rate, via radical mechanism, they allow for fast polymerization speeds, which are essential in order to decrease processing times. Other reported materials include hydrogels [147], siloxanes[148], and organic/inorganic hybrids[149,150].

The characteristics of the final polymer may be controlled by changing the monomer, or the mixture of monomers, used in the resin. Also, for applications that require liquid resists, solvents are also added to the composition which allow control over viscosity and resist thickness (by wet spinning processes). For example, to control polymer hardness and amount of shrinkage, it is possible to use highly branched monomers incorporating cyclic structures. These kinds of monomers produce highly

cross-linked solid polymers that can easily withstand the development step after fabrication without swelling and therefore losing mechanical structure[151].

Additionally, it is possible to further tailor specific properties of the produced microstructure by doping the base resin with different compounds, therefore changing the physical, chemical, biological and optical properties of the final microstructure.

5.2.2. PHOTOINITIATORS

A photoinitiator is a chemical compound that decomposes upon irradiation, by converting absorbed light energy, into chemical energy in the form of reactive species which will initiate a polymerization reaction[152].

Three main groups of initiators can be distinguished: radical, which yield free radicals upon decomposition, ionic which creates ions and a third group capable of forming both free radicals and ions. The type of photoinitiator used depends on the monomer type used in resin preparation[153].

5.3. PHOTOPOLYMERIZATION

Photopolymerization is a conversion process of unsaturated molecules, in the liquid state, into solid macromolecules using light (UV, visible or infra-red) to trigger chain, or step polymerization reactions[153].

Inducing a photopolymerization reaction, requires materials with a sufficiently high efficiency of initiation (quantum yield). Monomers and oligomers however, have inherently a low quantum yield value (*i.e.* molecules converted per absorbed photon). As a result, in order to initiate a reaction, it is necessary to supplement the material with light sensitive molecules such as photoinitiators[128].

Depending on initiator choice, the polymerization reaction may be triggered by different mechanisms, however, the majority of applications in TPP are usually initiated by free radicals[152] and undergo a chain-growth polymerization process, as seen on equation 5.3-2. Here, M is the monomer or oligomer unit, and M_n, the macromolecule containing n monomer units:

$$M \overset{M}{\rightarrow} M_2 \overset{M}{\rightarrow} M_3 \cdots M_{n-1} \overset{M}{\rightarrow} M_n \qquad (5.3\text{-}2)$$

5.3.1. FREE RADICAL FORMATION PROCESS

Radical chain polymerization is a chain reaction consisting of a sequence of three steps— initiation, propagation, and termination.

The initiation stage is considered to involve two reactions. Firstly, upon irradiation, the photoinitiator (I) is decomposed (usually by homolytic dissociation) to yield a pair of radicals ($R\cdot$):

$$I \xrightarrow{kd} I^* \rightarrow 2R\cdot \qquad (5.3.1\text{-}3)$$

Where k_d is the rate constant for the catalyst dissociation. The second part of the initiation, involves the addition of the formed radical to a monomer molecule to produce the chain initiating radical M_1

$$R\cdot + M \xrightarrow{ki} RM_1\cdot \qquad (5.3.1\text{-}4)$$

During the propagation phase, successive additions of large numbers of monomers to M_1 results in the growth of the chain initiating radical. Each addition creates a new radical that has the same identity as the one previously, except that it is larger by one monomer unit. The successive additions may be represented by:

$$RM_1\cdot + M_n \xrightarrow{ki} RM_{n+1}\cdot \qquad (5.3.1\text{-}5)$$

In chain polymerization, monomers react only with the propagating reactive centre, not with other monomers, and chain addition ceases when the active species are depleted by a number of termination reactions. At this termination stage, two radicals react with each other by combination (coupling) or, more rarely, by disproportionation which results in the formation of two polymer molecules, one saturated and one unsaturated.

$$RM_n\cdot + RM_m\cdot \xrightarrow{\text{(Combination)}} RM_{m+n}R \qquad (5.3.1\text{-}6)$$

$$RM_n\cdot + RM_m\cdot \xrightarrow{\text{(Disproportionation)}} RM_m + RM_n \qquad (5.3.1\text{-}7)$$

The molecular weight of chain polymers increases rapidly during polymerization and typical monomer to polymer conversion rates range between 70% and 90%[126,128,152–154].

There are many commercially available radical photoinitiators, some of the most common are the Irgacure® series[155].

5.4. PRINCIPLES OF TPA LASER LITHOGRAPHY

A typical TPP lithography system consists of a femtosecond laser source with high repetition rate, an attenuator for controlling the laser intensity, the focusing optics and translation stages and an acousto-optical modulator (AOM), to control radiation on/off regimes. A simple representation is illustrated at figure 4:

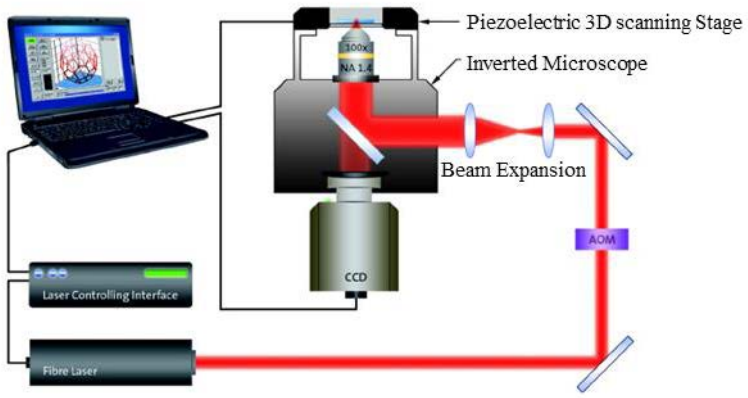

Figure 4 - Schematic of a typical setup for two photon polymerization (2PP) processing. Femtosecond (fs) laser pulses are focused into a volume of the photosensitive resin. The structures are fabricated by moving the laser focus in the xyz plane using a set of linear positioning stages, allowing the sample to be positioned within any 3D position. AOM: Acousto-optical modulator. Image from NanoScribe operational manual[181].

A pulsed near-infrared (NIR) laser is guided into an inverted microscope and tightly focused into a light sensitive resist. Substrate movement in all three spatial dimensions is assured by means of a motorized coarse stage (xy-stage) and a piezo stage (piezo) for fine positioning which enable polymerization along arbitrary trajectories in 3D space.

5.4.1. VOXEL FORMATION, RESOLUTION AND DIFFRACTION LIMIT

During TPP, crosslinking mainly occurs in the region with the highest concentration of radicals. This corresponds to the central part, of the square light intensity distribution, at the focal plane and induces the formation of volume elements with an ellipsoid shape, *i.e.* voxel (Figure 5). These volumetric pixels are the "building blocks" of any structure since it is their precise positioning and overlapping that yield the desired final result. As such, the resolution (*i.e.* ability to distinguish the shape and size between two elements) of TPP systems is limited by voxel dimensions.

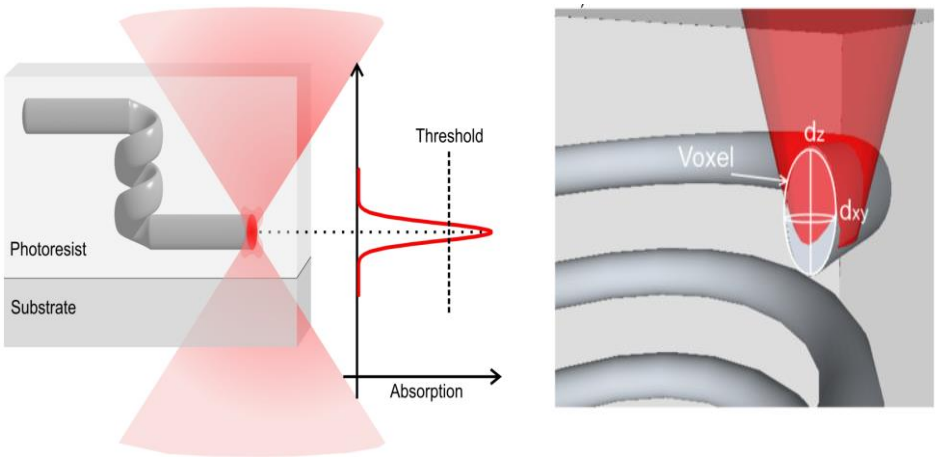

Figure 5 – (Left): Representation of a voxel. (Right): Illustration of the voxel ellipsoid shape. Left image from NanoScribe user manual[181] *. Right image from Jipa et al (2013)*[205].

For optical instruments, the resolution is proportional to the size of its objective, and inversely proportional to the wavelength of the light being observed. Theoretically, the highest resolution that can be achieved by a focusing light microscope before light starts scattering, may be estimated by Abbe's diffraction limit[156]:

$$difraction\ limit = \frac{\lambda}{2NA} \qquad (5.4.1\text{-}8)$$

Where λ is the laser wavelength and NA is the numerical aperture of the focusing objective. From this relationship, shorter wavelengths or larger NA may increase resolution, however, in regards to conventional optical systems, it also means that the diffraction limit cannot be circumvented.

Several devices exist that, alongside TPP, are capable of overcoming the diffraction limit. These include atom, electron or ion waves and also non-light patterning techniques, as scanning tunnelling microscopes (STMs)[157], atomic force microscopy (AFM)[158] and near-field scanning optical microscopy (NSOM)[159]. These systems are capable of achieving very low features (tens of nanometres), however, they mainly used for surface and not in-volume patterning.

For TPP the diffraction limit can be circumvented, since the photochemical processes responsible for the formation of voxels have a threshold response to light excitation. In this case, the diffraction limit becomes just a measure of the focal spot size, it does not put any actual restraint on voxel sizes. According to equation 5.4.1-8, if an 800nm wavelength laser source (NIR region) were to be focused through a 1.4 NA objective, the diffraction limit should be approximately 285nm. However, this theoretical

limitation has been easily surpassed since fabrication of voxels with transverse dimension as small as 30nm, have already been achieved[160–162].

5.5. APPLICATIONS AND LIMITATIONS OF TPP

A brief overview of some of the most common research areas employing TPP is presented in Table 3.

Table 3 - *Overview of various possible application areas for TPP fabrication.*

Field	Description	References
Optics		
Photonic crystals	Photonic crystals and metamaterials allow moulding the flow of light as well as controlling the dynamics of photons.	163,164
Photonic Surfaces	Applications include diffractive optical elements (DOEs), gratings, metamaterials, optical security labels and biomimetics.	165,166
Optical interconnects	Wire bonds to bridge the gap between nanophotonic circuits on different chips.	167,168
Mechanical	Development of generic mechanical microstructures such as cantilever beams, bridges, springs and structures with movable parts such as gears or windmills.	169,170
Microfluidics	Integration of sub-micron scaled three-dimensional elements into microfluidic channels to create filtration systems, stirrers, microfluidic valves or optical elements for lab-on-a-chip systems.	171,172
Biology		
Protein Crosslinking	Characterization of cell adhesion and spreading on linear patterns created on crosslinked matrix molecules and inside living cells.	173,174
Biomedical scaffolds	Artificial extracellular matrix for tissue engineering applications such as study of cell migration and differentiation.	175–177

Notwithstanding the extensive range of possible application in fields such as micro and nanophotonics, micro-electromechanical systems (MEMS), microfluidics, biomedical implants and microdevices, it has as of yet to be applied to manufacturing and it is used mainly for research. Several factors hinder the transition to widespread industry application. Slow speed and small processing volume, high costs of femtosecond lasers, positioning systems and optics as well as the lack of specially designed materials with good optical, mechanical and biomedical properties[178].

However, many of these issues are being resolved, and TPP is transforming from a research to a production tool. In recent years, considerable progress has been made in improving the reliability and reducing the cost of femtosecond laser oscillators and laser systems as well as improving fabrication speeds to match other industry used techniques[178].

6. MOTIVATION AND GOALS

Cells response to nano-topographical has been linked to control of cell phenotype, most notably with human MSC differentiation.

Given the fabrication limitations of early micro and nano fabrication techniques, initial studies focused on highly ordered nano-scale patterns, which typically resulted in lower cell adhesion. On the other side, the use of randomized surfaces, such as nano-scale roughness, have had conflicting results with both positive and negative reports on in vitro adhesion and in vivo implant integration. Following an intermediate approach (between highly organized and completely random), work by Dalby et al., (2007)[179] has shown that patterned surfaces exhibiting controlled nano-disorder were able to induce rapid osteogenesis from skeletal stem cells with similar efficiency to chemical stimulation[180].

The concept of using complex geometries to induce\instruct cell behaviour is an area where two photon based fabrication may excel, since it is capable of restraint free 3D fabrication at nano-scale. As such, the main objectives of this project can be divided into three main parts. First, develop a working knowledge of the 3D photolithography system, its fabrication process and technical limitations. Second, design and fabricate micro\nano patterns and study their influence on stem cell behaviour, such as orientation and shape. Third, develop alternate structures and patterns for single cell analysis and migration studies and finally and test\optimize a custom PLA-based biopolymer for TPP applications.

MATERIALS AND METHODS

7. MICROFABRICATION MATERIALS

Photocrosslinkable resins IP-L 780, IP-G 780 (NanoScribe GmbH), and methacrylate poly-lactic acid (in-house prepared) bio-polymer were used without further processing. Developer agents include isopropyl alcohol (IPA), propylene-glycol-methyl-ether-acetate (PGMEA) and propylene carbonate (PC). For soft lithography procedures, polydimethylsiloxane (PDMS, Sylgard 184 elastomer, Dow Corning, USA), polystyrene (PS, GoodFellow, Cambridge Ltd. UK) and Fluoroctatrichlorosilane (FOTS, Sigma-Aldrich, USA).

8. PHOTONIC 3D SYSTEM

Fabrication was performed with a 3D laser lithography system (*NanoScribe GmbH, Photonic Professional*). The excitation source was a femtosecond (fs) laser with an emission centre wavelength, pulse duration, repetition rate and peak power of 780nm, ~100fs, 80MHz and 25kW respectively. The laser beam was focused within the resin using a 100× or 63× microscope objective with a numerical aperture of 1.4 and 0.75, respectively. The main components and configuration can be seen on figure 6:

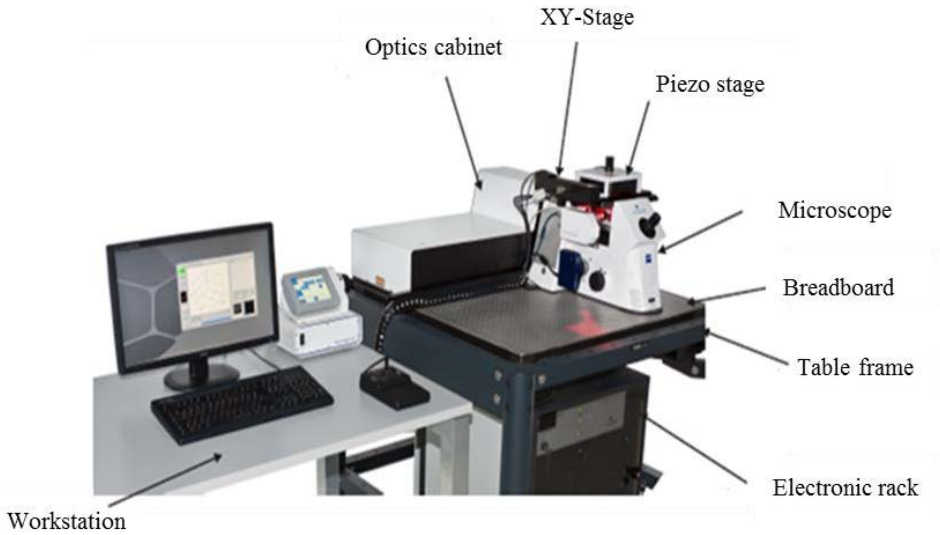

Figure 6 – NanoScribe's Photonic 3D. The optics cabinet is mounted on a breadboard and holds the laser and optic. Microscope is a Carl Zeiss Axio Observer equipped with motorized coarse stage (XY-stage) and a piezo stage as well as a live imaging system, focus dial and autofocus system. Image from NanoScribe operational handbook manual[181].

8.1. PROCESS WORKFLOW

When photoresist materials are used in micro-device fabrication, a processing protocol including some steps has to be followed. Substrate cleaning, photoresist deposition, material exposure, and development are the main stages (Figure 7).

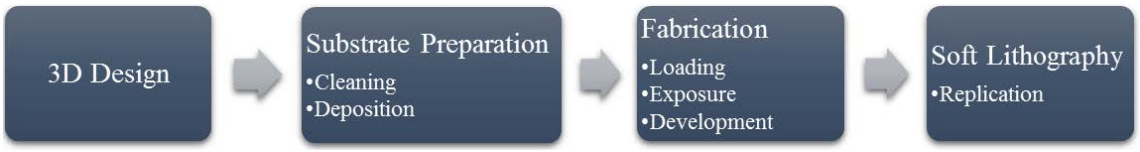

Figure 7 – The workflow of the two photon polymerization fabrication process starts with a 3D model of the desired structure. To initiate the fabrication process, the substrate is first cleaned, the photoresist deposited and loaded into the microscope to initiate the exposure phase. When finished, the structure is placed in a developer bath, to remove unpolymerized resist and it is ready for use or replication.

8.1.1. STRUCTURE DESIGN AND HARDWARE CONTROL

Hardware was controlled using NanoScribe proprietary software NanoWrite 2.1 and fed GWL (general writing language) programs, containing relevant information regarding laser focus trajectories and parameter configuration.

Objects were programmed using NanoScribe coordinate based programing language DeScribe v2.1. Additionally, structure design may also be exported from CAD (computer assisted design) software as STL (standard tessellation language) format and converted to GWL by NanoSlicer v2.1.

8.1.2. SUBSTRATE PREPARATION

Standard 30mm, 170µm thickness, glass cover slides were rinsed with isopropyl alcohol (IPA), dried under nitrogen stream and used without further treatment. They were secured in a substrate holder by rubber cement glue and the resist was drop cast on the top side of the glass slide as depicted on figure 8-a. When using the 100× objective a drop of immersion oil was added on the bottom side, as illustrated on Figure 8-b.

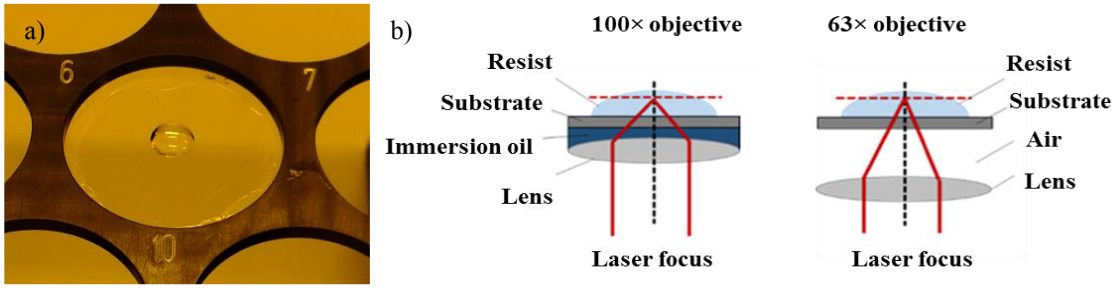

Figure 8- Deposition step of the substrate preparation process. a) Drop of photoresistive material cast on to a glass slide. b) Illustration of laser focus position when using 100x (left) and 63x objectives (right). The 100x objective is placed in contact with an immersion oil and 63x is exposed to air.

8.1.3. FABRICATION

Upon substrate fixation, photoresists were prepared, handled and development as shown in Table 4:

Table 4- *Fabrication parameters for different tested photoresistive materials.*

Photoresist	Material state	Handling	Prebake	Post-bake	Development
IP-L 780	Liquid	Drop cast	None	None	PGMEA/IPA
IP-G 780	Sol-Gel	Drop cast	1h @ 100ºC	None	PGMEA/IPA
Biopolymer	Liquid	Drop cast	None	None	PC

Fabrication was initiated with the laser being focused along a predefined pattern within a suitable photoresist (Figure 9.a). Afterwards, the unsolidified remainder of the photoresist was removed, using the appropriate development agent (Figure 9.b). Afterwards, remains of the development solution was removed by IPA rinse and dried by gentle nitrogen stream or left to evaporate at room temperature, leaving the newly fabricated microstructures on the substrate (Figure 9.c).

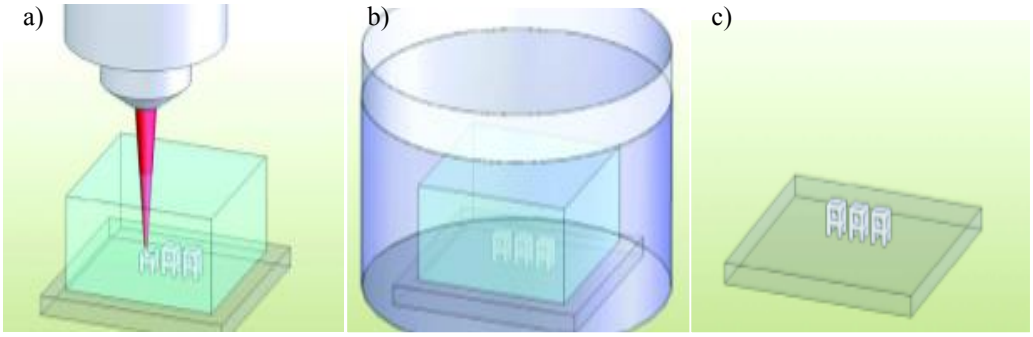

Figure 9 -Representation of TPP fabrication procedure. a) Laser focus within a light sensitive resists induces a polymerization reaction. b) Development step, where uncrosslinked resist is washed away by a solvent bath. c) Finished object. Images from: Application note, Three-Dimensional Microfabrication by two photon polymerization[140].

Upon completion, samples were visually inspected, by scanning electron microscopy (SEM; Philips XL-30, Netherlands) with secondary electron (SE) detection and sample stage with a 45º tilt for better 3D visualization. The samples were nonconductive polymer and therefore required a gold coating process, by sputtering at 30 mA for 40 seconds in argon atmosphere. Additionally, structures were also visualised using fluorescence (E600, Nikon, Japan) and generic optical microscopes.

8.2. SOFT LITHOGRAPHY

Soft lithography techniques were used to replicate 2PP constructs. An overview of the different procedures is represented in the following schematic:

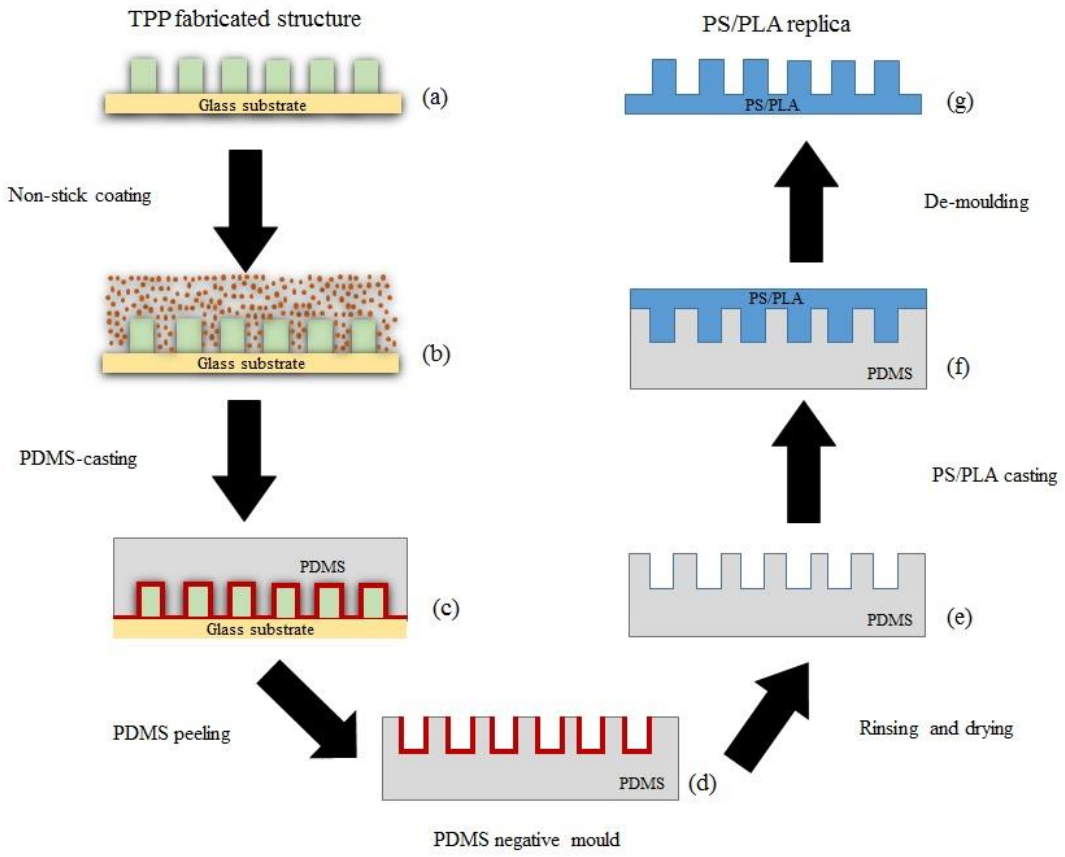

Figure 10- Soft lithography replication process: a master mould containing a TPP fabricated construct was coated with a non-stick layer and cast on to PDMS (steps a through c). The negative PDMS mould was peeled of the glass substrate, rinsed and used to pattern PLA and PS sheets (steps d through f). Lastly, the PS and PLA replicas were removed from PDMS mould.

8.2.1. NON-STICK COATING

A non-stick coating was prepared using a chemical vapour deposition process. A sealed petri dish was heated, along with 2PP fabricated sample at 120 ºC for 15 minutes. Afterwards, one drop of Fluoroctatrichlorosilane (FOTS) was placed inside on top of the cover slide, resealed and once more heated at 120 ºC for 2 hours. Afterwards, it was let to cool into room temperature before reheating at 100ºC for 1 hour. The petri dish with sample was then removed from the oven and cooled at room temperature.

8.2.2. MOULD PREPARATION IN POLYDIMETHYLSILOXANE (PDMS)

PDMS was mixed with the curing agent in a 10:1 ratio, stirred for 5 minutes to homogenize and centrifuged at 4000rpm for 1 minute to remove air bubbles. The mixture was cast onto the master mould, placed inside a desiccator connected to a vacuum pump for 15 minutes for further degassing and better PDMS fill of mould features. Finally, the PDMS was cured in the oven for 3 hours at 60 ºC, manually cut and peeled from the master mould, cleaned with ethanol and dried under nitrogen stream.

8.2.3. HOT-EMBOSSING (PS/PLA CASTING)

8.2.4. THIN FILM PRODUCTION

Polystyrene (PS) and polylactic acid (PLA) films were used to create replicas from the PDMS negative mould. The PLA film was prepared using high molecular weight PLA pellets, compressed to a film whose thickness could be controlled by means of hot-press. Film preparation parameters are presented in Table 5.

Table 5- *Hot-Press parameter settings for PLA thin film fabrication.*

Material	Temperature (ºC)	Pressure (kN)	Weight (g)	Thickness (µm)	Diameter (cm)
PLA	150.00	50.0	6.14	0.55	119.3

The pellets were placed on top of a metal square base with a sheet of Teflon, followed by a metal frame, to prevent overflow of the PLA when it reaches its melting point, covered again with Teflon sheet and place another metal square on top as seen on Figure 11.

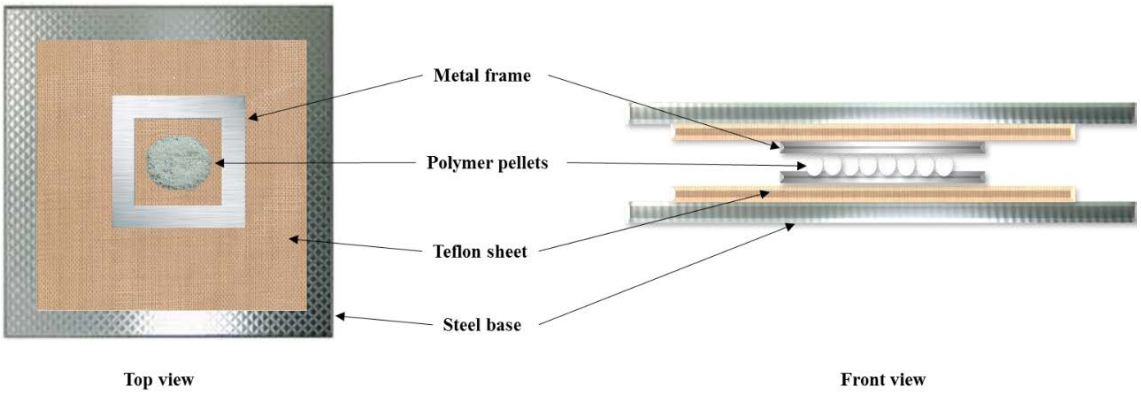

Figure 11 –Illustration representing top and frontal view of the hot embossing apparatus. The components are layered as follows: steel base, teflon sheet, metal frame, PLA pellets, metal frame, teflon sheet, steel base.

The hot-press was pre-heated up to 150ºC, the sample placed in the middle of the blocks and compressed at 50kN and 150ºC for 5 minutes. It was then cooled at room temperature or by nitrogen stream and cut into small discs using a steel puncher.

8.2.5. IMPRINT

PS and PLA, replicas were fabricated as illustrated on Figure 12. The setup was secured via clamps and layered as follows: glass slide, teflon, PDMS mould, PS\PLA film, teflon and glass slide. After assuring proper balance and stability, the sample was cured for 1 hour at 60ºC and 15 minutes at 60ºC for PS and PLA, respectably and finally cooled with a nitrogen stream or at room temperature.

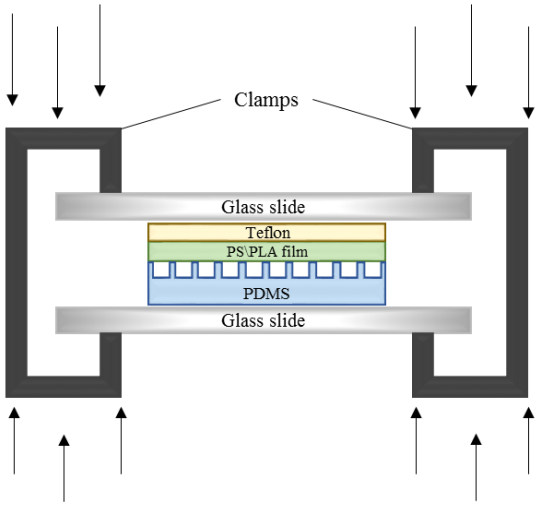

Figure 12 - Overview of imprinting process, a) through f). Glass slide with PDMS master mould sequentially adding PS or PLA thin film, layer of Teflon, glass slide and paper clamps.

9. CELL CULTURE MATERIALS

Triton X-100, Tween-20, bovine serum albumin (BSA) and hexamethyldisilazane (HMDS) were obtained from Sigma-Aldrich, USA, and used without further processing. Phosphate buffered saline (PBS), Minimum Essential Medium α (α-MEM), fetal bovine serum (FBS) and trypsin were from Gibco, Life Technologies, USA. Fluorescein isothiocyanate (FITC) conjugated antibody for vinculin, focal adhesion kinase (FAK) rabbit antibody, F-actin probe Alexa Fluor™ 594 for phalloidin, secondary antibody Alexa Fluor 647 anti-rabbit and 4',6-diamidino-2-phenylindole (DAPI) were from Invitrogen, Life Technologies. Human osteosarcoma cell line MG-63 (ATCC CRL-1427) was obtained from ATCC-LGC, United Kingdom.

10. CELL EXPANSION

Prior to cell culture, for sterilization, all samples were washed two times with 70% ethanol for 5 min, one time with phosphate buffered saline (PBS) for 5 min, transferred to new tissue culture treated plastic well plates, washed again with PBS for 5 min, and left in incubation with medium for at least 30 min before aspiration and cell seeding.

Human osteosarcoma cell line MG-63 was used with Minimum Essential Medium α (α-MEM) supplemented with 10% fetal bovine serum (FBS), 1% penicillin and streptomycin and 1% L-glutamine. Cells were cultured at 37 ºC in a humidified atmosphere of 5% CO2. Medium was replaced every 2 or 3 days. Upon reaching 80-90% confluence, cells were trypsinized with 0.25% trypsin in ethylene-diamine-tetraacetic acid (EDTA) for 5 minutes at 37 ºC. Trypsin was inactivated with three times the volume of medium, and sub-cultured in standard culture flasks or seeded for experiments. In all experiments, MG-63 cells were seeded at a density of 7500 cells/cm^2, in a working volume of 1.5 mL for 24-well plates and 2.5 mL for 12-well plates.

10.1. CELL MORPHOLOGY AND ATTACHMENT

Cell morphology and attachment were evaluated by a four channel fluorescence imaging of nucleus, F-actin, focal adhesion kinase (FAK) and vinculin. Cells were seeded and cultured on 24-well plates for 1 and 3 days, as described above. For imaging purposes all samples were done in triplicate. At each time point the medium was removed, samples were washed with PBS and fixed with 4% paraformaldehyde for 20 min at room temperature.

For fluorescent staining, samples were washed twice with PBS, permeabilized with 0.1% Triton X-100 in PBS for 5 min, washed twice with 0.1% Tween-20 in PBS (PBST). They were incubated in blocking buffer (2% BSA in PBST) for 30 min, and subsequently incubated overnight with a fluorescein isothiocyanate (FITC) conjugated antibody for vinculin (1:750 in blocking buffer) in combination with primary rabbit antibody for FAK (1:500 in blocking buffer). On the next day the samples were washed twice with PBST, incubated with F-actin probe Alexa Fluor® 594 phalloidin (1:40 in PBST) combined with secondary antibody Alexa Fluor® 647 anti-rabbit (1:400 in PBST) for 1 hour, washed twice with PBS and finally incubated with DAPI (1:100 in PBS) to

stain the nucleus, for 15 min. Samples were washed again and left in PBS. All incubation periods with fluorescent dyes were at room temperature in the dark.

Cells were observed with a fluorescence microscope equipped with a mercury lamp (E600, Nikon, Japan), for lower magnification (10x), and with a BD Pathway™ 435 (BD Biosciences, USA), for higher magnification (20x). The absorption and emission spectra of the fluorophores, Hg lamp and filters used are shown in Appendix 16.1 - Figure 45.

TECHNICAL SETUP AND OPTIMIZATIONS

Part I

This section illustrates the different existent interfaces, the manual trial and error process of determining them using a 63× objective and its influence to voxel positioning during fabrication. Additionally represented are particular fabrication issues that led to structure defect, either from technical limitations (piezo and XY-stage positioning systems), or microboiling and laser induced damage. Finally, it was shown that it is possible to employ soft lithography techniques to increase TPP fabrication throughput and rapidly replicate structures.

11. TPP TECHNICAL SKILLS AND COMPLEMENTARY FABRICATION TECHNIQUES

11.1. WRITING WITH AN AIR OBJECTIVE

Finding the proper laser focus interface is of paramount importance and can dramatically influence the success of the microfabrication process. While using the air objective, there are three main zones to consider: air-glass, glass-resist and resist-air (Figure 13).

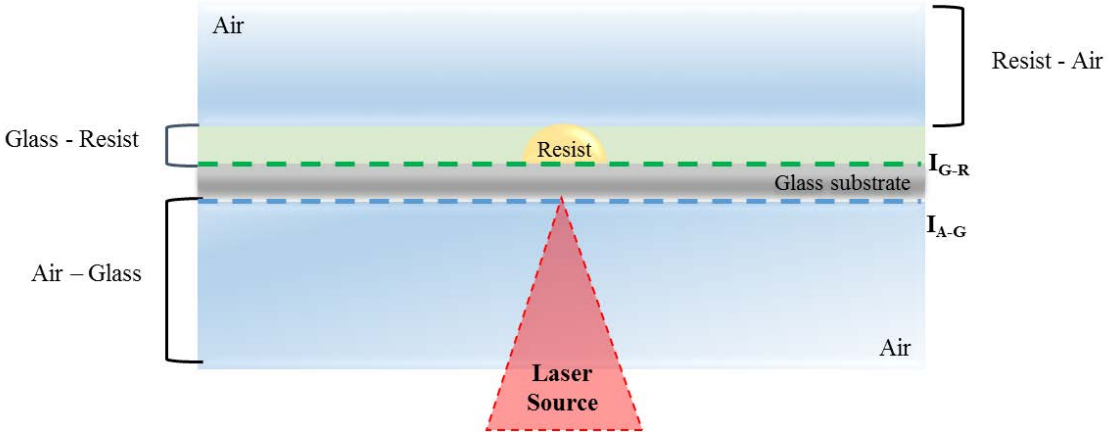

Figure 13 - Different zones found when attempting to detect the fabrication interface: air-glass, glass-resist and resist-air. The triangle vertices represent laser focal point using air objective. Blue dashed line represents the air-glass interface (I_{A-G}) and the green dashed line illustrates the glass-resist interface (I_{G-R}).

The air-glass interface is ignored when working with the 100× objective since the objective is directly positioned inside the immersion oil. This oil is index-matched to the 170µm thick glass substrate and objective lens allows for the glass-resist interface (I_{G-R}, Figure 13, green dashed line) to be automatically detected. This system is only fully

available if there is a slight difference in the refractive index, between the substrate and the photoresistive material.

Contrary to the immersion objective (100× amplification), when the system is set for air objective (63×) writing, the glass-resist interface is not easily detected, thus it is necessary to trigger a manual approach.

Figure 14 represents the interface finding procedures, using the microscope's live imaging system to monitor the sequential writing of test lines positioned at different laser focus locations.

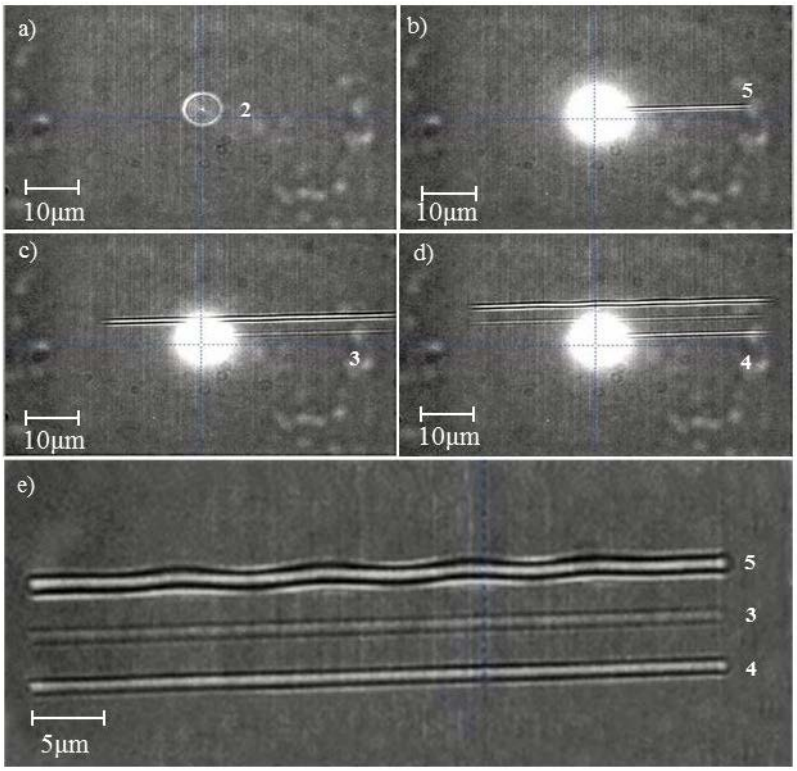

Figure 14- Sequence of interface finding auxiliary lines. a) Test line written at the air-glass interface. Images b through d represent test lines at different Z positions e) Comparison between the three test lines.

Reaching the optimal interface is mainly a trial and error process. Figure 14.a represents a line written at the automatically detected interface (air-glass, 9645.069µm). Unsurprisingly, no polymerization occurred but rather a diffraction pattern. This is a consequence of light (from a point source) passing through a small circular aperture, which produces a diffuse circular disc known as Airy disk. This phenomena will continue to be observable for as long as the laser is focused solely within the glass substrate (~107µm) and less visible during polymerization since it will be obfuscated by light emitted through the two-photon excitation effect.

As expected, polymerization starts at the glass-resist interface as seen on Figures 14.b, c and d found at 9741.886, 9738.725 and 97939.585µm, respectably. These three successful polymerization events represent generic positions used to accurately find the correct interface and are further illustrated at Figure 15.

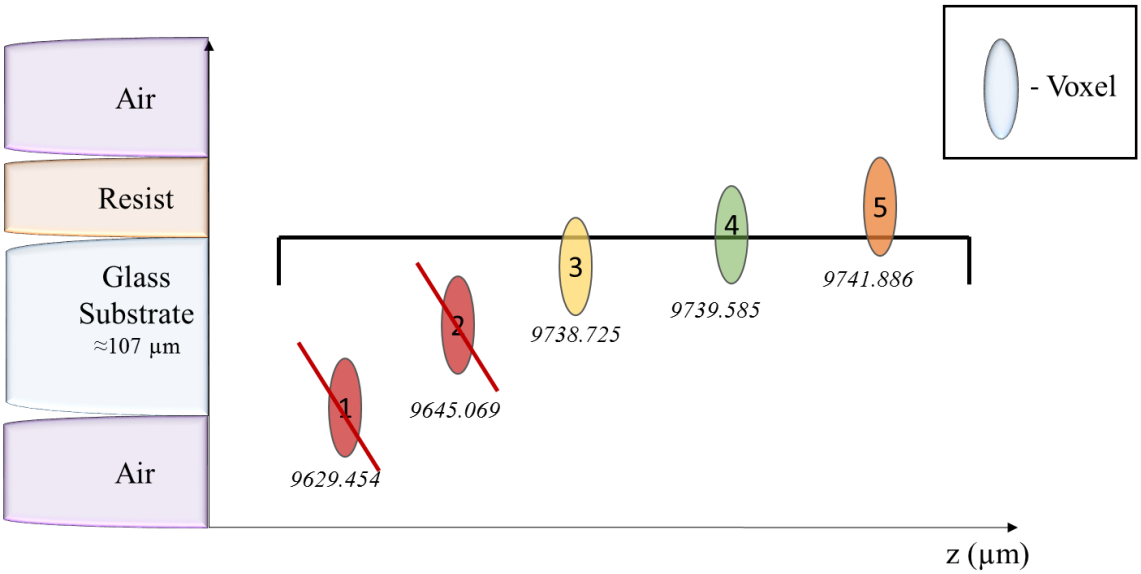

Figure 15 - Illustration of test lines used to find the best interface position. Each voxel number denotes a position which corresponds to the lines seen on Figure 15. Voxel positions 1 and 2 are unusable, 3 and 4 are usable with some limitations and voxel position n.º 4 is the ideal.

Voxel position nº4 (Figure 15) represents an ideal situation since it has an optimal surface area to quantity of polymerized material ratio, resulting in very strong connectivity to the substrate. The remaining positions may not be as secure. Particularly number 5, as it may not have sufficient area of contact which destabilizes the voxel (Figure 14.e -5) and might lead to unwanted removal during development phase.

Voxel nº3 (Figure 15) is strongly adhered to the substrate, however the low quantity of polymerized photomaterial may originate design imperfections or even, in certain circumstances, such as in large area printing, cause contact loss with the surface, thus not achieving polymerization.

11.2. Fabrication issues

11.2.1. Large area printing

One of the main challenges encountered to develop large patterns was overcoming the technical limitations of large scale printing (>300µm^2).

Voxel location may be controlled via two mechanisms with different positioning accuracies, XY-stage and piezo-stage. The piezo is accurate up to 10nm, however, it is

confined to a writing area of 300µm^2. The XY-stage may address a larger area (defined by the maximum writing area of the current substrate, though its accuracy is only about 1µm[181].

Figure 16 illustrates a sample holder, capable of storing up to ten samples, as well as a representation of addressable areas for piezo (grey square) and XY-stage (green area):

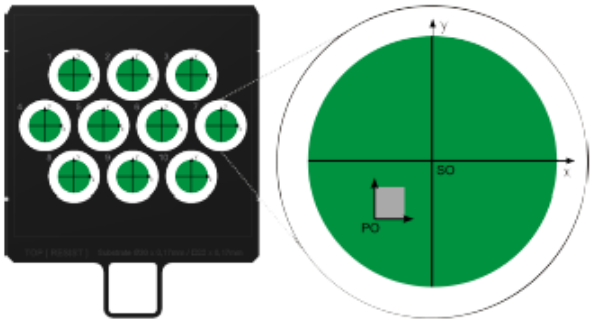

Figure 16 –Illustration of a sample holder device capable of storing up to ten sample positions. The green and grey areas represent the total addressable area by the XY and piezo stage, respectably. Image from NanoScribe operational handbook manual[181].

This constraint to piezo maximum addressable area, forces larger designs to be built in modules of up to 300µm^2, as illustrated on Figure 17.

Consequently, a typical writing cycle would employ the piezo for construction (coloured grids) and the XY-stage for repositioning after each 300µm block.

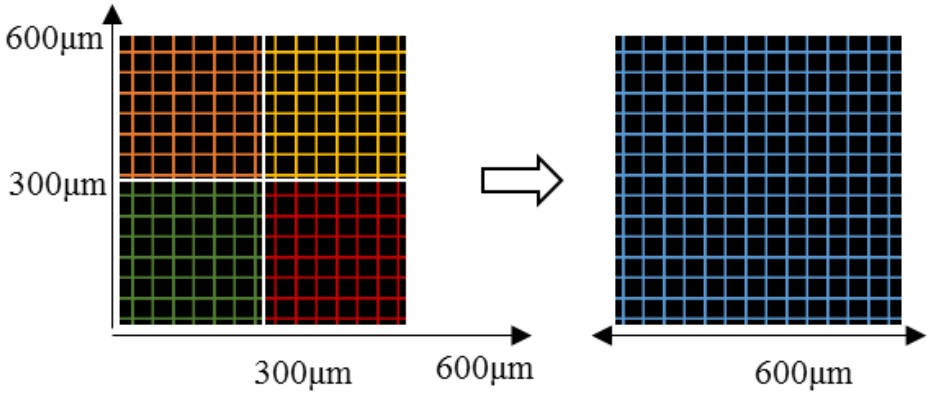

Figure 17 – Illustration of stitching method used to create patterns larger than 300um2 with the piezo stage. The structure was created using blocks of300 and then use the XY stage to position.

While this procedure may, in theory, allow overcoming the area restriction, it also leads to two different problem sets. First, given the low accuracy of the XY-stage, an improperly positioned voxel, might lead to design flaws which will destabilize and collapse structures. The second problem, originates from the constant stage repositioning which, if not properly calibrated, might lead to misalignment between the XY-plane of the piezo and the substrate surface (Figure 18).

Whenever a new sample position (sample holder, Figure 16) is selected, the system automatically triggers a calibration procedure to compensate for possible substrate tilt and adapts the design's coordinates to compensate for this shift. If the piezo stage is to be used, the calibration points will be evenly distributed throughout the 300×300µm^2 piezo range. For XY-stage writing, the measurements will take place over the complete addressable writing area on the current sample position and needs repeating only when changing to a new sample position.

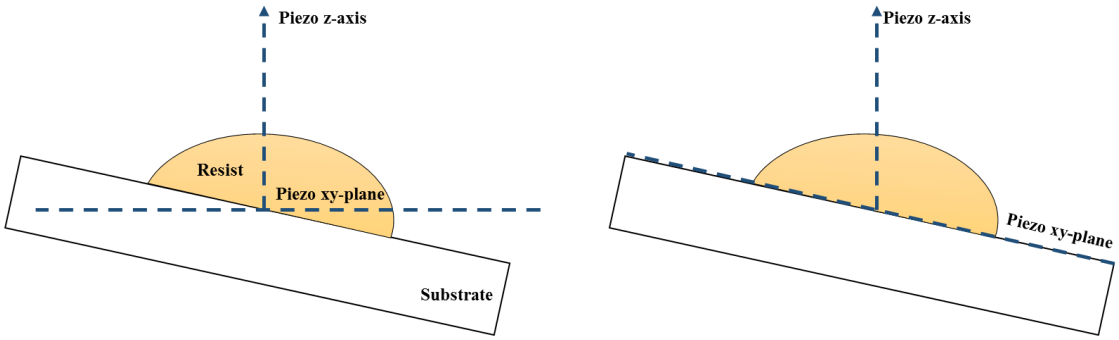

Figure 18 - This figure depicts the principle of tilt correction. To facilitate understanding, the tilt has been reduced to one direction and the angle has been exaggerated. The left hand side shows the uncorrected situation, the right hand side demonstrates side demonstrates the tilt-corrected case.

Given the limited calibration area of the piezo, it is necessary to implement a "*MeasureTilt"* command, in the GWL script code, to prompt a new adjustment after each XY-stage repositioning. This action should help preventing structures from not having sufficient contact to the surface and thus being torn off during development.

Figure 19 exemplifies the occurrence of the aforementioned issues:

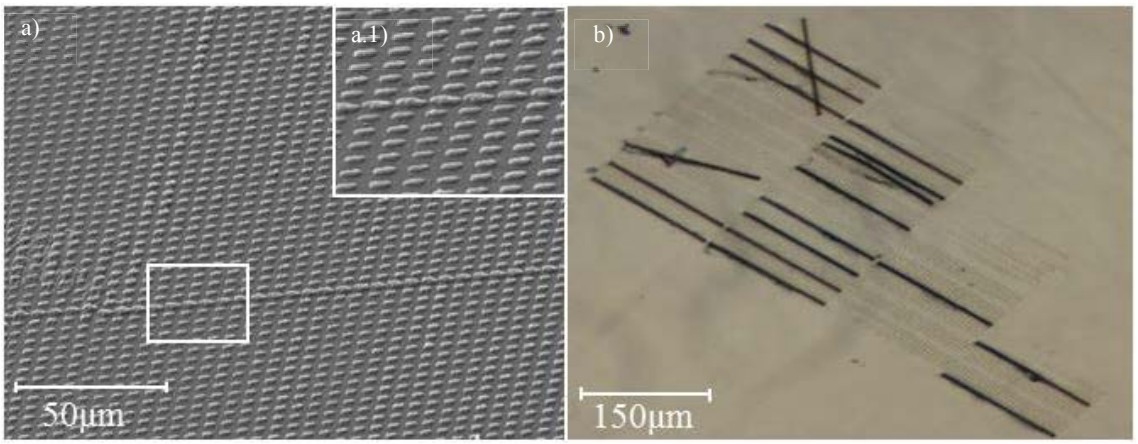

Figure 19- Examples of fabrication errors resultant from the technical limitations of large area printing. a) SEM image of a pattern composed of small dashes (3µm length) fabricated by stitching (Figure17) where a positioning inaccuracy led to voxel overlap. a.1) Higher magnification image of the defect. b) Beam structures collapsed due to stitching errors and lack of tilt correction (Figure18).

The first image (Figure 19.a) represents a 100×100µm^2 grid of lines (dashes), built as illustrated on Figure 17. It is possible to observe the overlapping dashes,

consequence of the stitching error due to XY-stage inaccuracy. Figure 19.b depicts a $600\times900\mu m^2$ structure composed of a series of beams ($150\times15\times10\mu m^3$) intercalated with dashes. The design failure can be attributed to a mixture of both mentioned errors since in addition to the low accuracy issues, there were also problems regarding stage tilt which resulted in many of the beams to be torn or washed away (due to insufficient contact area), during development stage.

11.2.2. MICROBOILING AND LASER INDUCED DAMAGE

Technical limitations aside, one of the most common reasons leading to structural degradation is the uncontrolled increase of temperature during fabrication which triggers boiling of the photoresist.

This phenomena occurs mainly in two situations: laser power dosage set beyond the threshold limit of the material, (maximum usable dose to safely process a resist) thereby generating sufficient heat to locally boil, or even burn, the resist. This effect might also be observed in the presence of dust particles, air bubbles, crystallites or other microscopic particles which absorb laser light and induce a localized temperature increase.

Figure 20 exemplifies fabrication defects resulting from heat induced deformation and burning.

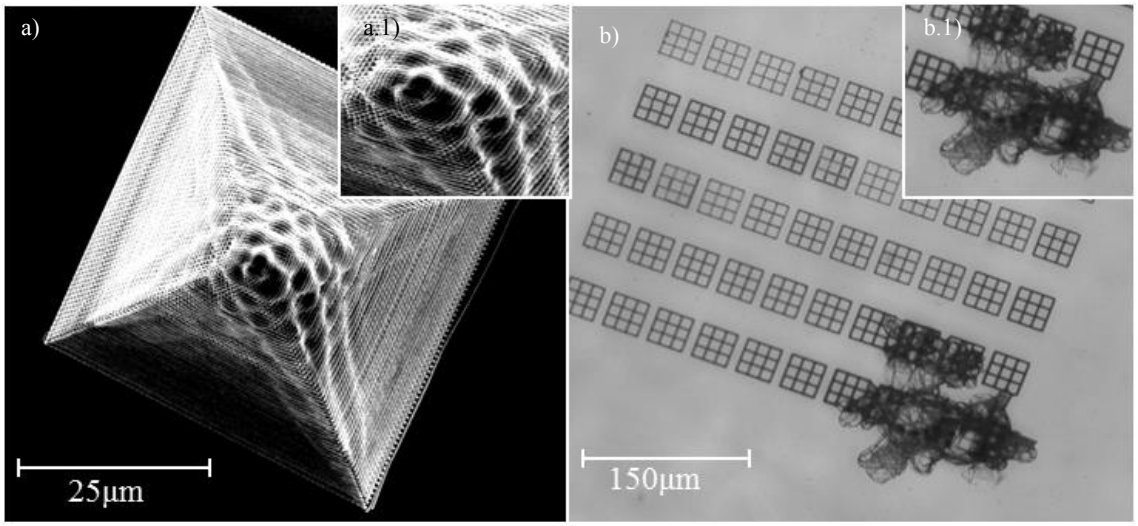

Figure 20 – Examples of TPP heat induced fabrication defects. a) SEM image of a woodpile pyramid exhibiting microboiling deformation at the top section. a-1)Higher magnification of the deformation. b) Bright field image an array of 3x3 grids with localized laser induced damage (lower bottom right section). b-1) Higher magnification of the burnt area.

Figure 20.a depicts a SEM image of heat induced deformation bubbles on a solid $50\times50\times120\mu m^3$ pyramid, fabricated (bottom to top) using a woodpile pattern. The fact that the defect appears to some extent limited to, the top section is an indication that initially, the energy dose is not excessively high. It seems however, that the cumulative effects of continual laser exposure on the same layers in addition to the smaller dimensions at the top, exacerbate the damage. As a result, when building high structures (>100μm) it might be necessary to dynamically change the laser power in order to avoid resist degradation or in some cases use top-to-bottom fabrication techniques.

Figure 20.b shows a series of $30\times30\mu m^2$ grids, (fabricated under varying laser power and writing speed settings) presenting a more severe case of localized boiling, ultimately resulting in burning. Considering that fabrication was performed inside a cleanroom, the "explosion-like" shape of the burnt area and the fact that no significant parameters had change between structures, it is possible to attribute this defect to impurities in the resins, in all likelihood a gas bubble. Given the severity of this and other defects originated from impurities, in order to reduce the chances of this happening, it is advisable, but not mandatory, to perform fabrication in filtered and dust free environments such as a cleanroom.

11.3. SOFT LITHOGRAPHY

In TPP and other fabrication processes, there is usually a close relationship between speed and quality which may originate high fabrication times. One way of increasing throughput is by using 3D soft lithography (a moulding technique) in conjunction with TPP fabrication to generate multiple copies of identical scaffolds [178]. This is typically achieved using the industry standard, PDMS, which apart from other characteristics, also exhibits a low interfacial free energy which helps preventing adherence of most materials[182].

11.3.1. IMPRINTING PROCESS

Imprints originated from master moulds (2PP constructs) with simple shaped geometries, such as a pyramid, were easily fabricated and yielded good results.

Figure 21 represents SEM images of a 10x10x5μm^3 pyramid array and corresponding polystyrene (PS) replica:

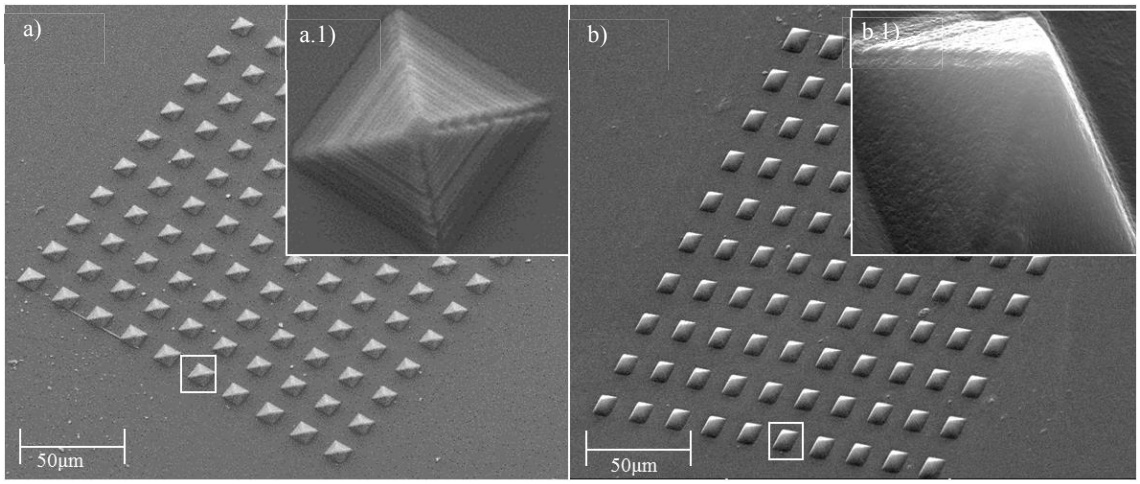

Figure 21- SEM images of TPP fabricated structure and PS replica. a) Pyramid array fabricated by TP. a.1) Higher magnification of the structure where a ridge-like surface pattern can be seen. b) Polystyrene replica of the array. b.1) Higher magnification of the imprint which presents a smoother surface than the original mould.

A visual comparison between the master mould and imprint, shows no significant structural differences apart from some alterations in surface topography. The original groove-like surface pattern (intentional fabrication design), seems to have been lost during replication and replaced by a more homogeneous and porous topography.

Despite the success of this procedure for simple structures, objects with intricate, or fragile parts, may require additional steps in order to increase the chances of successfully peeling the PDMS, off the master mould, without pattern fracture.

11.3.2. MOULD OPTIMIZATION

Figure 22 represents a 3D model schematic of a pattern with more delicate features. It is composed of a series of 150×15×10μm^3 beams and 3μm dashes filling the space between them.

Initial attempts to create a PDMS negative mould from this master were unsuccessful due to remnants of dashes, from the original structure, becoming trapped in the PDMS spaces and preventing filling. This can be observed in Figure 23.a, which represents a fluorescence image of the PDMS mould, where the bright spots represent the unremoved photoresist.

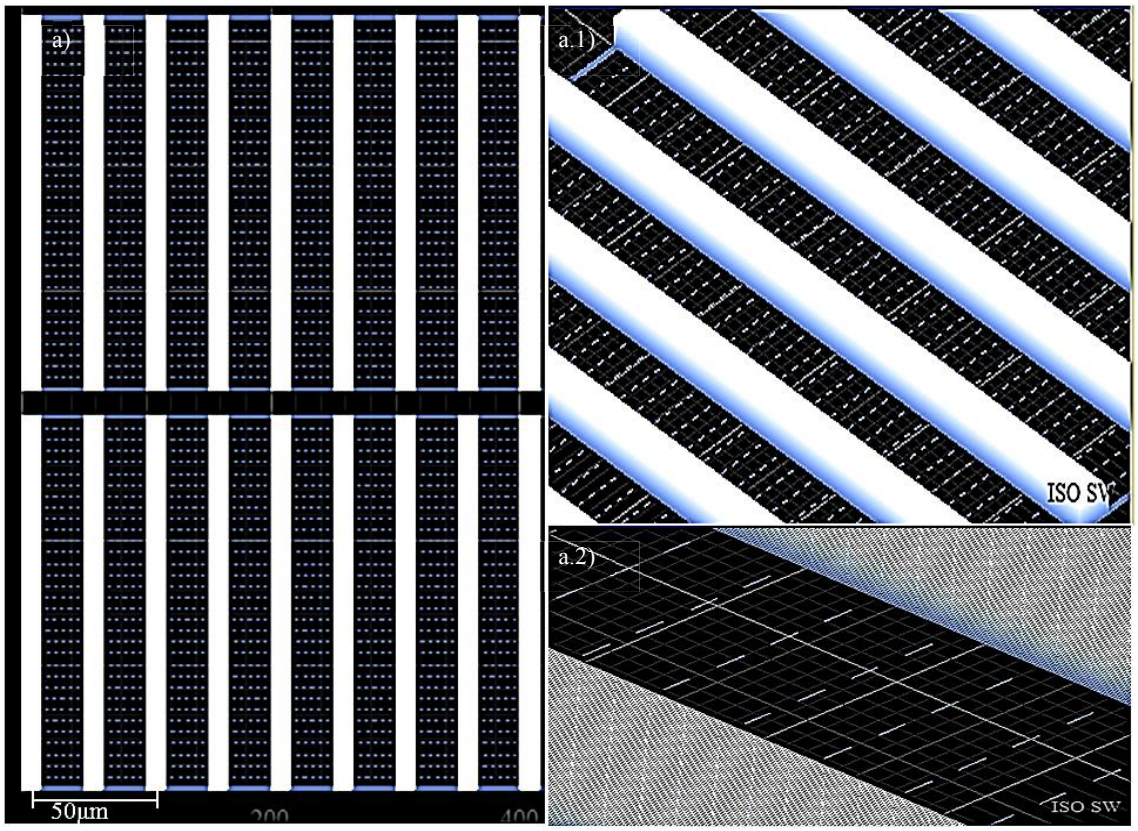

Figure 22 - Three dimensional model of a pattern. a) Schematic overview of a structure built using beams and dashes. a.1) Isometric magnification view of the beams. a.2) Magnification detailing the dashes.

To improve the odds off successful PDMS removal, a non-stick coating was applied, by molecular vapour deposition, to the master mould. Although the procedure was successful, in diminishing the number of trapped, it did not completely prevent it.

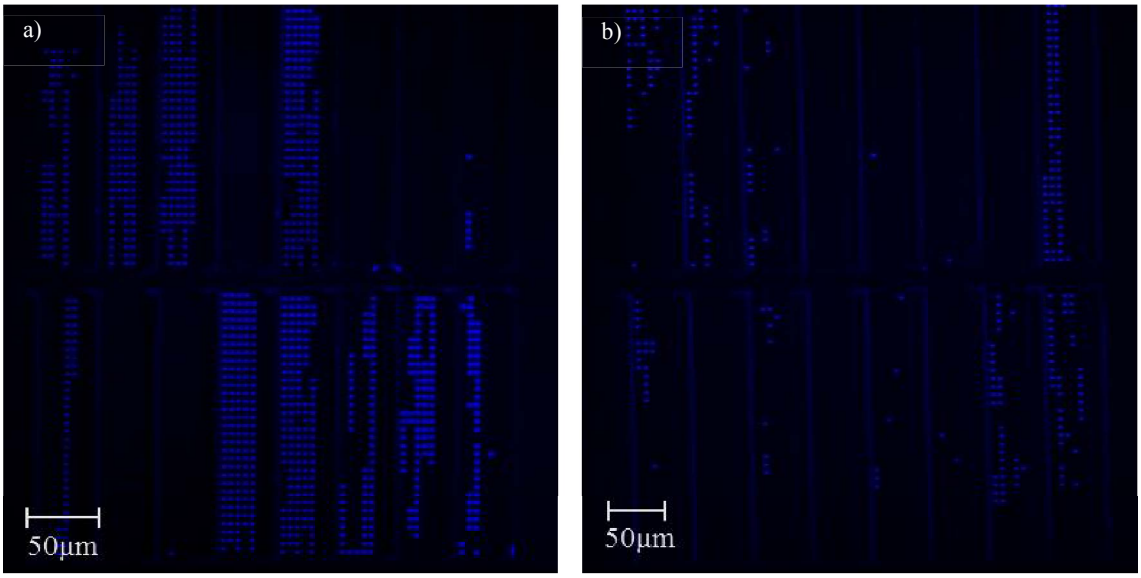

Figure 23- Fluorescence images of PDMS negative moulds. a) Untreated PDMS mould showing a high percentage of unremoved photoresist represented by the bright spots. b) Non-stick coated mould.

Figure 23.b depicts the improved outcome of the coating treatment, as seen from the lower number of bright spots, *i.e.* dashes. In addition to non-stick coatings, other authors have reported an alternative, or complementary, method to improve the peeling process of delicate structures, by attaching the PDMS mould to a piezoelectric stage and carefully moving it while the original structure substrate was fixed in place[183].

11.3.3. REPLICA TOPOGRAPHY CHARACTERIZATION

To evaluate the efficiency of the replication process to use in various different designs, polystyrene (PS) and polylactic acid (PLA) imprints were fabricated, using the PDMS mould from Figure 23.b, and visually inspected via SEM, as seen on Figure 24:

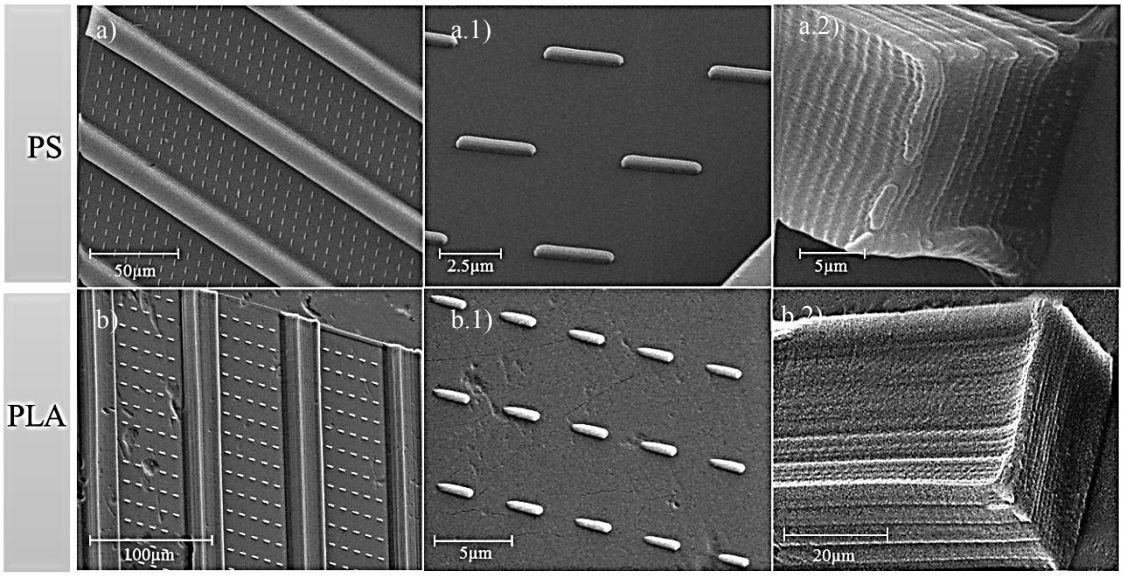

Figure 24 – SEM images of PS and PLA imprints fabricated using the non-stick coated PDMS mould from Figure 24.b). a) Overview of the beam and dashes PS replica. a.1) Greater magnification detailing the PS dashes. a.2) Magnified view of a PS beam. b) General view of the PLA beams and dashes replica. b.1) Magnified image of the PLA dashes. b.2) Increased magnification of a PLA beam.

A comparison between PS and PLA imprints, shows no apparent structural differences apart from a small deformation on the top section of the beams and some topography dissimilarities in all likelihood due to the differences between materials and imprinting procedures. It is not clear if this deformation resulted from the replication processes or if it was already present in the original mould since a thorough characterization of the TPP construct was not performed.

Planar dimensions were estimated during SEM imaging and appear to be in accordance to the originally programed parameters, $150\times15\mu m^2$ beams and 3µm dashes. Feature height was assessed by white light interferometry and used to generate 3D average height models as seen on Figure 25:

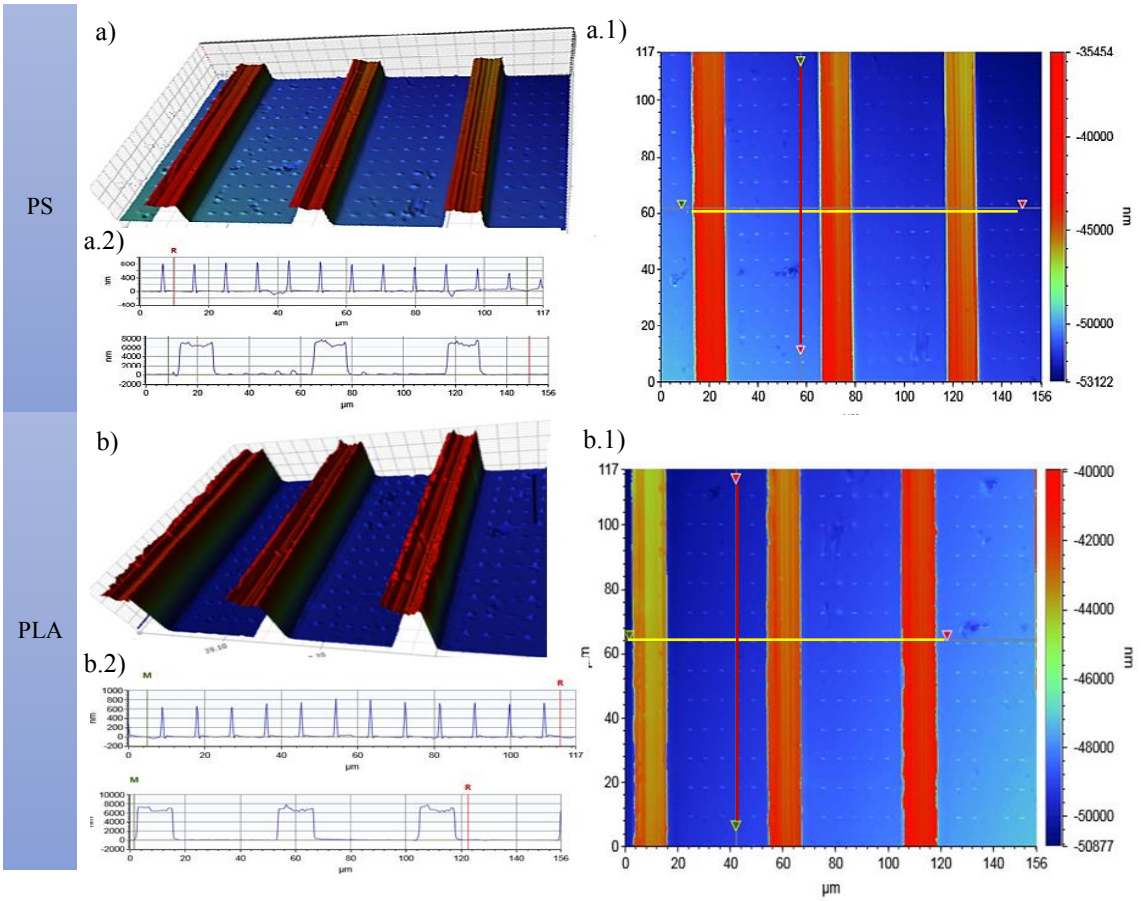

Figure 25 – 3D generated model of PS and PLA beam and dashes structures. a) 3D model of PS replica of the beams and dash pattern. a.1) Height heat map of the PS model. a.2) Measurements of PS features height. a) 3D model of PLA replica of the beams and dash pattern. b.1) Height heat map of the PS model. b.2) Measurements of PS features height.

Analysis of the graphics (Figure 25.a.2 and b.2), where each narrow peak represents features found along the y axis (red line, Figure 25.b1 and b.2) of the heat maps and the wide peaks correspond to measures made along an x axis (yellow line, Figure 25.b.1 and b.2), revealed similar values for both PS and PLA imprints.
Dash height is on average 800nm and beams oscillate between 8µm on the borders and 6µm in the middle which is lower than the programmed height (10µm) and also confirms the deformation seen in SEM images. Larger version of the graphics are available for consultation in Appendix 16.2 and 16.3 - Figures 46 and 47 for PS and PLA respectably.

Chapter II

The following section depicts the learning process regarding photolithography fabrication and the influence that experimental parameters (such as laser power and writing speed) have on overall structure integrity. Given the dynamic nature of voxel formation it was

also shown the inherent iterative process necessary to improve the overall quality of the structure.

12. EARLY STAGE STRUCTURE DESIGN AND FABRICATION

Initial attempts to construct objects using the 3D photolithography system were rather unsuccessful. The first test designs comprised of three distinct objects: wireframe cube and helix arrays, programed using *DeScribe* and a solid rectangle designed using CAD software and converted from STL to GWL using *NanoSlicer* with standard settings.

Figure 26 illustrates the 3D models of each structures and their respective brightfield and fluorescence image:

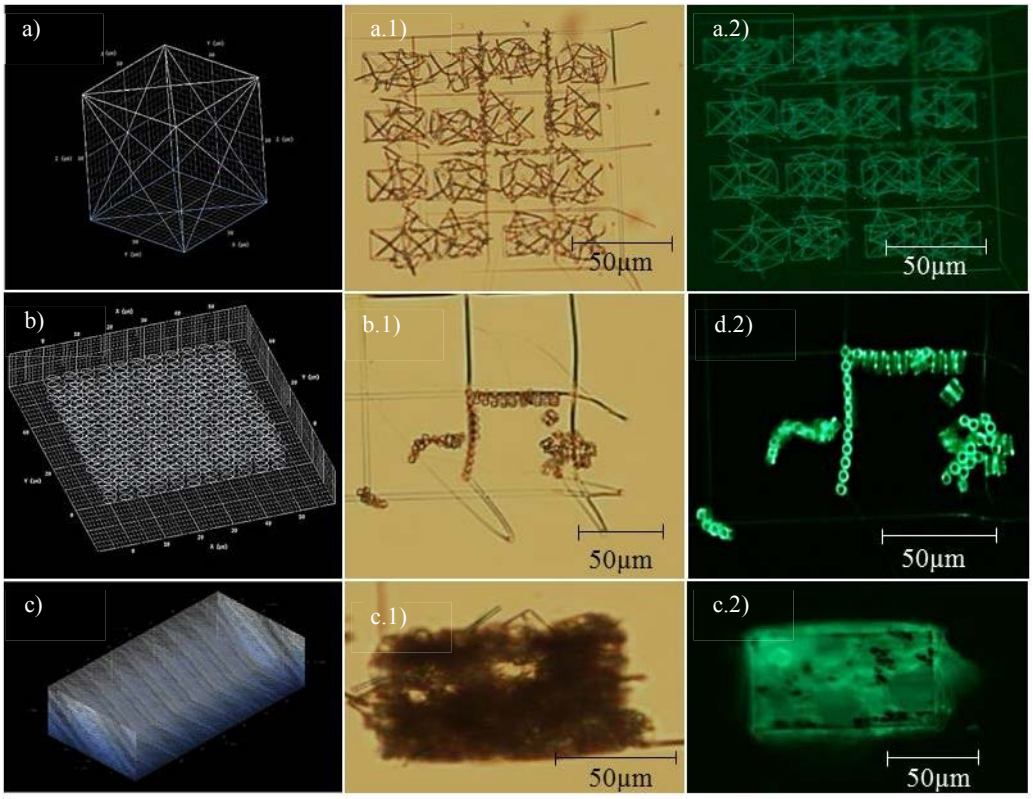

Figure 26 – Early fabrication stage of TPP constructs. a) 3D model of a wireframe cube. a.1) Brightfield image of collapsed wireframe cube array. Fluorescence image of the collapsed array. b) Schematic of a helix array. b.2) Brightfield image of the remnants of the helix array. b.2 Fluorescence image of the helixes. c) 3D representation of a solid rectangle. c.1) Brightfield image depicting the deformation of the fabricated design. c.2) Fluorescence image of the solid rectangle.

These structures were created using IP-L photoresist and the 100× objective with standard settings. As it is readily apparent, the majority of structures collapsed or have otherwise been deformed. From these results it was gathered that voxel order formation and foundation support is necessary requirement when dealing with liquid resists such as the IP-L. Notwithstanding this result, great deal of information was gathered which

ultimately proved advantageous for the creation of increasingly stable and complex structures.

12.1. PARAMETER TESTING

The preceding results exposed the necessity of assessing the effect of certain operational settings on voxel formation. Thus, a test program was devised to generate a series of lines written at increasingly smaller distances (100nm between last lines) while simultaneously varying laser power, 20 to 150 % (increments of 10%) and writing speeds ranging from 50 to 300µm/s (25µm/s increments).

This test is partially represented at Figure 27 and depicts a writing speed of 225µm/s at laser power-writing speed axis origin:

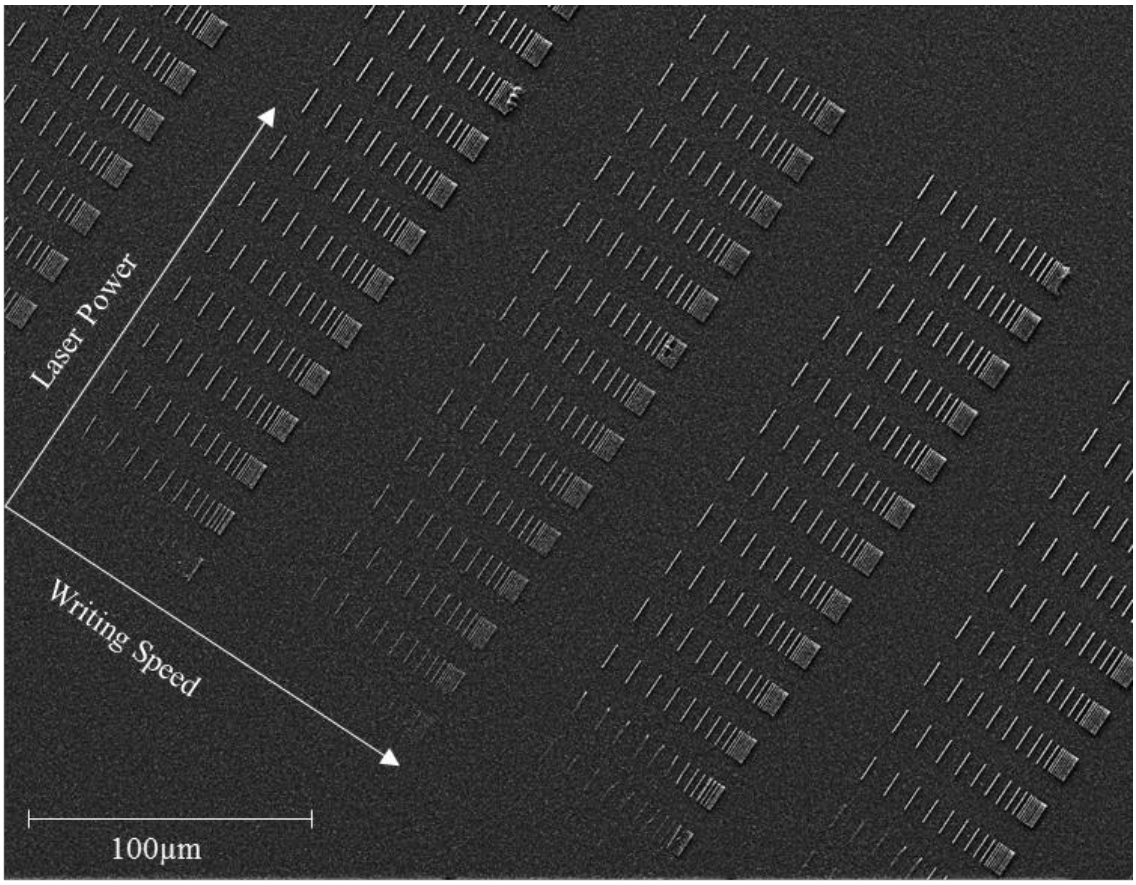

Figure 27 - Parameter sweep test for different laser power and scanning speed values as well as lateral resolution testing. Laser power is set to increase from 20 to 150 % (increments of 10%) and writing speeds range from 50 to 300µm/s (25 µm/s increments).

This test was of empirical nature since an exhaustive characterization of voxel formation would be far too time consuming and not the focus of the project. As such, the main objective was to acquire a visual assessment of the voxel formation process and parameter influence on its formation.

From observation of the different fabricated lines it was gathered that certain combinations of low laser power and high writing speeds leads to either very fragile and deformed voxels (50 to 150µm/s) or polymerization may not occur (150-300µm/s).

Figure 28 represents a line pattern fabricated using 20% laser power and 100µm/s writing speed. The lines are deformed and hardly visible, this effect gets progressively worse as speed increases up to 150µm/s and beyond that, the energy dose is not sufficient to induce polymerization.

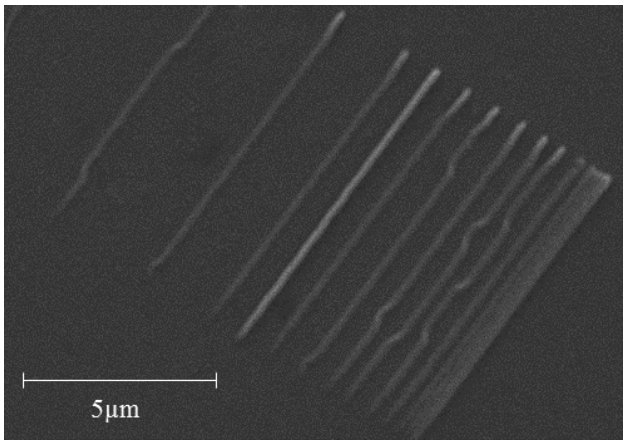

Figure 28- SEM image of the parameter test lines for 20% laser power and100µm/s writing speed.

For higher values of laser power, there is, as expected[181], a clear linear dependence between voxel size and energy dose. Figures 29.a and b represent voxel fabrication at 100µm/s and laser powers of 50% and 150% respectably:

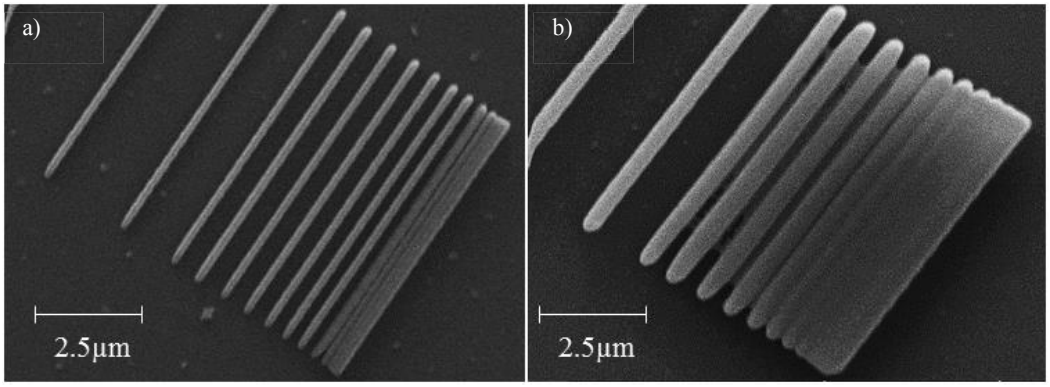

Figure 29-SEM images show the influence of laser power on voxel dimensions. a) Test lines written at100µm/s and laser power of 50%. b) Test lines fabricated at 100µm/s and laser power of 150%.

12.2. ITERATIVE NATURE OF STRUCTURE DESIGN

12.2.1. WOODPILE TEST STRUCTURES

Given the dynamic nature of voxel formation (depends of photoresist, energy dose and writing speed), when programming a new structure it is necessary to perform a

dosage test in order to determine the parameters that best fit the design while maintaining an adequate speed to quality ratio. This is achieved by replicating a structure, or a part of it, several times at different locations while varying system settings such as laser power and writing speed, or design parameters such as the distance between individual voxels and layers.

Figure 30 represents an example of this iterative process by depicting the successive fabrications attempts of a $30\times30\times15\mu m^3$ woodpile.

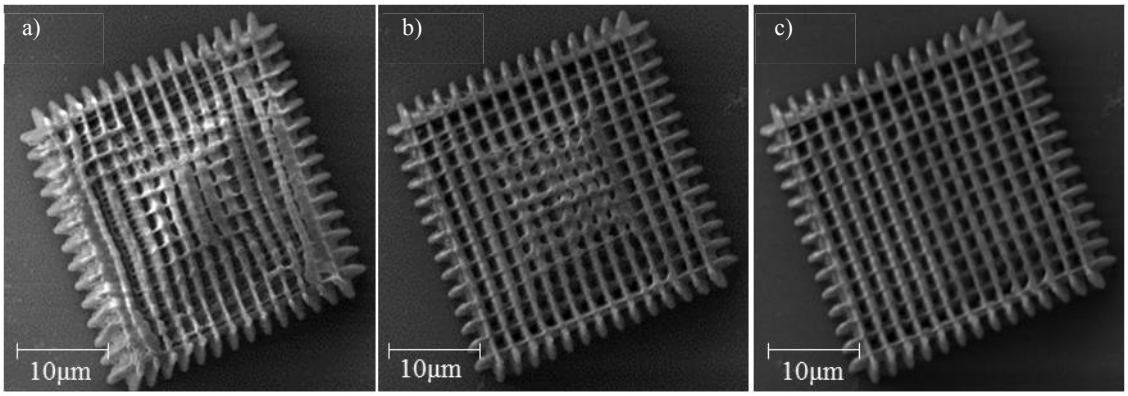

Figure 30 - Iterative process of TPP fabrication. By replicating a structure, or a part of it, the best combination of fabrication parameters and design is achieved.

This structure consists of layers of evenly spaced three dimensional rods in a repeatable stacking sequence and were built using the 100× objective and IP-L resist. From the image sequence it is possible to observe some deformation and other defects within the middle section of the first image (Figure 30.a), where some voxels appear to have fused. By progressively changing these parameters, decreased writing speed (Figure 30.b) and lower laser power (Figure 30.c) it was possible to fabricate an object with less apparent significant defects.

12.2.2. VERTICAL VOXEL

The fabrication of objects through voxel stacking in a xy-plane, although not without issues, is usually a straightforward process. The same cannot be said for single voxel extrusion, which is inherently much less stable and has a limited aspect ratio.

The following image sequence represent the various defects encountered during fabrication of rod-like structures, built using a liquid photoresist (IP-L) and programmed as single lines plotted in z direction.

Structure collapse due to improper combination of design settings/photoresist (Figures 31.a and 31.b) and/or careless development procedures (Figure 31.c) was one of the main issues. Given the low viscosity of the photoresist, high aspect ratio constructs

were difficult to achieve. If the programed height was high (>10 to 15µm) the voxel would collapsed under its own weight. If the laser power was increased, to created larger voxels,

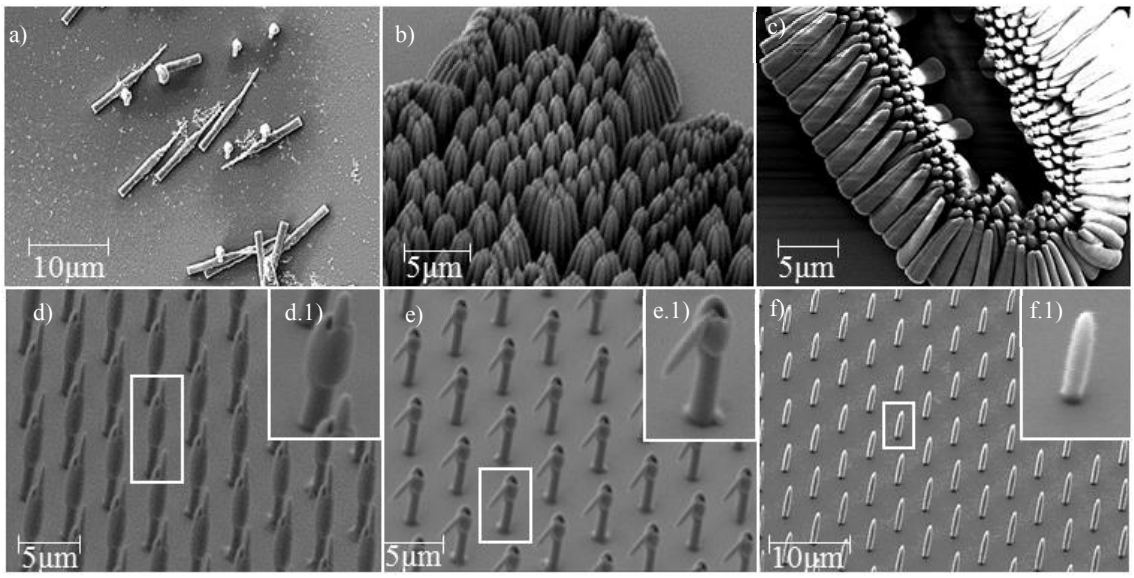

Figure 31 – SEM images depicting several attempts to create an array of reproducible and stable vertical voxels.

the object would also present defects since the top part would not be supported and would oose back, creating almost like a coating around the voxel (Figure 31.d).

For a particular combination of parameters an interesting effect was noticed. Figures 31.d and 31.e represent structures that have collapsed in a controlled and reproducible way. In Figure 31.e increasing the height beyond the aspect ratio threshold led to the top section bend in a hook-like manner. This is good example of the reproducibility of TPP fabrication, since even structure deformation can be replicated and possibly exploited to develop complex structures that would otherwise be very difficult, or even impossible, for conventional techniques. In fact, Rezende et al., (2014) has developed velcro® -like spheroids with interlockable hooks, "lockyballs", for *in* vivo bottom-up modular biofabrication[184].

The tested parameters were not by any means exhaustive and it would have been possible to construct higher aspect ratio objects as shown by Obata et al., (2013) who managed to fabricate structures with heights up to 7mm using a modified optical TPP setup[185].

Since high aspect ratio single voxel spikes could not be fabricated in a consistent manner, a highly reproducible 100×100µm^2 array of 5µm spikes was designed and can be seen on Figure 31.f.

RESULTS

13. PATTERN MICROFABRICATION

Cells response to topographical cues is a well-documented research area and it has shown that through a phenomenon known as contact guidance, cells react to surface features by changing their proliferation, adhesion, migration and/or cell orientation[186,187].

Micro and nanotechnology have been used to create patterned surfaces that promote cell alignment and/or induce differentiation. Given the inability to fully replicate the complexity of cells microenvironment, the choice of optimal surface topography is not consensual, and patterns are usually developed to target specific areas of interest and are therefore subjected to personal bias. Some explore the effect of micro-groves (ridges) dimensions[186], while others such as Dalby et al., (2007) focus on randomly placed nano-pits[179]. Additionally, Unadkat et al. (2011) have developed a TOPOCHIP device, whereas through a mathematical algorithm, thousands of randomized geometries were generated, based on simple shapes such as circles triangles and rectangles, in a single chip aimed at instructing or studying cell behaviour in an unbiased way[188].

Despite an abundance of studies, exploring numerous geometries, reports based on patterns with real 3D shapes and variable heights (or other dimensions) within a single sample configuration are less common[186]. This is due to lack of appropriate fabrication techniques, since traditional photolithography and soft-lithography usually require multiple process steps, with a number of masks, in order to fabricate variable dimension patterns on the same substrate[189].

13.1. STRUCTURE CHARACTERIZATION

Considering TPP's potential for fabricating arbitrary three-dimensional structures, several patterned surfaces were developed and replicated in PS to evaluate the role of simultaneous topographic cues at micro/nano scale, in controlling the shape and orientation of a pre-osteoblastic stem cell lineage, MG-63.

The effect of structure height (low, high and variable) on cell development was evaluated by three cylinder based pillar patterns: woodpile pillars, concentric pillars and variable pillars. Cell orientation induced by micro and nano topography was to be assessed by the previously presented beams and dash design.

13.1.1. WOODPILE PILLARS

The first, of four different patterns, was composed by an array of 12µm cylinders fabricated following a woodpile pattern similar to Figure 30. A cylinder shape rather than single voxel extrusion was used for this and other designs since it allowed for higher aspect ratio objects than vertical voxels such previously presented at Figure 31.

Three dimensional models, SEM image and pattern parameters are displayed in Figure 32 and can consulted at Table 6, respectably:

Table 6- *Woodpile pillars pattern fabrication parameters.*

Pattern		Object			Fabrication time (minutes)
Size (μm^2)	Array (units)	Height (µm)	Diameter (µm)	Spacing (µm)	
250×250	25×25	12	6	4	~100

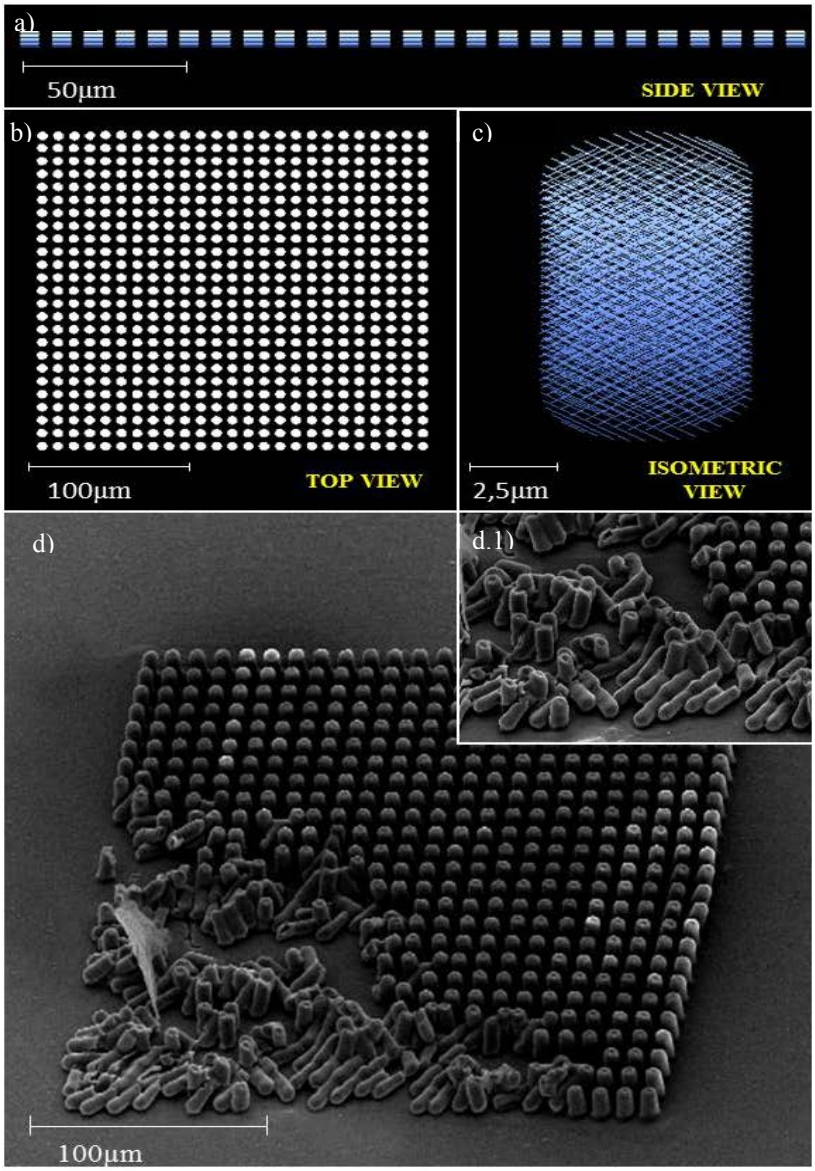

Figure 32- Three dimensional concept model and SEM image of the woodpile pillars pattern. a) Side view. b) Top view. c) Isometric view of a single woodpile cylinder. d) SEM image of the finished pattern with a partially collapsed area. d.1) Higher magnification of the collapsed pillars.

13.1.2. CONCENTRIC PILLARS

The second pattern was composed of 3µm cylinders, fabricated by stacking evenly spaced concentric voxels. Three dimensional models, SEM image and pattern parameters are displayed at Figure 33 and can consulted at Table 7, respectably:

Table 7 - *Concentric pillars pattern fabrication parameters.*

Pattern		Object			Fabrication Time (minutes)
Size (μm^2)	Array (units)	Height (µm)	Diameter (µm)	Spacing (µm)	
600×400	60×40	3	5	5	~200

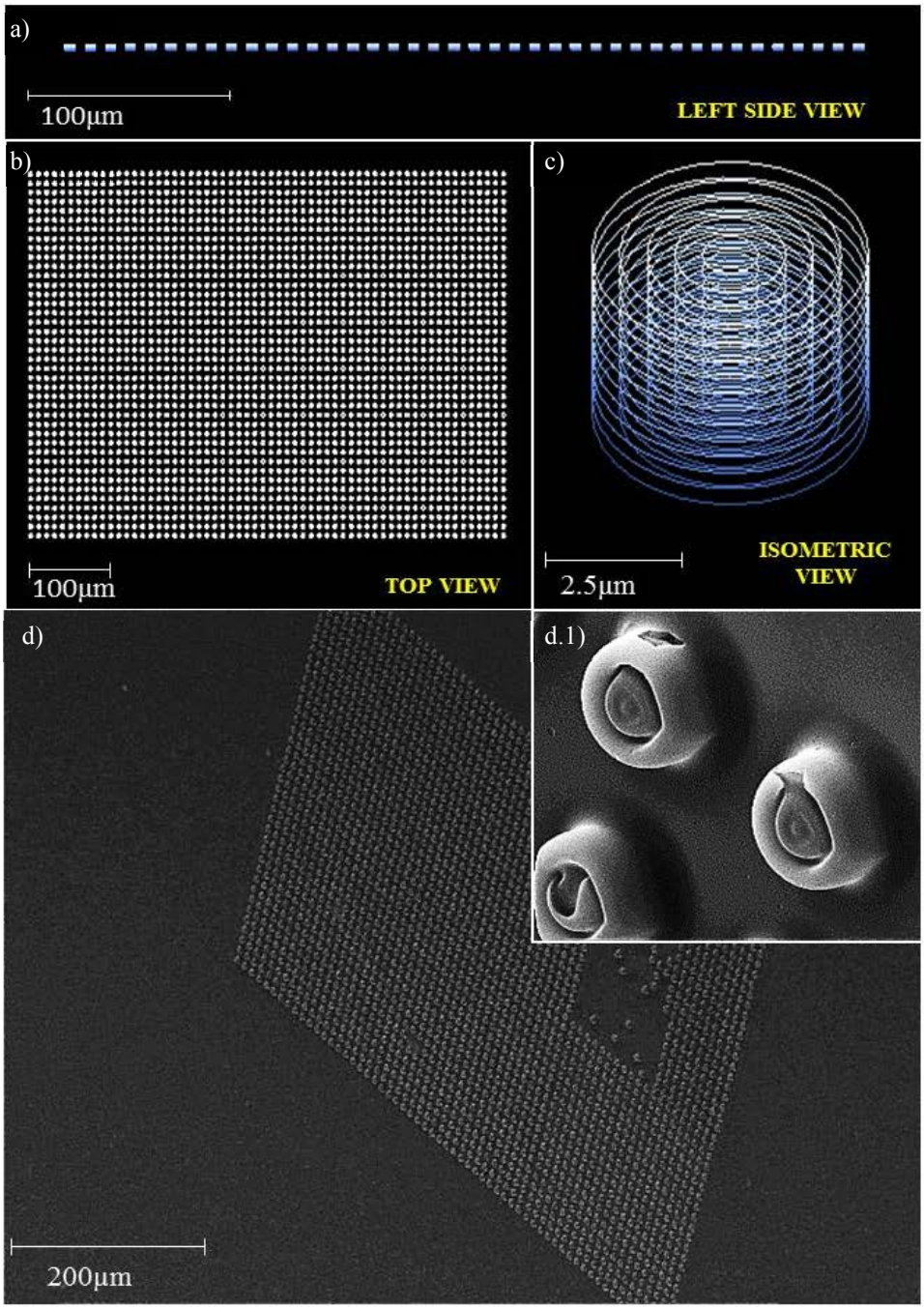

Figure 33 - Three dimensional concept model and SEM image of the concentric pillars pattern. a) Side view. b) Top view. c) Isometric view of a single concentric cylinder. d) SEM image of the finished pattern d.1) Higher magnification of the pillars.

13.1.2.1. VARIABLE PILLARS

The third pattern was a ramp-like pattern containing pillars with variable heights, ranging from 3 at the edges to 15µm in the middle section. Three dimensional models, SEM image and pattern parameters are displayed at Figure 34 and can consulted at Table 8, respectably:

Table 8- *Variable pillars pattern fabrication parameters.*

Pattern		Object					
Size (μm^2)	Array (units)	Height (µm)			Diameter (µm)	Spacing (µm)	Fabrication time (minutes)
		Min.	Max.	Increment			
380×400	38×40	3	15	0.6	5	5	~350

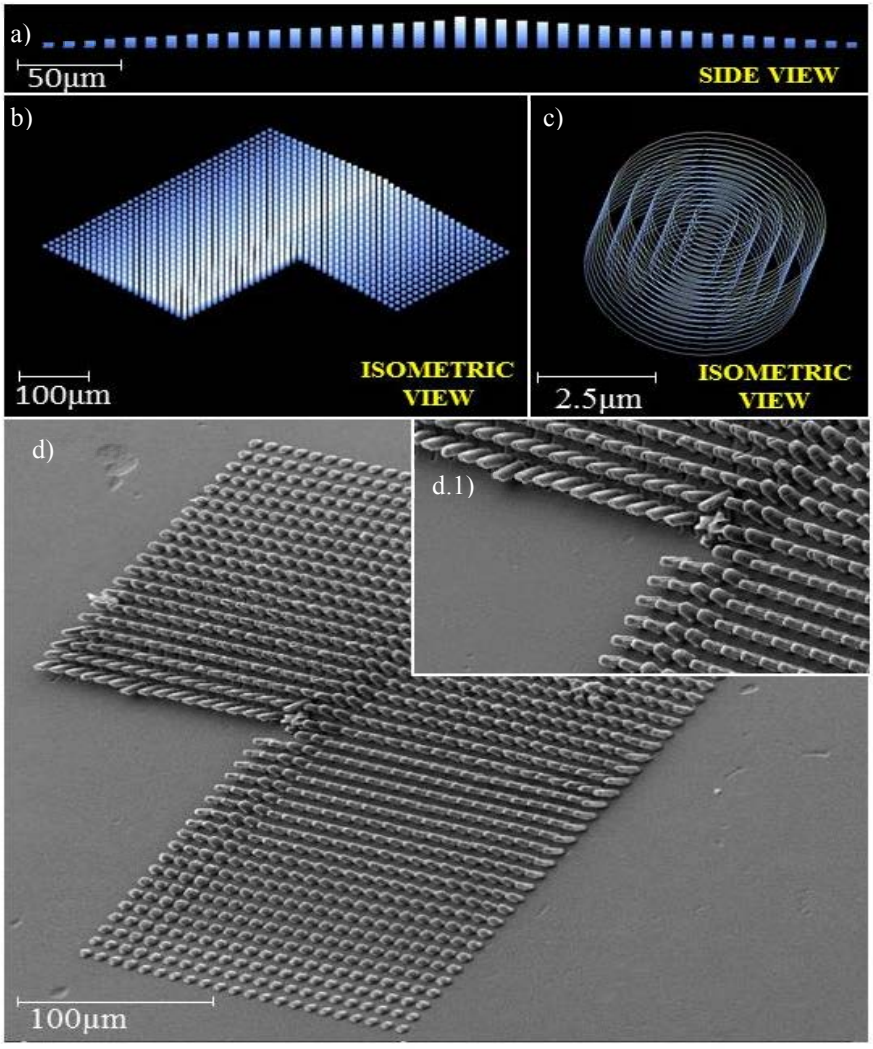

Figure 34 - Three dimensional concept model and SEM image of the variable pillars pattern. a) Side view. b) Top view. c) Isometric view of a concentric cylinder. d) SEM image of the finished pattern d.1) Higher magnification of the pillars.

The fourth and last pattern was the beams and dashes structure, whose 3D models, SEM images and pattern parameters were previously described in chapter I of *Technical Setup and Optimizations: Mould Optimization, page 35*.

13.2. BIOLOGICAL ASSAY

13.2.1. CYLINDER PATTERNS

All of the patterned substrates were seeded and expanded for 24 and 72 hours. SEM images of the first analysed pattern, woodpile pillars, (Figure 32.d), revealed fabrication defects in the lower left section. This was not corrected since it presented an opportunity to study the effect of a chaotic geometry in the same pattern.

Figure 35 depicts the fluorescence images and a merged brightfield composite after for three distinct regions: reference area, patterned surface and the collapsed section after 72h:

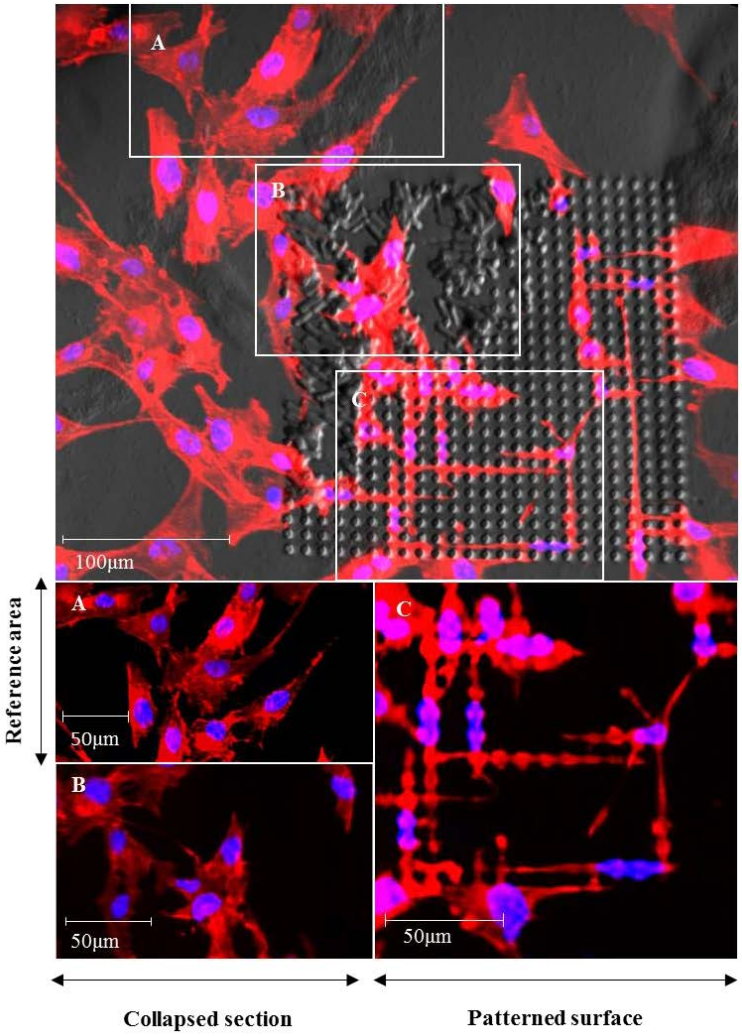

.Figure 35 – 72h fluorescence images for woodpile pillars with collapsed section. Red: F- actin stained with Phalloidin 355. Blue: Nuclear staining with DAPI 594. a) Composite image resultant from bright field and Fluorescence images, divided into three regions: A, B and C, corresponding to Reference area, collapsed section and patterned surface respectably. A) Further magnification of fluorescence image on the reference area. B) Collapsed Section. C) Patterned surface.

Visual inspection of the different areas reveal a distinct shift in cellular morphology between both reference and collapsed area and the patterned surface. The

majority of cells positioned within the pillar area adopted an elongated shape spreading extensively across the pillars, however a few cells still retained a rounded shape. Cells within the collapsed region and the reference area have a similar morphology and show no significant differences.

Unlike the previous design, cells expanded in the concentric pillars pattern (Figure 33), seemed to have experienced a different strength of contact guidance, as no apparent significant change in morphology was detected between reference and the patterned surface. Figure 36 depicts the fluorescence images and a merged brightfield composite for a reference area and patterned surface after 72h:

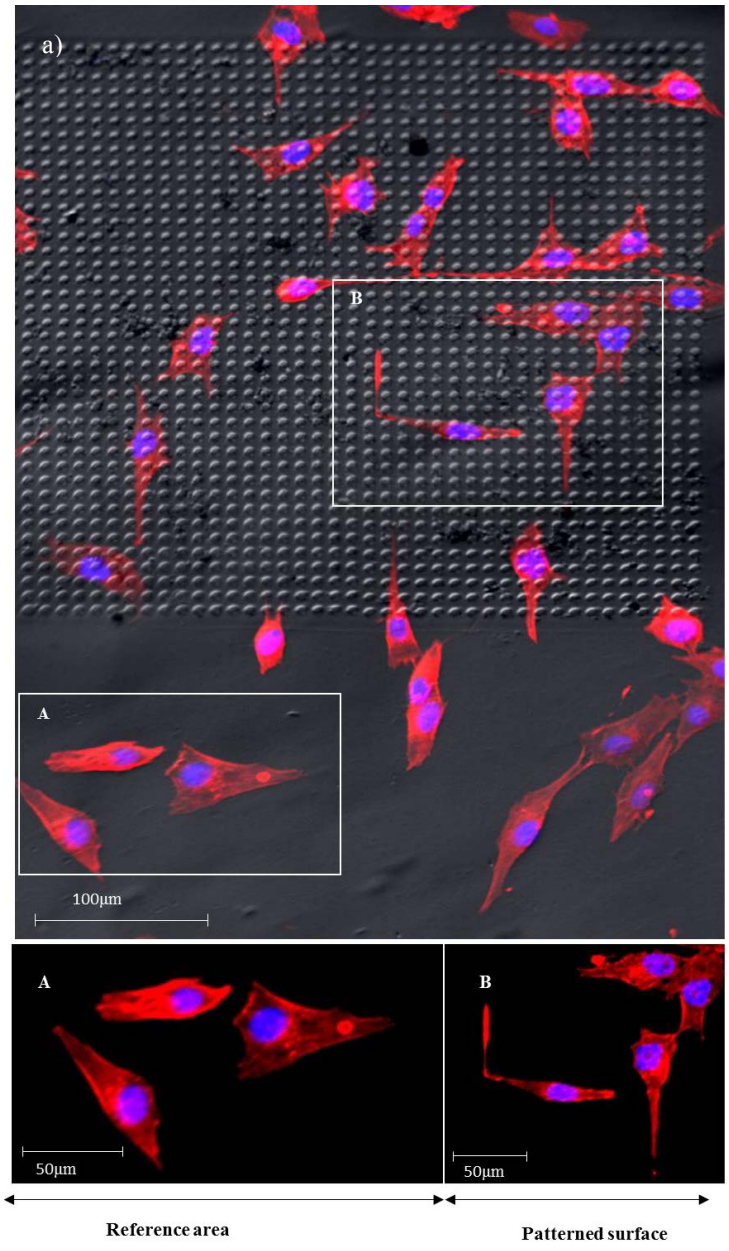

.Figure 36 - 72h fluorescence images for concentric pillars. Red: F- actin stained with Phalloidin 355. Blue: Nuclear staining with DAPI 594. a) Composite image resultant from bright field and Fluorescence images, divided into two regions: A and B, corresponding to Reference area, and patterned surface respectably. A) Further magnification of the reference area. B) Patterned surface.

The last pillar patterned, variable pillars (Figure34) was meant to detect the minimum height required to induce the behaviour seen in the woodpile pattern (Figure 35).

Figure 37 shows the fluorescence images and a merged brightfield composite of a reference area and both high and low sections of the patterned surface after 72h:

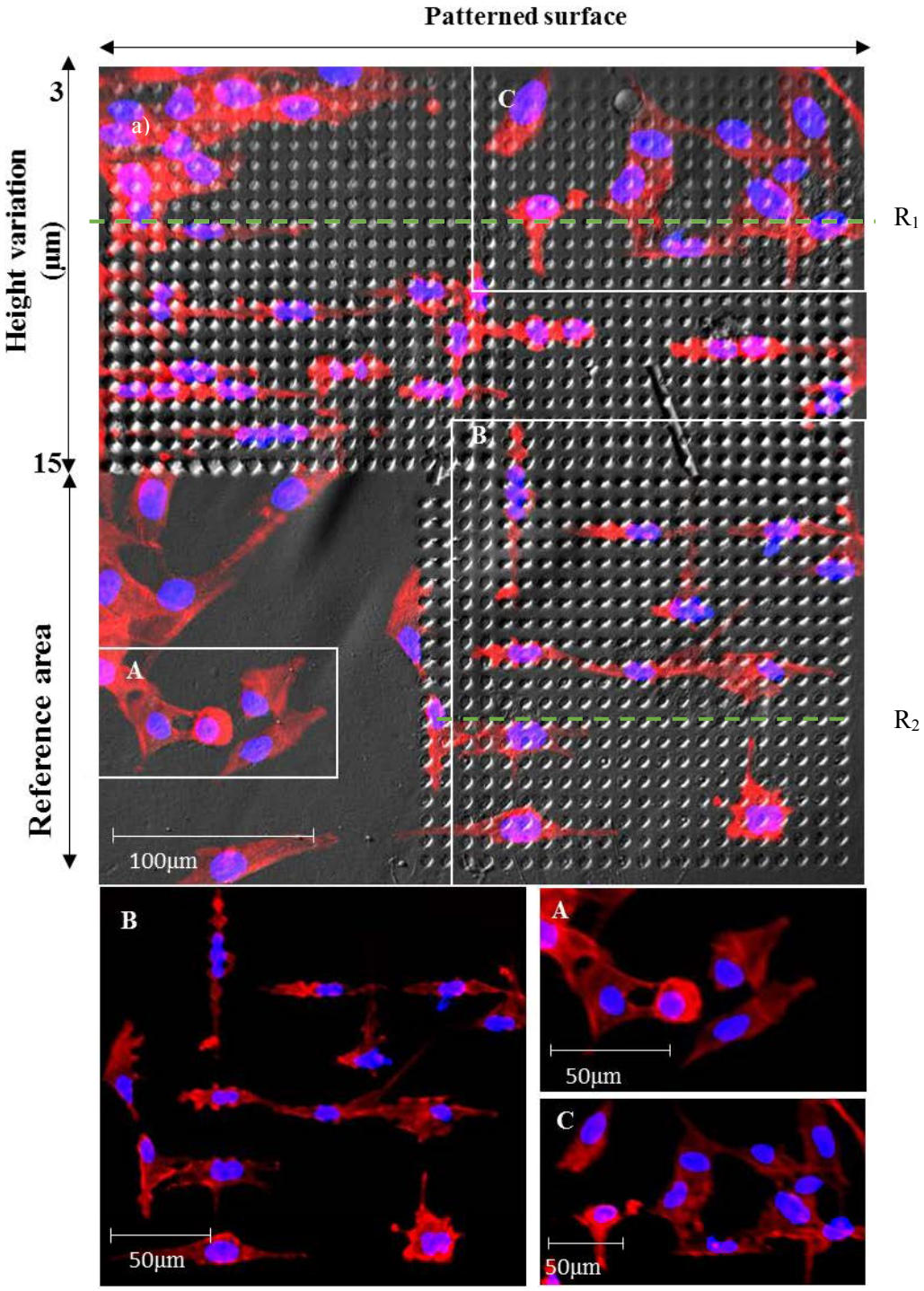

Figure 37- 72h fluorescence images for the variable pillars pattern. Red: F- actin stained with Phalloidin 355. Blue: Nuclear staining with DAPI 594. a) Composite image resultant from bright field and Fluorescence images, divided into three regions: A, B and C, corresponding to Reference area, high pillars section and low pillars surface respectably. A) Further magnification of fluorescence image on the reference area. B) High pillars section. C) Low pillars patterned surface.

Analysis of the composite image (Figure 37.a) shows a shift in cellular morphology in certain areas of the patterned surface. Similarly to the second pattern (Concentric pillars, Figure 36), cells within the region containing small pillars (height <6µm) do not present apparent change shape change when compared to the reference area, Figures 37.A and 37.C, respectably. However, as height increases (R_1 to R_2, Figure37), cells start to adopt an elongated shape and spread across pillars as previously seen on the woodpile pillars, Figure 35. This is a good indication of the existence of a height threshold (around 5-6µm) which is necessary to reach, in order to induce this type of elongation and morphology change.

13.2.2. BEAMS AND DASHES

Cell orientation through contact guidance induce by micro (beams) and nano (dashes) topographies was also evaluated.

Figure 38 depicts brightfield and fluorescence images reference area and the patterned surface after 72h:

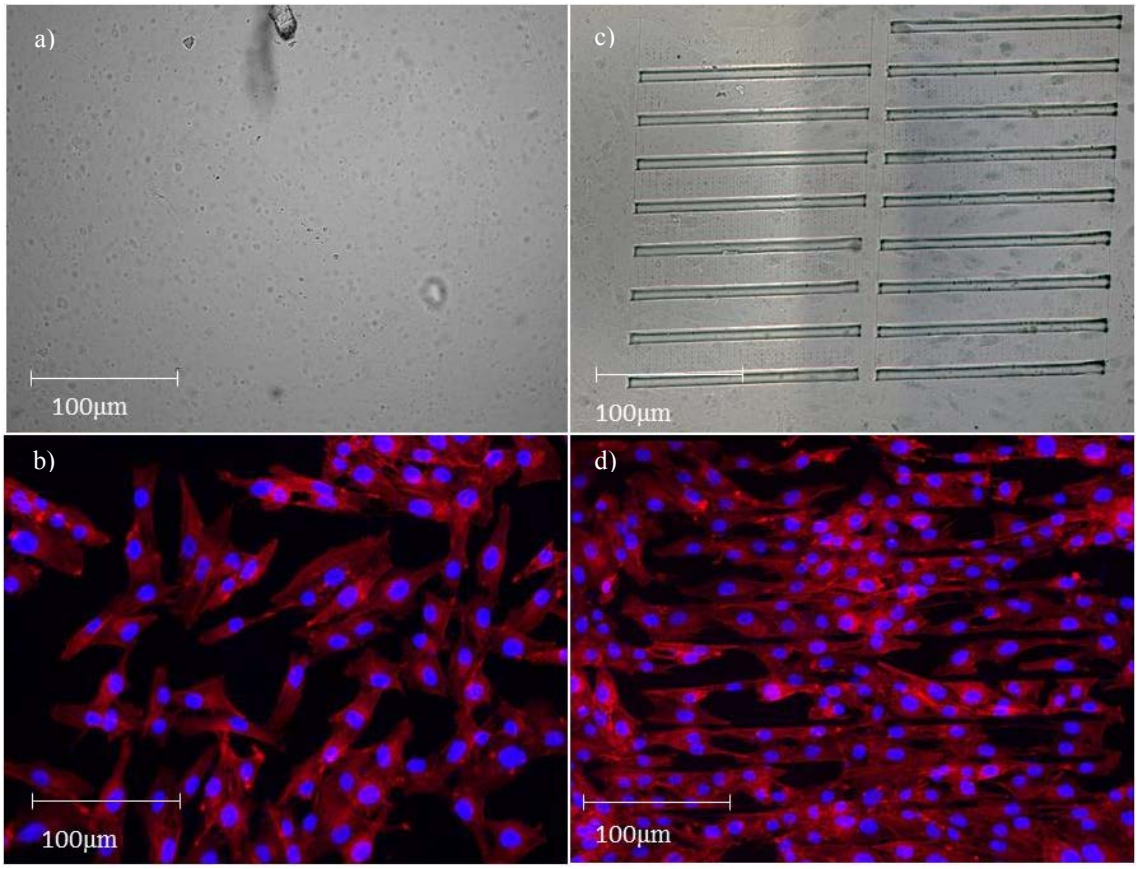

Figure 38-72h fluorescence images for the variable pillars pattern. Red: F- actin stained with Phalloidin 355. Blue: Nuclear staining with DAPI 594. a) Bright field image of the reference area. b) Fluorescence image of reference area. c) Brightfield image of patterned surface. d) Fluorescence image of patterned surface

A visual comparison of the images taken from reference and patterned surface, show a clear difference in cell alignment since cells located within the beams are aligned alongside the beams (Figure 38.d) as opposed to the random orientation of the reference area (Figure 38.b). This behaviour was further illustrated by the composite 24h time point image seen at Figure 39:

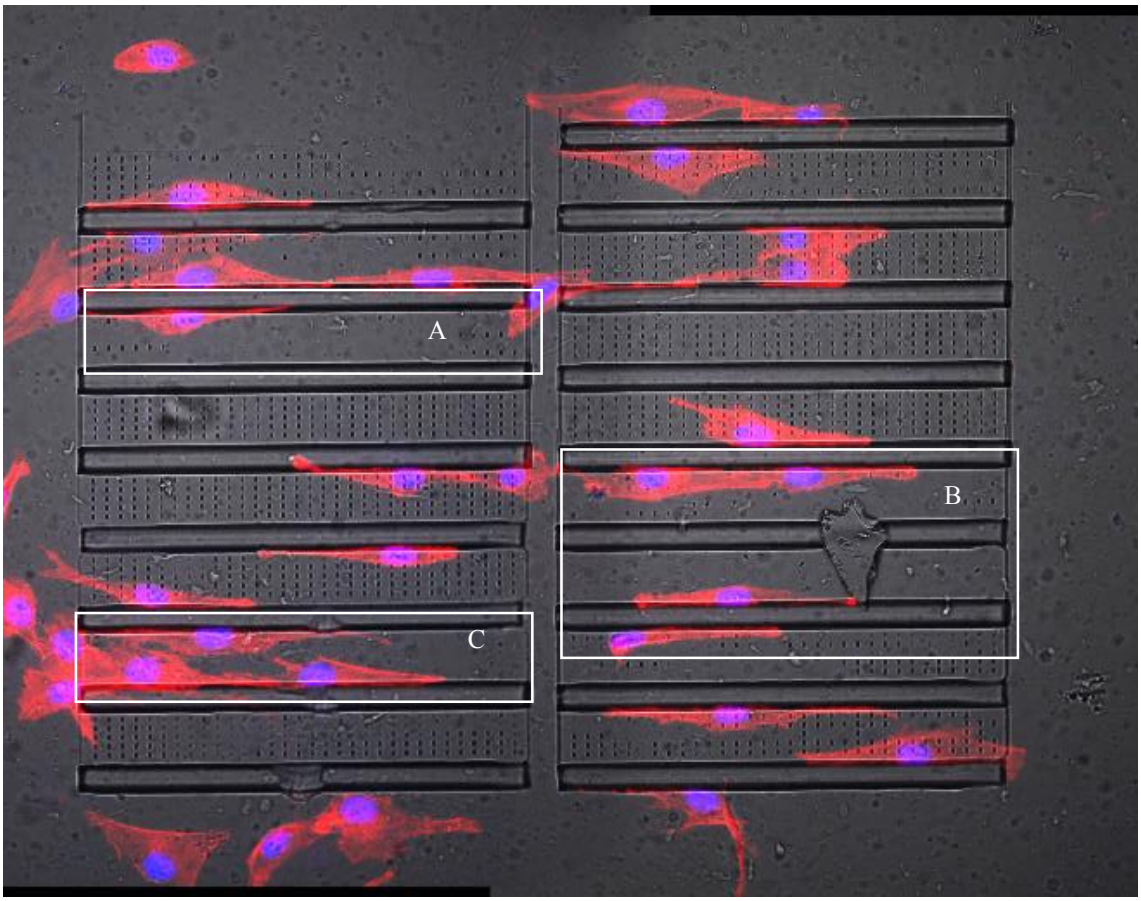

Figure 39 – 24h composite image of the patterned surface. Red: F- actin stained with Phalloidin 355. Blue: Nuclear staining with DAPI 594. Zones A, B and C represent areas of the pattern without dashes.

It is possible to observe that the majority of cells adhered to the beam walls rather that. As time progresses several more cells mimic this behaviour and align into a tissue-like formation (Figure 38.d).

The presence and/or absence of nano cues (*i.e.* dashes) in zones A, B and C (Figure 39) seem to have no apparent impact in cell spreading and orientation.

FUTURE WORK

Parallel to the main project, additional patterned surfaces and large (>100μm) 3D structures, were developed targeting possible applications for single cell analysis and migration studies. Lastly several PLA-based biopolymer formulations were tested\optimized for two photon fabrication.

14. MICROPATTERNING FOR SINGLE CELL ANALYSIS

One of the main challenges of biology is understanding how individual cells process information and respond to stimulus. The average response of a cell was, and often still is, interpreted as the response of all cells in a sample. However, cell-to-cell differences are always present to some degree in any cell population, and in some cases the collective behaviours of a population may not represent the behaviours of any individual cell. By studying single cells it may be possible to ensure a stronger correlation between cause (substrate geometry, growth factors, stress, etc.) and effect (migration, shape or division over time)[190,191].

To assist in cells isolation, several techniques that make use of microdevices, have been reported: microwell arrays, patterning, traps and droplets. Some, such as microwells create physical barriers to isolate cells, while others enclose cells in droplets of low volumes (fL to nL) to create micro-chambers for individual reactions. It is also possible to trap cells at fixed positions by inserting magnetic particles in living cells or using optical tweezers in order to control and direct a trapped cell[190].

The micropatterning of surfaces, is also frequently used to spatially arrange single cells for analysis and its main premise is to provide cytophilic vs. cytophobic regions by modifying surface chemistry and topography of a substrate. To create the patterns, several conventional photolithography techniques may be used however they are usually multistep processes and normally limited to 2D or 2.5D designs[190].

By using TPP fabrication it is possible to overcome some of the design limitations of other processes and construct a fully 3D environment. Following this line of thought, a cage-like structure was developed to serve as a support structure to study single-cell focal point adhesion while stressed by different 3D geometric patterns.

Figure 40 displays SEM images of a 100×10×15µm^3 cage-like structure and various templates, with simple geometric shapes, whose dimensions and approximate fabrication times can be consulted at Table 9:

Table 9 - *Substrate pattern dimensions and approximate fabrication times.*

Object	Dimensions		Approximate fabrication time (minutes)
	Base (µm)	Height (µm)	
Spike	1	5	5
Cylinder	3	12	15
Cone	5	3	10
Blunt cone	5	3	15

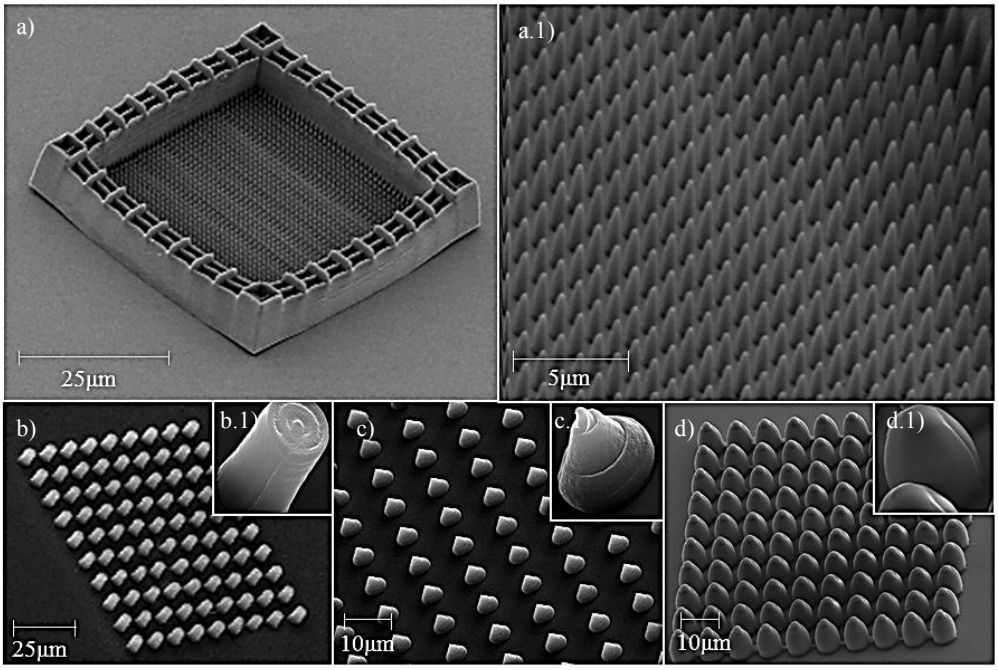

Figure 40 – SEM images of various substrate patterns for possible single cell analysis application. a) Cage-like structure with spikes pattern. b) Cylinder array. c) Sharp cone array. d) Blunt cone array.

Fabricated structures include spikes and cylinders as well as sharp and blunt cones (Figures 40.a, b, c and d respectably).

Single cell analysis usually acquires data from hundreds or thousands of individual cells simultaneously in order not to draw misleading or wrong conclusions from rare cells or stochastic biological noise[190]. As such, it would be necessary to fabricate a large array of the cage-like structures, as seen on Figure 41.

Each well required approximately five minutes to be built and despite being technically possible to scale up the project, by fabricating a much larger array (than the one seen at Figure 41), time constrains and complexity of single cell isolation procedures precluded their use in biological assays.

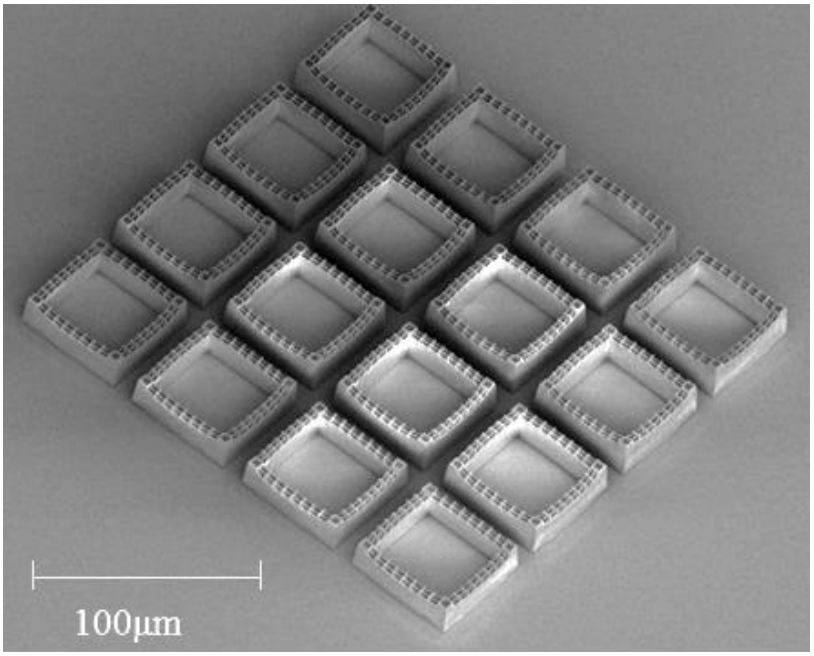

Figure 41 – SEM image of a cage array template for possible application in single cell analysis.

15. MIGRATION STUDIES

Cellular migration is a critical function during many important physiological processes. This is especially relevant during cancer progression, where cellular invasion through the extracellular matrix, blood vessels, and secondary tissues, is a prerequisite for metastasis formation. Some oversimplified invasion protocols, such as the transwell (or Boyden) assay, show a lack of correlation between compounds that inhibit migration and invasion *in vitro* and their efficacy in human clinical trials since they focus mainly on the inhibition of cell motility and disregard other cellular cues [192].

Recreating *in vivo* cellular invasion, which contains an immense 3D structural heterogeneity is very difficult using conventional fabrication techniques. By using TPP it is possible to create complex 3D shapes and therefore provide a more realistic environments.

To assess the possibility of TPP for migration studies, a few test designs, whose parameters can be consulted at Table 10 were fabricated and displayed at Figure 42.

Table 10 - *Object dimensions for structures with possible application for migration studies.*

Object	Dimensions		
	Base (µm)	Height (µm)	Length (µm)
Cone	200	150	-
Half-pipe	50	-	200
Random	-	-	-
Squared hollow pyramid	150	120	-

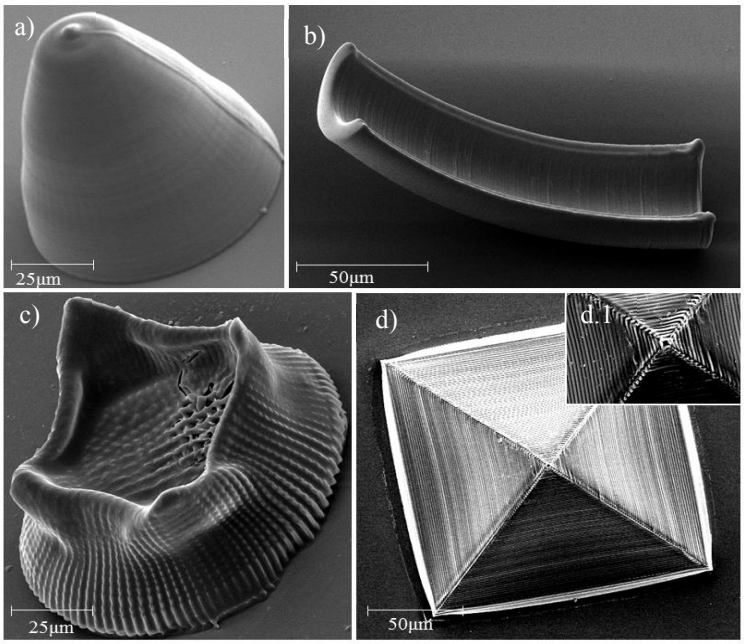

Figure 42 – SEM images of different structures with possible application in migration studies. a) Solid smooth cone. b) Half-pipe. c) Random 3D shape. d) Hollow pyramid. d.1) Greater magnification of the hollow pyramid.

Figure 42 represents SEM images of the programmed structures. These include a cone, a half-pipe, a random 3D object and a squared hollow pyramid (Figures 42.a, b, c and d, respectably).

Each of the designed objects was programmed to supply a different theoretical challenge to cells. A smooth surface and high incline of the cone, the ridged step-like topography of the pyramid, a curved ascending structure of the half pipe and finally an object with more exotic shape. Although not realistic when compared to the actual cell microenvironment, these objects and others, can be seen as another example of TPP fabricated structures with shapes and topographies not easily available for conventional techniques.

Apart from constructing complex 3D shapes, one the greatest advantage of TPP fabrication lies on its great flexibility regarding compatible photoresists. For example, it might be possible to adapt a TPP formulation to include inductive materials that, as shown by Yuan H. and Fernandes H. et al., (2010)[193], are capable of inducing a response similar to autologous tissue, to create more accurate 3D models of cells microenvironment.

16. BIOPOLYMER OPTIMIZATION

Despite exhibiting good performance, commercial photoresists may, at times, not be suitable for cellular and biomolecular patterning applications and their formulation is usually uncertain[194]. Considering the requirements of certain designs, such as high

resolution, transparency at certain wavelengths, viscosity or biocompatibility, custom-made resins may also be developed. These resins can be formulated with specific components to adjust the mechanical and surface properties and different initiators can be chosen to be adapted to the laser wavelength[195].

One approach was to create a hybrid organic/inorganic materials in which the organic portion acts as the photoresist. For instance, resins containing polysiloxane chains with acrylate functional groups have been shown to create a photoresist, capable of 3D stereolithography, with mechanical and optical properties not readily accessible with acrylates alone[196].

Various formulations of a methacrylate terminated PLA biopolymer were synthetized using different solvents, Propylene carbonate (PC) and N-vinylpyrrolidone (NVP). To induce photopolymerization, two photoinitiators, Irgacure 2959 (1-[4-(2-Hydroxyethoxy)-phenyl]-2-hydroxy-2-methyl-1-propane-1-one) and a Benzophenone derivative (4,4'-Bis(dimethylamino)benzophenone) were also added to the pre-polymer mixture. A Poly(trimethylene) carbonate (PTMC) monomer dissolved in PC was additionally tested.

Table 11 – *Polymerization results for different photoresist formulations.*

Sample	Photoresistive biopolymer composition						Polymerization
	Monomers Ratio		Solvents Ratio		Photoinitiators (%Wt.)		
	PLA	**PTMC**	**PC**	**NVP**	**Irgacure 2959**	**Benzophenone**	
Trial 1							
1	50	-	50	-	2	-	Negative
2	35	-	65	-	2	-	Negative
3	20	-	80	-	2	-	Negative
Trial 2							
1	50	-	50	-	5	-	Negative
2	50	-	50	-	7.5	-	Negative
3	50	-	50	-	10	-	Negative
4	50	-	-	50	5	-	Negative
5	50	-	-	50	7.5	-	Negative
6	50	-	-	50	10	-	Negative
Trial 3							
1	-	50	50	-	2.5	-	Negative
2	-	50	50	-	1	-	Negative
3	-	50	50	-	5	-	Negative
Trial 4							
1	50	-	50	-		5	Positive
2	50	-	50	-		7.5	Positive
3	50	-	50	-		10	Negative
4	50		-	50		5	-
5	50	-	-	50		7.5	-
6	50	-	-	50		10	Negative
Trial 5							
1	50	-	50	-	-	2	Positive
2	50	-	50	-	-	5	Positive
3	50	-	50	-	-	7.5	-
4	50	-	-	50	-	2	Positive
5	50	-	-	50	-	5	Positive
6	50	-	-	50	-	7.5	-

All tests were performed using the 63x air objective. The first formulation (Trial 1, table 11) consisting of a PLA/PC monomer mixture with 2%Wt. Irgacure 2959, a common photoinitiator for acrylate based resists. The different samples were prepared using different monomers/solvent ratios (50/50; 35/65; 20/80) to control viscosity. Since polymerization was not achieved and considering the many factors capable of influencing polymerization, such as monomer and initiator concentrations, the remaining trials were performed using a 50/50 monomer to solvent ratio, while varying other parameters.

The kinetics of a photopolymerization system consists of several steps as also observed for other conventional polymer systems: autoacceleration, autodeceleration, primary cyclization, oxygen inhibition, termination, and incomplete reaction of the double bonds[197]. As such, the influence of an UV initiator on the degree of polymerization, may be approximated by the radical chain polymerization process.

In principle, the rate of propagation in radical polymerization can be controlled by changing the initiator and/or monomer concentration. Mathematically, this is illustrated by the first-order rate equation for radical propagation[153]:

$$R_p = -k_p \left(\frac{k_d f[\mathrm{I}]}{k_t} \right)^{1/2} [\mathrm{M}]. \qquad (16\text{-}9)$$

Here, f is the efficiency of an initiator I, k_d is the rate constant of initiator decomposition, k_p is the rate constant for propagation for a monomer M, and k_t is the rate constant for termination.

Since the concentration of photoinitiator is a determinant factor, additional trials were prepared to test the PLA/PC composite (samples 1-3, Trial 2, Table 11) with increasing amounts of photoinitiator concentration (5; 7.5; 10%Wt.). Alternatively, a PLA/NVP mixture was additionally prepared for the same initiator percentages (samples 4-6, Trial 2, Table 11).

Despite raising photoinitiator concentration and replacing PC with NVP (a reactive diluent, shown to increase the polymerization rate in acrylate monomers by reducing the inhibition of free radical photopolymerization by atmospheric oxygen[198]), both cases have shown no signs of polymerization.

In a parallel test (Trial 3, Table 11), a PTMC/PC formulation with increasing amounts of Irgacure 2959 initiator (5; 7.5; 10%Wt.), had similar negative results.

The continued negative results, led to a re-evaluation of the photoinitiator properties and it was verified that its absorption spectra, 200-380nm (Appendix 16.4 –

Figure 48), did not perfectly match the *Photonic Professional* system, whose laser source emitted at 780nm, thus the local excitation due to two photon absorption was 390nm (as illustrated at the Jabłoński diagram in Figure 1, page 10). A new photoinitiator was selected, a Benzophenone derivative, with an absorption spectra peak near 380nm (Appendix 16.5 – Figure 49) and a known polymerization mechanism for acrylate-based resists[199].

By switching to a new photoinitiator, polymerization was readily achieved. Figures 44.a and b depict live images of the PLA/PC composite polymerization with 7.5 and 5% Wt. of Benzophenone (samples 2 and 1, Trial 4, Table 11), respectably:

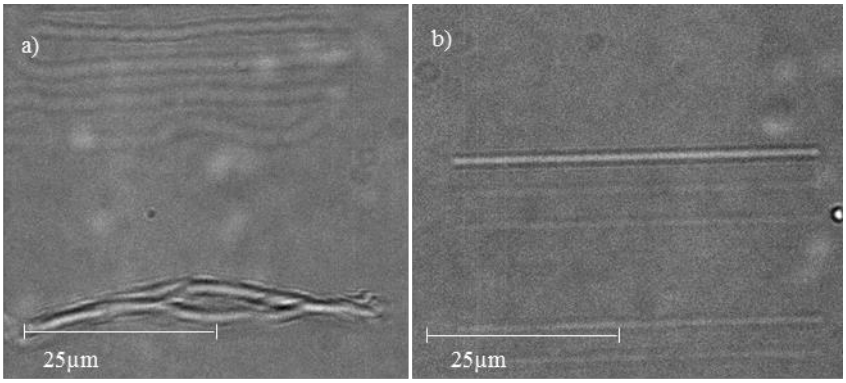

Figure 43 – Live image of polymerization of a PLA/PC composite. a) PLA/PC with 5% Benzophenone initiator. b) PLA/PC with 7.5% imitator.

It is clear that the PLA/PC mixture containing 5%Wt. initiator (Figure 44.b) presents more stable voxels as opposed to the 7.5%Wt. which appear deformed. The PLA/NVP (5 and 7.5% Wt.) could not be properly assessed due to interface finding errors.

Mixtures with 10% initiator had negative results for both PLA/PC and PLA/NVP composites, which is not unexpected since there have been other reports of photoinitiator efficiency, in free radical polymerisations, to decrease beyond a certain optimum concentration[200]. Further increase of initiator concentration was not desirable since the inactivated residues, or by-products (free radicals) of initiators, has been shown to have cytotoxic effects, after certain concentrations[201,202].

There are three polymerization steps *(i.e.*, initiation, propagation, and termination). During initiation phase , the photoinitiator is decomposed into a pair of free radicals upon UV exposure (equation 5.3.1-3).When a large amount, of equally distributed, photoinitiator is present, the radicals can re-combine before initiating a chain. This results in most of the C=C double bonds being converted by photoinitiator radicals, rather than secondary monomer radicals and therefore the reaction might be terminated after this step. Alternatively, a low amount of initiator, may more easily induce chain

polymerization of the C=C double bonds and propagation occur as described in equation 5.3.1-5[197].

To optimize photoinitiator concentration a new experiment was conducted to refine PLA/PC and PLA/NVP formulations with 2, 5 and 7.5% Wt. of Benzophenone initiator.

The results for 7.5% Wt. initiator were not possible to confirm due to interface finding issues. Figures 44.a, b, c and d represent SEM images of the successful polymerization events, samples 1, 2, 4 and 5 (Trial 5, Table 11), respectably:

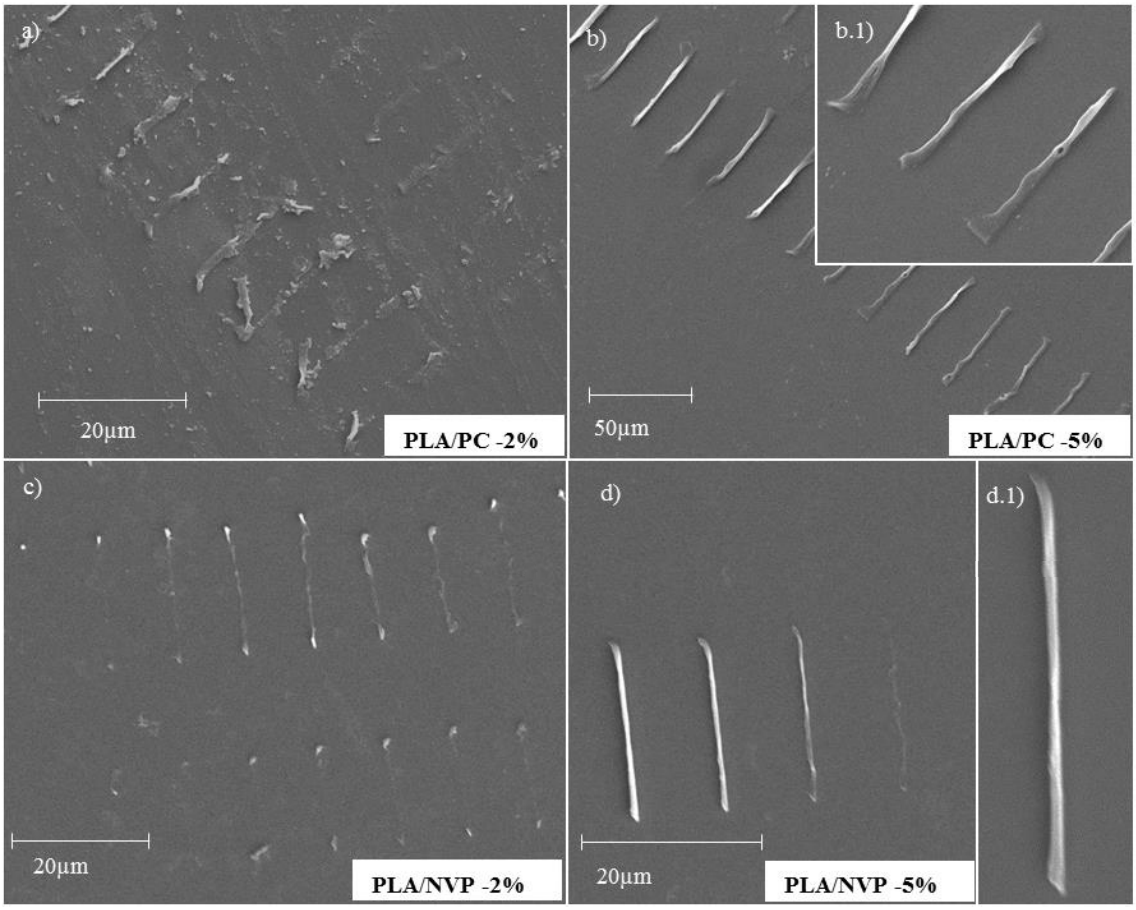

Figure 44- SEM images depicting the results from trial 5 (samples 1, 2, 4 and 5; table 8). a) PLA/PC with 2% Benzophenone. b) PLA/PC with 5% initiator. b.1) Further magnification. c) PLA/NVP with 2% initiator. d) PLA/NVP with 5% initiator. d.1) Further magnification.

As seen on Figure 44, the best results have been obtained using the PLA/NVP and PLA/PC formulation with 5%Wt. Benzophenone. Despite achieving polymerization, the samples with 2% Wt. initiator were less robust and in the case of the PLA/PC composite, voxels appear fragmented. This might have been due to fabrication parameters not being tuned for those particular composition or due to the myriad of factors that can influence polymerization efficiency. Also, given the possible cytotoxicity of high photoinitiator concentration, further usage of this formulation for cellular applications,

might require an extra “ageing” step, in a solvent bath, to remove, or minimize harmful by-products.

Due to time restraints, further optimization of the PLA formulation for micro structures fabrication and proper polymer characterization, such as swelling characteristics, cytotoxicity and cell adhesion were not possible. Nevertheless, these results show that it is indeed possible to use a wider range of materials than those commercially available for two photon polymerization and tailor them to user specifications.

CONCLUSION

Fabricating objects using TPP can be a challenging process. Depending on the complexity of the design, a plethora of settings must be experimentally tested by trial and error. To determine parameters such as Z layer and XY voxel distances it is necessary to consider the type of photoresist, laser settings and writing speeds (since these influence voxel size), along with other operational parameters.

One of the factors that most influences parameter choice is the fabrication time. Given the relatively low writing speed of the system, which is usually set around 150µm/s, it is necessary to make a compromise between stability and speed. This leads to a reduction of supportive layers in order to lower fabrication times and can sometimes lead to collapse.

Due to time restraints, further increase in design complexity was not feasible. As such, simplified models were used to assess the simultaneous effect of nano (in the form of dashes) and micro cues (beams) on cell motility and orientation. Preliminary results showed that, for this particular geometry, the effect of micro cues has a greater prevalence over nano features, by successfully "forcing" cells to align alongside the structures and form a tissue-like conformation in between beams. However, these particular nano cues did not seem that have a particular effect.

The cylinder based patterns have hinted at a threshold limit to object height that is capable of inducing a morphological changes in cell shape. Although similar results have been obtained by other authors, albeit using different cell lineages, fabrication methods and fixed height[188], these results illustrate the potential of this fabrication method for basic science studies.

Despite TPP being a very powerful technique regarding the fabrication of complex three dimensional shapes, printing of micro and nano structures is usually a slow process and therefore it is practically impossible to rely upon on an industrial level. However, the next generation of TPP based laser lithography systems have recently been launched and promise tremendous advances.

These new devices, such as recently announced *Photonic Professional GT* (NanoScribe, GmbH), implement a set of galvanic mirror, similar to those used in scanning units of CD and DVD drives, to increase printing speed a hundred fold (up to 100mm/s) and allow fabrication of objects from nano to millimetre scale. The accuracy of this new galvo stage is up to 10nm, which is a great improvement when compared to

the coarse stage used in this project which had an accuracy at the micrometre range and often led to fabrication stitching errors[203,204].

The continuous development of software and hardware as well as novel TPP specific biopolymers will surely bring even more applications of two photon polymerization technology in the near future.

REFERENCES

1. Gurtner GC, Werner S, Barrandon Y, Longaker MT. Wound repair and regeneration. *Nature*. 2008;453(7193):314-321. doi:10.1038/nature07039.

2. Gurtner GC, Callaghan MJ, Longaker MT. Progress and Potential for Regenerative Medicine. *Annu Rev Med*. 2007;58(1):299-312. doi:10.1146/annurev.med.58.082405.095329.

3. Baddour J, Sousounis K, Tsonis P. Organ repair and regeneration: An overview. *Birth Defects Res Part C Embryo Today Rev*. 2012;96(1):1-29. doi:10.1002/bdrc.21006.

4. Singer AJ, Clark RA, Adam J. Singer RAFC. Cutaneous wound healing. *N Engl J Med*. 1999;341(10):738-746. doi:10.1056/NEJM199909023411006.

5. Aarabi S, Longaker MT, Gurtner GC. Hypertrophic Scar Formation Following Burns and Trauma: New Approaches to Treatment. *PLoS Med*. 2007;4(9):e234. doi:10.1371/journal.pmed.0040234.

6. Trent JT, Kirsner RS. Wounds and malignancy. *Adv Skin Wound Care*. 2003;16(1):31-34. doi:10.1097/00129334-200301000-00014.

7. Chen F-M, Liu X. Advancing biomaterials of human origin for tissue engineering. *Prog Polym Sci*. 2015. doi:10.1016/j.progpolymsci.2015.02.004.

8. S.Colwell A, T. Longaker M, Lorenz HP. Fetal wound healing. *Front Biosci*. 2003;8:1240-1248.

9. Atala A. The Jay and Margie Grosfeld Lecture "Regenerative Medicine Strategies." *J Pediatr Surg*. doi:10.1016/j.jpedsurg.2011.10.013.

10. Chan BP, Leong KW. Scaffolding in tissue engineering: general approaches and tissue-specific considerations. *Eur Spine J*. 2008;17(S4):467-479. doi:10.1007/s00586-008-0745-3.

11. Langer R, Tirrell DA. Designing materials for biology and medicine. *Nature*. 2004;428(6982):487-492. doi:10.1038/nature02388.

12. Karp JM, Langer R. Development and therapeutic applications of advanced biomaterials. *Curr Opin Biotechnol*. 2007;18(5):454-459. doi:10.1016/j.copbio.2007.09.008.

13. Spector M. Biomaterials-based tissue engineering and regenerative medicine solutions to musculoskeletal problems. *Swiss Med Wkly*. 2006;136(19-20):293-301. doi:2006/19/smw-11310.

14. Cao Y, Vacanti JP, Paige KT, Upton J, Vacanti CA. Transplantation of Chondrocytes Utilizing a Polymer-Cell Construct to Produce Tissue-Engineered Cartilage in the Shape of a Human Ear. *Plast Reconstr Surg*. 1997;100(2). http://journals.lww.com/plasreconsurg/Fulltext/1997/08000/Transplantation_of_Chondrocytes_Utilizing_a.1.aspx.

15. Gonfiotti A, Jaus MO, Barale D, et al. The first tissue-engineered airway transplantation: 5-year follow-up results. *Lancet (London, England)*. 2014;383(9913):238-244. doi:10.1016/S0140-6736(13)62033-4.

16. Monici,M., Cialda F. The Role of Physical Factors in Cell Differentiation, Tissue Repair and Regeneration. In: J.Davies, ed. *Tissue Regeneration - From Basic Biology to Clinical Application*. Intech; 2012:520. doi:10.5772/1334.

17. Bhatia SK. Tissue engineering for clinical applications. *Biotechnol J*. 2010;5(12):1309-1323. doi:10.1002/biot.201000230.

18. Katari R, Peloso A, Orlando G. Tissue Engineering and Regenerative Medicine: Semantic Considerations for an Evolving Paradigm. *Front Bioeng Biotechnol*. 2015;2(January):1-6. doi:10.3389/fbioe.2014.00057.

19. Fisher MB, Mauck RL. Tissue engineering and regenerative medicine: recent innovations and the transition to translation. *Tissue Eng Part B Rev*. 2013;19(1):1-13. doi:10.1089/ten.TEB.2012.0723.

20. Chen F-M, Zhao Y-M, Jin Y, Shi S. Prospects for translational regenerative medicine. *Biotechnol Adv*. 2012;30(3):658-672. doi:10.1016/j.biotechadv.2011.11.005.

21. Shizuru JA, Negrin RS, Weissman IL. Hematopoietic Stem and Progenitor Cells: Clinical and Preclinical Regeneration of the Hematolymphoid System. *Annu Rev Med*. 2005;56(1):509-538. doi:10.1146/annurev.med.54.101601.152334.

22. Meier JJ, Bhushan A, Butler PC. The potential for stem cell therapy in diabetes. *Pediatr Res*. 2006;59(4 Pt 2):65R - 73R. doi:10.1203/01.pdr.0000206857.38581.49.

23. Sirabella D, Cimetta E, Vunjak-Novakovic G. "The state of the heart": Recent advances in engineering human cardiac tissue from pluripotent stem cells. *Exp Biol Med*. 2015;240(8):1008-1018. doi:10.1177/1535370215589910.

24. Stem Cell Basics : Stem Cell Information. *US Dep Heal Hum Serv*. 2015. http://stemcells.nih.gov/info/basics/Pages/Default.aspx. Accessed March 1, 2015.

25. Appasani K, Raghu K. A, eds. *Stem Cells & Regenerative Medicine : From Molecular Embryology to Tissue Engineering*. Vol 1. Humana Press; 2011. doi:10.1007/978-1-60761-860-7.

26. Takahashi K, Yamanaka S. Induction of Pluripotent Stem Cells from Mouse Embryonic and Adult Fibroblast Cultures by Defined Factors. *Cell*. 2006;126(4):663-676. doi:10.1016/j.cell.2006.07.024.

27. Wang WE, Chen X, Houser SR, Zeng C. Potential of cardiac stem/progenitor cells and induced pluripotent stem cells for cardiac repair in ischaemic heart disease. *Clin Sci*. 2013;125(7):319-327. doi:10.1037/a0030561.Striving.

28. Li K, Zhu S, Russ H a., et al. Small molecules facilitate the reprogramming of mouse fibroblasts into pancreatic lineages. *Cell Stem Cell*. 2014;14(2):228-236. doi:10.1016/j.stem.2014.01.006.

29. Zhu S, Rezvani M, Harbell J, et al. Mouse liver repopulation with hepatocytes generated from human fibroblasts. *Nature*. 2014;508(7494):93-97. doi:10.1038/nature13020.

30. Seaberg RM, Van der Kooy D. Stem and progenitor cells: the premature desertion of rigorous definitions. *Trends Neurosci*. 2003;26(3):125-131. doi:10.1016/S0166-2236(03)00031-6.

31. Vertes AA, Qureshi N, Caplan AI, Babiss LE, eds. *Stem Cells in Regenerative Medicine : Science, Regulation and Business Strategies*. Wiley Blackwell; 2015.

32. Bajada S, Mazakova I, B. Richardson J, Ashammakhi, Nureddin. Updates on stem cells and their applications in regenerative medicine. *J Tissue Eng Regen Med*. 2010;4(7):169-183. doi:10.1002/term.

33. Nizzardo M, Simone C, Falcone M, et al. Direct reprogramming of adult somatic cells into other lineages: Past evidence and future perspectives. *Cell Transplant*. 2013;22(6):921-944. doi:10.3727/096368912X657477.

34. Martin GR. Isolation of a pluripotent cell line from early mouse embryos cultured in medium conditioned by teratocarcinoma stem cells. *Proc Natl Acad Sci U S A*. 1981;78(12):7634-7638. doi:10.1073/pnas.78.12.7634.

35. Thomson JA, Itskovitz-Eldor J, Shapiro SS, et al. Embryonic Stem Cell Lines Derived from Human Blastocysts. *Science (80-)*. 1998;282(5391):1145-1147. doi:10.1126/science.282.5391.1145.

36. Metallo CM, Vodyanik MA, De Pablo JJ, Slukvin II, Palecek SP. The response of human embryonic stem cell-derived endothelial cells to shear stress. *Biotechnol Bioeng*. 2008;100(4):830-837. doi:10.1002/bit.21809.

37. Altman GH, Horan RL, Martin I, et al. Cell differentiation by mechanical stress. *FASEB J*. 2002;16(2):270-272. doi:10.1096/fj.01-0656fje.

38. Yim EKF, Pang SW, Leong KW. Synthetic nanostructures inducing differentiation of human mesenchymal stem cells into neuronal lineage. *Exp Cell Res*. 2007;313(9):1820-1829. doi:10.1016/j.yexcr.2007.02.031.

39. Geiger B, Spatz JP, Bershadsky AD. Environmental sensing through focal adhesions. *Nat Rev Mol Cell Biol*. 2009;10(1):21-33. doi:10.1038/nrm2593.

40. Kshitiz, Park J, Kim P, et al. Control of stem cell fate and function by engineering physical microenvironments. *Integr Biol (Camb)*. 2012;4(9):1008-1018. doi:10.1039/c2ib20080e.

41. Eisenberg LM, Eisenberg CA. Stem cell plasticity, cell fusion, and transdifferentiation. *Birth Defects Res Part C Embryo Today Rev*. 2003;69(3):209-218. doi:10.1002/bdrc.10017.

42. Turhan AG. Plasticity of adult stem cells. *Transfus Clin Biol*. 2003;10(3):103-108.

43. Wozniak MA, Chen CS. Mechanotransduction in development: a growing role for contractility. *Nat Rev Mol Cell Biol*. 2009;10(1):34-43. doi:10.1038/nrm2592.

44. Orr AW, Helmke BP, Blackman BR, Schwartz MA. Mechanisms of mechanotransduction. *Dev Cell*. 2006;10(1):11-20. doi:10.1016/j.devcel.2005.12.006.

45. Badylak SF. Xenogeneic extracellular matrix as a scaffold for tissue reconstruction. *Transpl Immunol*. 2004;12(3-4):367-377. doi:10.1016/j.trim.2003.12.016.

46. Pan Z, Ding J. Poly(lactide-co-glycolide) porous scaffolds for tissue engineering and regenerative medicine. *Interface Focus*. 2012;2(3):366-377. doi:10.1098/rsfs.2011.0123.

47. Okamoto M, John B. Synthetic biopolymer nanocomposites for tissue engineering scaffolds. *Prog Polym Sci*. 2013;38(10-11):1487-1503. doi:10.1016/j.progpolymsci.2013.06.001.

48. Chow D, Nunalee ML, Lim DW, Simnick AJ, Chilkoti A. Peptide-based biopolymers in biomedicine and biotechnology. *Mater Sci Eng R Reports*. 2008;62(4):125-155. doi:10.1016/j.mser.2008.04.004.

49. Cui F-Z, Li Y, Ge J. Self-assembly of mineralized collagen composites. *Mater Sci Eng R Reports*. 2007;57(1-6):1-27. doi:10.1016/j.mser.2007.04.001.

50. Badylak SF. The extracellular matrix as a scaffold for tissue reconstruction. *Semin Cell Dev Biol*. 2002;13(5):377-383. doi:10.1016/S1084952102000940.

51. Seal B. Polymeric biomaterials for tissue and organ regeneration. *Mater Sci Eng R Reports*. 2001;34(4-5):147-230. doi:10.1016/S0927-796X(01)00035-3.

52. Lutolf MP, Hubbell JA. Synthetic biomaterials as instructive extracellular microenvironments for morphogenesis in tissue engineering. *Nat Biotechnol*. 2005;23(1):47-55. doi:10.1038/nbt1055.

53. Baptista PM, Siddiqui MM, Lozier G, Rodriguez SR, Atala A, Soker S. The use of whole organ decellularization for the generation of a vascularized liver organoid. *Hepatology*. 2011;53(2):604-617. doi:10.1002/hep.24067.

54. L'Heureux N, McAllister TN, de la Fuente LM. Tissue-engineered blood vessel for adult arterial revascularization. *N Engl J Med*. 2007;357(14):1451-1453. doi:10.1056/NEJMc071536.

55. Shin'oka T, Imai Y, Ikada Y. Transplantation of a Tissue-Engineered Pulmonary Artery. *N Engl J Med*. 2000;343(7):532-533. doi:10.1056/NEJM200009283431303.

56. Atala A, Bauer SB, Soker S, Yoo JJ, Retik AB. Tissue-engineered autologous bladders for patients needing cystoplasty. *Lancet*. 2006;367(9518):1241-1246. doi:10.1016/S0140-6736(06)68438-9.

57. Ott HC, Matthiesen TS, Goh S-K, et al. Perfusion-decellularized matrix: using nature's platform to engineer a bioartificial heart. *Nat Med*. 2008;14(2):213-221. doi:10.1038/nm1684.

58. Taylor DA. From stem cells and cadaveric matrix to engineered organs. *Curr Opin Biotechnol*. 2009;20(5):598-605. doi:10.1016/j.copbio.2009.10.016.

59. Petersen TH, Calle EA, Zhao L, et al. Tissue-engineered lungs for in vivo implantation. *Science*. 2010;329(5991):538-541. doi:10.1126/science.1189345.

60. Cortiella J, Niles J, Cantu A, et al. Influence of Acellular Natural Lung Matrix on Murine Embryonic Stem Cell Differentiation and Tissue Formation. *Tissue Eng Part A*. 2010;16(8):2565-2580. doi:10.1089/ten.tea.2009.0730.

61. Wagner DE, Bonvillain RW, Jensen T, et al. Can stem cells be used to generate new lungs? *Ex vivo* lung bioengineering with decellularized whole lung scaffolds. *Respirology*. 2013;18(6):895-911. doi:10.1111/resp.12102.

62. Uygun BE, Soto-Gutierrez A, Yagi H, et al. Organ reengineering through development of a transplantable recellularized liver graft using decellularized liver matrix. *Nat Med*. 2010;16(7):814-820. doi:10.1038/nm.2170.

63. Takeda YS, Xu Q, Takeda, Yuji S.; Xu Q. Fabrication of 2D and 3D Constructs from Reconstituted Decellularized Tissue Extracellular Matrices. *J Biomed Nanotechnol*. 2014;10(12):3631-3637. doi:http://dx.doi.org/10.1166/jbn.2014.1876.

64. Ross EA, Williams MJ, Hamazaki T, et al. Embryonic Stem Cells Proliferate and Differentiate when Seeded into Kidney Scaffolds. *J Am Soc Nephrol*. 2009;20(11):2338-2347. doi:10.1681/ASN.2008111196.

65. Liu C, Liu S, Xu A, Kang Y, Zheng S, Li H. [Preparation of whole-kidney acellular matrix in rats by perfusion]. *Nan Fang Yi Ke Da Xue Xue Bao*. 2009;29(5):979-982. doi:10.3969/j.issn.1673-8225.2009.38.013.

66. Nakayama KH, Batchelder C a., Lee CI, Tarantal AF. Decellularized Rhesus Monkey Kidney as a Three-Dimensional Scaffold for Renal Tissue Engineering. *Tissue Eng Part A*. 2010;16(7):2207-2216. doi:10.1089/ten.tea.2009.0602.

67. Baptista PM, Orlando G, Mirmalek-Sani SH, Siddiqui M, Atala A, Soker S. Whole organ decellularization - A tool for bioscaffold fabrication and organ bioengineering. *Proc 31st Annu Int Conf IEEE Eng Med Biol Soc Eng Futur Biomed EMBC 2009*. 2009:6526-6529. doi:10.1109/IEMBS.2009.5333145.

68. Zambon JP. Kidney regeneration: Where we are and future perspectives. *World J Nephrol*. 2014;3(3):24. doi:10.5527/wjn.v3.i3.24.

69. Soto-Gutierrez A, Wertheim JA, Ott HC, Gilbert TW. Perspectives on whole-organ assembly: Moving toward transplantation on demand. *J Clin Invest*. 2012;122(11):3817-3823. doi:10.1172/JCI61974.

70. Feinberg AW. Engineered tissue grafts: opportunities and challenges in regenerative medicine. *Wiley Interdiscip Rev Syst Biol Med*. 2012;4(2):207-220. doi:10.1002/wsbm.164.

71. Lee K, Silva EA, Mooney DJ. Growth factor delivery-based tissue engineering: general approaches and a review of recent developments. *J R Soc Interface*. 2011;8(55):153-170. doi:10.1098/rsif.2010.0223.

72. Griffith LG, Naughton G. Tissue Engineering--Current Challenges and Expanding Opportunities. *Science (80-)*. 2002;295(5557):1009-1014. doi:10.1126/science.1069210.

73. Spector M. Novel cell-scaffold interactions encountered in tissue engineering: contractile behavior of musculoskeletal connective tissue cells. *Tissue Eng*. 2002;8(3):351-357. doi:10.1089/107632702760184628.

74. Brien FJO. Biomaterials and scaffolds for tissue engineering. *Mater Today*. 2011;14(3):3-23.

75. Sachlos E, Czernuszka JT. Making tissue engineering scaffolds work. Review: the application of solid freeform fabrication technology to the production of tissue engineering scaffolds. *Eur Cell Mater*. 2003;5:29-39; discussion 39-40.

76. Möller S, Weisser J, Bischoff S, Schnabelrauch M. Dextran and hyaluronan methacrylate based hydrogels as matrices for soft tissue reconstruction. *Biomol Eng*. 2007;24(5):496-504. doi:10.1016/j.bioeng.2007.08.014.

77. Tsioptsias C, Tsivintzelis I, Papadopoulou L, Panayiotou C. A novel method for producing tissue engineering scaffolds from chitin, chitin–hydroxyapatite, and cellulose. *Mater Sci Eng C*. 2009;29(1):159-164. doi:10.1016/j.msec.2008.06.003.

78. Martín L, Alonso M, Girotti A, Arias FJ, Rodríguez-Cabello JC. Synthesis and characterization of macroporous thermosensitive hydrogels from recombinant elastin-like polymers. *Biomacromolecules*. 2009;10(11):3015-3022. doi:10.1021/bm900560a.

79. Pathi SP, Kowalczewski C, Tadipatri R, Fischbach C. A Novel 3-D Mineralized Tumor Model to Study Breast Cancer Bone Metastasis. *PLoS One*. 2010;5(1):e8849. doi:10.1371/journal.pone.0008849.

80. Zhu XH, Arifin DY, Khoo BH, Hua J, Wang C-H. Study of cell seeding on porous poly(d,l-lactic-co-glycolic acid) sponge and growth in a Couette–Taylor bioreactor. *Chem Eng Sci*. 2010;65(6):2108-2117. doi:10.1016/j.ces.2009.12.006.

81. Salerno A, Netti PA, Di Maio E, Iannace S. Engineering of Foamed Structures for Biomedical Application. *J Cell Plast* . 2009;45 (2):103-117. doi:10.1177/0021955X08099929.

82. Gomes ME, Azevedo HS, Moreira AR, Ellä V, Kellomäki M, Reis RL. Starch-poly(epsilon-caprolactone) and starch-poly(lactic acid) fibre-mesh scaffolds for bone tissue engineering applications: structure, mechanical properties and degradation behaviour. *J Tissue Eng Regen Med*. 2008;2(5):243-252. doi:10.1002/term.89.

83. Mooney DJ, Mazzoni CL, Breuer C, et al. Stabilized polyglycolic acid fibre-based tubes for tissue engineering. *Biomater Silver Jubil Compend*. 2006;17(2):129-138. doi:10.1016/B978-008045154-1.50017-4.

84. Liu X, Ma PX. Phase separation, pore structure, and properties of nanofibrous gelatin scaffolds. *Biomaterials*. 2009;30(25):4094-4103. doi:10.1016/j.biomaterials.2009.04.024.

85. Nichols MD, Scott E a., Elbert DL. Factors affecting size and swelling of poly(ethylene glycol) microspheres formed in aqueous sodium sulfate solutions without surfactants. *Biomaterials*. 2009;30(29):5283-5291. doi:10.1016/j.biomaterials.2009.06.032.

86. Lee SH, Seong SC, Lee JH, et al. Porous Polymer Prosthesis for Meniscal Regeneration. *Key Eng Mater*. 2007;342-343(Advanced Biomaterials VII):33-36. doi:10.4028/www.scientific.net/KEM.342-343.33.

87. Wang Y, Liu L, Guo S. Characterization of biodegradable and cytocompatible nano-hydroxyapatite/polycaprolactone porous scaffolds in degradation in vitro. *Polym Degrad Stab*. 2010;95(2):207-213. doi:10.1016/j.polymdegradstab.2009.11.023.

88. Mu Y, Yubao L, Wang M, Xu F, Zhang X, Tian Z. Novel Method to Fabricate Porous n-HA/PVA Hydrogel Scaffolds. *Mater Sci Forum*. 2006;510-511:878-881. doi:10.4028/www.scientific.net/MSF.510-511.878.

89. Sinha A, Guha A. Biomimetic patterning of polymer hydrogels with hydroxyapatite nanoparticles. *Mater Sci Eng C*. 2009;29(4):1330-1333. doi:10.1016/j.msec.2008.10.024.

90. Mironov V, Kasyanov V, Zheng Shu X, et al. Fabrication of tubular tissue constructs by centrifugal casting of cells suspended in an in situ crosslinkable hyaluronan-gelatin hydrogel. *Biomaterials*. 2005;26(36):7628-7635. doi:10.1016/j.biomaterials.2005.05.061.

91. Pitarresi G, Palumbo FS, Calabrese R, Craparo EF, Giammona G. Crosslinked hyaluronan with a protein-like polymer: Novel bioresorbable films for biomedical applications. *J Biomed Mater Res Part A*. 2008;84A(2):413-424. doi:10.1002/jbm.a.31316.

92. Más Estellés J, Vidaurre A, Meseguer Dueñas JM, Castilla Cortázar I. Physical characterization of polycaprolactone scaffolds. *J Mater Sci Mater Med*. 2008;19(1):189-195. doi:10.1007/s10856-006-0101-2.

93. Wang T-W, Spector M. Development of hyaluronic acid-based scaffolds for brain tissue engineering. *Acta Biomater*. 2009;5(7):2371-2384. doi:10.1016/j.actbio.2009.03.033.

94. Farrell E, O'Brien FJ, Doyle P, et al. A collagen-glycosaminoglycan scaffold supports adult rat mesenchymal stem cell differentiation along osteogenic and chondrogenic routes. *Tissue Eng*. 2006;12(3):459-468. doi:10.1089/ten.2006.12.459.

95. Yang S, Leong K-F, Du Z, Chua C-K. The design of scaffolds for use in tissue engineering. Part II. Rapid prototyping techniques. *Tissue Eng*. 2002;8(1):1-11. doi:10.1089/107632702753503009.

96. Melchels FPW, Feijen J, Grijpma DW. A review on stereolithography and its applications in biomedical engineering. *Biomaterials*. 2010;31(24):6121-6130. doi:10.1016/j.biomaterials.2010.04.050.

97. Billiet T, Vandenhaute M, Schelfhout J, Van Vlierberghe S, Dubruel P. A review of trends and limitations in hydrogel-rapid prototyping for tissue engineering. *Biomaterials*. 2012;33(26):6020-6041. doi:10.1016/j.biomaterials.2012.04.050.

98. Hanemann T, Bauer W, Knitter R, Woias P. Rapid Prototyping and Rapid Tooling Techniques for the Manufacturing of Silicon, Polymer, Metal and Ceramic Microdevices. In: Leondes CT, ed. *Mems/Nems Handbook : Techniques and Applications*. ; 2006:801-869.

99. Guo R, Lu S, Page JM, et al. Fabrication of 3D Scaffolds with Precisely Controlled Substrate Modulus and Pore Size by Templated-Fused Deposition Modeling to Direct Osteogenic Differentiation. *Adv Healthc Mater*. 2015;4(12):1826-1832. doi:10.1002/adhm.201500099.

100. Chia HN, Wu BM. Recent advances in 3D printing of biomaterials. *J Biol Eng*. 2015;9(1):4. doi:10.1186/s13036-015-0001-4.

101. Hamid Q, Snyder J, Wang C, et al. Fabrication of three-dimensional scaffolds using precision extrusion deposition with an assisted cooling device. *Biofabrication*. 2011;3(3):34109. doi:10.1088/1758-5082/3/3/034109.

102. Darling AL, Sun W. 3D microtomographic characterization of precision extruded poly-epsilon-caprolactone scaffolds. *J Biomed Mater Res B Appl Biomater*. 2004;70(2):311-317. doi:10.1002/jbm.b.30050.

103. Whatley BR, Kuo J, Shuai C, Damon BJ, Wen X. Fabrication of a biomimetic elastic intervertebral disk scaffold using additive manufacturing. *Biofabrication*. 2011;3(1):015004. doi:10.1088/1758-5082/3/1/015004.

104. Chee Kai Chua, Kah Fai Leong CSL. *Rapid Prototyping : Principles and Applications*. World Scientific; 2010.

105. Geiger M, Steger W, Greul M, Sindel M. Multiphase Solidification - a new process towards metal prototypes and a new data interface. *Fraunhofer*. 1994:9-16.

106. Greulich M, Greul M, Pintat T. Fast, functional prototypes via multiphase jet solidification. *Rapid Prototyp J*. 1995;1(1):20-25. doi:10.1108/13552549510146649.

107. Moroni L, Schotel R, Hamann D, de Wijn JR, van Blitterswijk CA. 3D Fiber-Deposited Electrospun Integrated Scaffolds Enhance Cartilage Tissue Formation. *Adv Funct Mater*. 2008;18(1):53-60. doi:10.1002/adfm.200601158.

108. Moroni L. A Mechanistic Approach to Design Smart Scaffolds for Tissue Engineering. 2006. http://doc.utwente.nl/57610/.

109. Vozzi G, Ahluwalia A. Microfabrication for tissue engineering: rethinking the cells-on-a scaffold approach. *J Mater Chem*. 2007;17(13):1248. doi:10.1039/b613511k.

110. Xiong Z. Fabrication of porous scaffolds for bone tissue engineering via low-temperature deposition. *Scr Mater*. 2002;46(11):771-776. doi:10.1016/S1359-6462(02)00071-4.

111. Wei Xu, Xiao Wang, Yongnian Yan, Renji Zhang. Rapid Prototyping of Polyurethane for the Creation of Vascular Systems. *J Bioact Compat Polym*. 2008;23(March 2008):103-114. doi:10.1177/0883911507088271.

112. Khalil S, Nam J, Sun W. Multi-nozzle deposition for construction of 3D biopolymer tissue scaffolds. *Rapid Prototyp J*. 2005;11(1):9-17. doi:10.1108/13552540510573347.

113. Sachlos E, Czernuszka JT. Making tissue engineering scaffolds work. Review: the application of solid freeform fabrication technology to the production of tissue engineering scaffolds. *Eur Cells Mater*. 2003;5:29-40.

114. Landers R, Mülhaupt R. Desktop manufacturing of complex objects, prototypes and biomedical scaffolds by means of computer-assisted design combined with computer-guided 3D plotting of polymers and reactive oligomers. *Macromol Mater Eng*. 2000;282(Llm):17-21. doi:10.1002/1439-2054(20001001)282:1<17::AID-MAME17>3.0.CO;2-8.

115. Cesarano J. A review of robocasting technology. In: *Symposium V - Solid Freeform and Additive Fabrication a Materials*. Vol 542. ; 1998:133-139. doi:10.1557/PROC-542-133.

116. Liu W, Li Y, Liu J, Niu X, Wang Y, Li D. Application and performance of 3D printing in nanobiomaterials. *J Nanomater*. 2013;2013. doi:10.1155/2013/681050.

117. Ilkhanizadeh S, Teixeira AI, Hermanson O. Inkjet printing of macromolecules on hydrogels to steer neural stem cell differentiation. *Biomaterials*. 2007;28(27):3936-3943. doi:10.1016/j.biomaterials.2007.05.018.

118. Boland T, Tao X, Damon BJ, et al. Drop-on-demand printing of cells and materials for designer tissue constructs. *Mater Sci Eng C*. 2007;27(3):372-376. doi:10.1016/j.msec.2006.05.047.

119. Sun J, Ng J, Fuh Y, Wong Y, Loh H, Xu Q. Comparison of micro-dispensing performance between micro-valve and piezoelectric printhead. *Microsyst Technol*. 2009;15(9):1437-1448. doi:10.1007/s00542-009-0905-3.

120. Leong KF, Chua CK, Gui WS, Verani. Building porous biopolymeric microstructures for controlled drug delivery devices using selective laser sintering. *Int J Adv Manuf Technol*. 2006;31(5-6):483-489. doi:10.1007/s00170-005-0217-4.

121. Narayan RJ. *Rapid Prototyping of Biomaterials: Principles and Applications*.; 2014. http://www.scopus.com/inward/record.url?eid=2-s2.0-84904083797&partnerID=40&md5=8e82f5b68ff8b640edc24fae608fd555.

122. Ikuta K, Hirowatari K. Real three dimensional micro fabrication using stereo lithography and metal molding. *Proc IEEE Micro Electro Mech Syst Conf*. 1993:42-47. doi:10.1109/MEMSYS.1993.296949.

123. Ikuta K, Maruo S, Kojima S. New micro stereo lithography for freely movable 3D micro structure-super IH process with submicron resolution. In: *MEMS 98. Proceedings., The Eleventh Annual International Workshop on*. ; 1998:290-295. doi:10.1109/MEMSYS.1998.659770.

124. Yeong W-Y, Chua C-K, Leong K-F, Chandrasekaran M. Rapid prototyping in tissue engineering: challenges and potential. *Trends Biotechnol*. 2004;22(12):643-652. doi:http://dx.doi.org/10.1016/j.tibtech.2004.10.004.

125. Sachs E, Cima M, Cornie J. Three-Dimensional Printing: Rapid Tooling and Prototypes Directly from a CAD Model. *CIRP Ann - Manuf Technol*. 1990;39(1):201-204. doi:10.1016/S0007-8506(07)61035-X.

126. Bak TM. Two photon Microstereolithography of polymers for tissue engineering. 2009. doi:10.3990/1.9789036528471.

127. LaFratta CN, Fourkas JT, Baldacchini T, Farrer R a, Christopher N. LaFratta, John T. Fourkas, Tommaso Baldacchini and RAF. Multiphoton fabrication. *Angew Chem Int Ed Engl*. 2007;46(33):6238-6258. doi:10.1002/anie.200603995.

128. Sun H-B, Kawata S. Two-Photon Photopolymerization and 3D Lithographic Microfabrication. 2006:169-273. doi:10.1007/b94405.

129. Xing J-F, Dong X-Z, Chen W-Q, et al. Improving spatial resolution of two-photon microfabrication by using photoinitiator with high initiating efficiency. *Appl Phys Lett*. 2007;90(13):131106-131106 - 3. doi:doi:10.1063/1.2717532.

130. Pao Y, Rentzepis PM. Laser induced production of free radicals in organic compounds. *Appl Phys Lett*. 1965;6(5).

131. Maruo S, Nakamura O, Kawata S. Three-dimensional microfabrication with two-photon-absorbed photopolymerization. *Opt Lett*. 1997;22(2):132-134. doi:10.1364/OL.22.000132.

132. Strickler JH, Webb WW. Two-photon excitation in laser scanning fluorescence microscopy. In: Vol 1398. ; 1991:107-118. http://dx.doi.org/10.1117/12.47787.

133. Wu E-S, Strickler JH, Harrell WR, Webb WW. Two-photon lithography for microelectronic application. In: Vol 1674. ; 1992:776-782. http://dx.doi.org/10.1117/12.130367.

134. Göppert-Mayer M. Uber Elementarakte mit zwei Quantensprüngen. *Ann Phys*. 1931;401(3):273-294. doi:10.1002/andp.19314010303.

135. Kaiser W, Garrett C. Two-Photon Excitation in CaF2: Eu2+. *Phys Rev Lett*. 1961;7(6):229-231. doi:10.1103/PhysRevLett.7.229.

136. Rocheleau J V, Piston DW. Two-photon excitation microscopy for the study of living cells and tissues. *Curr Protoc Cell Biol*. 2003;Chapter 4:Unit 4.11. doi:10.1002/0471143030.cb0411s20.

137. Correa DS, Boni L De, Otuka AJG, Tribuzi V, Mendonça CR. Two-Photon Polymerization Fabrication of Doped Microstructures. In: Gomes ADS, ed. *Polymerization*. Intechopen; 2012:333-356. doi:10.5772/36061.

138. Denk W, Piston DW, Watt W. W. Two-Photon Molecular Excitation in Laser-Scanning Microscopy. In: *Handbook of Biological Confocal Microscopy*. ; 1995:445-458.

139. Peřina J, Saleh B, Teich M. Multiphoton absorption cross section and virtual-state spectroscopy for the entangled n-photon state. *Phys Rev A*. 1998;57(5):3972-3986. doi:10.1103/PhysRevA.57.3972.

140. Three-Dimensional Microfabrication by two photon polymerization. *Newport Corp Technol Appl Cent*.

141. Raimondi MT, Eaton SM, Nava MM, Laganà M, Cerullo G, Osellame R. Two-photon laser polymerization: from fundamentals to biomedical application in tissue engineering and regenerative medicine. *J Appl Biomater Biomech*. 2012;(June):0-0. doi:10.5301/JABB.2012.9249.

142. Levinson HJ. *Principles of Lithography 3rd Ed*. SPIE Press; 2011.

143. Chichkov BN, Ostendorf A. Two-Photon Polymerization: A New Approach to Micromachining. *Photonics Spectra*. 2006;40(October):72-79.

144. Tan D, Li Y, Qi F, et al. Reduction in feature size of two-photon polymerization using SCR500. *Appl Phys Lett*. 2007;90(7):071106. doi:10.1063/1.2535504.

145. Cao H-Z, Zheng M-L, Dong X-Z, Jin F, Zhao Z-S, Duan X-M. Two-photon nanolithography of positive photoresist thin film with ultrafast laser direct writing. *Appl Phys Lett*. 2013;102(20):201108. doi:10.1063/1.4807678.

146. Decker C. The use of UV irradiation in polymerization. *Polym Int*. 1998;45(2):133-141. doi:10.1002/(SICI)1097-0126(199802)45:2<133::AID-PI969>3.0.CO;2-F.

147. Watanabe T, Akiyama M, Totani K, et al. Photoresponsive Hydrogel Microstructure Fabricated by Two-Photon Initiated Polymerization. *Adv Funct Mater*. 2002;12(9):611-614. doi:10.1002/1616-3028(20020916)12:9<611::AID-ADFM611>3.0.CO;2-3.

148. Coenjarts CA, Ober CK. Two-Photon Three-Dimensional Microfabrication of Poly(Dimethylsiloxane) Elastomers. *Chem Mater*. 2004;16(26):5556-5558. doi:10.1021/cm048717z.

149. Serbin J, Egbert A, Ostendorf A, et al. Femtosecond laser-induced two-photon polymerization of inorganic--organic hybrid materials for applications in photonics. *Opt Lett*. 2003;28(5):301-303. doi:10.1364/OL.28.000301.

150. Serbin J, Ovsianikov A, Chichkov B. Fabrication of woodpile structures bytwo-photon polymerization and investigation of their optical properties. *Opt Express*. 2004;12(21):5221-5228. doi:10.1364/OPEX.12.005221.

151. Torres-Filho A, Neckers DC. Mechanical properties of acrylate networks formed by visible laser-induced polymerization. I. Dependence on photopolymerization parameters. *J Appl Polym Sci*. 1994;51(5):931-937. doi:10.1002/app.1994.070510515.

152. Pitts JN, Hammond GS, Gollnick K. *Advances in Photochemistry*.; 2009.

153. Odian G, Group F. *Principles of Polymerization, 4th Edition*. Wiley Subscription Services, Inc., A Wiley Company; 2004.

154. Fouassier J. *Photoinitiation, Photopolymerization, and Photocuring : Fundamentals and Applications*. Hanser Publishers; 1995.

155. Schafer KJ, Hales JM, Balu M, Belfield KD, Van Stryland EW, Hagan DJ. Two-photon absorption cross-sections of common photoinitiators. *J Photochem Photobiol A Chem*. 2004;162(2-3):497-502. doi:10.1016/S1010-6030(03)00394-0.

156. Born M, Wolf E. *Principles of Optics 7th Ed*. Press Syndicate of the university of cambridge; 2003.

157. Matsumoto K. STM/AFM nano-oxidation process to room-temperature-operated single-electron transistor and other devices. *Proc IEEE*. 1997;85(4):612-628. doi:10.1109/5.573745.

158. Sauer BB, McLean RS, Thomas RR. Tapping Mode AFM Studies of Nano-Phases on Fluorine-Containing Polyester Coatings and Octadecyltrichlorosilane Monolayers. *Langmuir*. 1998;14(11):3045-3051. doi:10.1021/la971334d.

159. Betzig E, Trautman JK. Near-field optics: microscopy, spectroscopy, and surface modification beyond the diffraction limit. *Science*. 1992;257(5067):189-195. doi:10.1126/science.257.5067.189.

160. Tsai Y-C, Leitz K-H, Fardel R, Schmidt M, Arnold CB. Generating Nanostructures with Multiphoton Absorption Polymerization using Optical Trap Assisted Nanopatterning. *Phys Procedia*. 2012;39:669-673. doi:10.1016/j.phpro.2012.10.087.

161. Juodkazis S, Mizeikis V, Seet KK, Miwa M, Misawa H. Two-photon lithography of nanorods in SU-8 photoresist. *Nanotechnology*. 2005;16(6):846. doi:10.1088/0957-4484/16/6/039.

162. Sun HB, Takada K, Kim MS, Lee KS, Kawata S. Scaling laws of voxels in two-photon photopolymerization nanofabrication. *Appl Phys Lett*. 2003;83(2003):1104-1106. doi:10.1063/1.1599968.

163. Haberko J, Scheffold F. Fabrication of mesoscale polymeric templates for three-dimensional disordered photonic materials. *Opt Express*. 2013;21(1):1057-1065. doi:10.1364/OE.21.001057.

164. Brüser B, Staude I, von Freymann G, Wegener M, Pietsch U. Visible light Laue diffraction from woodpile photonic crystals. *Appl Opt*. 2012;51(28):6732. doi:10.1364/AO.51.006732.

165. Xiong X, Jiang SC, Hu YH, Peng RW, Wang M. Structured metal film as a perfect absorber. *Adv Mater*. 2013;25(29):3994-4000. doi:10.1002/adma.201300223.

166. Nawrot M, Zinkiewicz \Lukasz, W\lodarczyk B, Wasylczyk P, Zinkiewicz Ł. Transmission phase gratings fabricated with direct laser writing as color filters in the visible. *Opt Express*. 2013;21(26):31919-31924. doi:10.1364/OE.21.031919.

167. Schröder M, Bülters M, von Kopylow C, Bergmann RB. Novel concept for three-dimensional polymer waveguides for optical on-chip interconnects. *J Eur Opt Soc*. 2012;7:8-11. doi:10.2971/jeos.2012.12027.

168. Lindenmann N, Balthasar G, Hillerkuss D. Photonic Wire Bonds for Terabit/s Chip-to-Chip Interconnects. *Phys Opt*. 2011:1-8. http://arxiv.org/abs/1111.0651.

169. Jang D, Meza LR, Greer F, Greer JR. Fabrication and deformation of three-dimensional hollow ceramic nanostructures. *Nat Mater*. 2013;12(10):893-898. doi:10.1038/nmat3738.

170. Yeh C, Boyce JB, Ho J, Lau R. Fabrication of Mechanical Microstructures Using Amorphous Silicon Films on Glass Substrates. *MRS Online Proc Libr*. 2000;609:null - null.

171. Lee WC, Heo YJ, Takeuchi S. Wall-Less Microfluidic Channels Using 3-Dimemsional Ring Arrays. *Miniaturized Syst Chem Life Sci*. 2012:296-298.

172. Kim S, Qiu F, Kim S, et al. Fabrication and characterization of magnetic microrobots for three-dimensional cell culture and targeted transportation. *Adv Mater*. 2013;25(41):5863-5868. doi:10.1002/adma.201301484.

173. Pins GD, Bush KA, Cunningham LP, Campagnola PJ. Multiphoton excited fabricated nano and micro patterned extracellular matrix proteins direct cellular morphology. *J Biomed Mater Res A*. 2006;78(1):194-204. doi:10.1002/jbm.a.30680.

174. Basu S, Rodionov V, Terasaki M, Campagnola PJ. Multiphoton-excited microfabrication in live cells via Rose Bengalcross-linking of cytoplasmic proteins. *Opt Lett*. 2005;30(2):159-161. doi:10.1364/OL.30.000159.

175. Greiner AM, Jäckel M, Scheiwe AC, et al. Multifunctional polymer scaffolds with adjustable pore size andchemoattractant gradients for studying cell matrix invasion. *Biomaterials*. 2014;35(2):611-619. doi:10.1016/j.biomaterials.2013.09.095.

176. Greiner AM, Richter B, Bastmeyer M. Micro-Engineered 3D Scaffolds for Cell Culture Studies. *Macromol Biosci*. 2012;12(10):1301-1314. doi:10.1002/mabi.201200132.

177. Wittig R, Waller E, von Freymann G, Steiner R. Direct laser writing-mediated generation of standardized topographies for dental implant surface optimization. *J Laser Appl*. 2012;24(4):042011. doi:10.2351/1.4728135.

178. Farsari M, Chichkov BN. Materials processing: Two-photon fabrication. *Nat Photonics*. 2009;3(8):450-452. doi:10.1038/nphoton.2009.131.

179. Dalby MJ, Gadegaard N, Tare R, et al. The control of human mesenchymal cell differentiation using nanoscale symmetry and disorder. *Nat Mater*. 2007;6(12):997-1003. doi:10.1038/nmat2013.

180. Dalby MJ, Gadegaard N, Oreffo ROC. Harnessing nanotopography and integrin-matrix interactions to influence stem cell fate. *Nat Mater*. 2014;13(6):558-569. doi:10.1038/nmat3980.

181. Nanoscribe GmbH. Photonic Professional User Maual. 2012;(May). www.nanoscribe.de.

182. Koroleva A, Gill AA, Ortega I, et al. Two-photon polymerization-generated and micromolding-replicated 3D scaffolds for peripheral neural tissue engineering applications. *Biofabrication*. 2012;4(2):025005. doi:10.1088/1758-5082/4/2/025005.

183. Koroleva A, Schlie S, Fadeeva E, et al. Microreplication of laser-fabricated surface and three-dimensional structures. *J Opt*. 2010;12(12):124009. doi:10.1088/2040-8978/12/12/124009.

184. Rezende RA, Pereira FDAS, Kasyanov V, et al. Design, physical prototyping and initial characterisation of `lockyballs'. *Virtual Phys Prototyp*. 2012;7(4):287-301. doi:10.1080/17452759.2012.740877.

185. Obata K, El-Tamer A, Koch L, Hinze U, Chichkov BN. High-aspect 3D two-photon polymerization structuring with widened objective working range (WOW-2PP). *Light Sci Appl*. 2013;2(August):e116. doi:10.1038/lsa.2013.72.

186. Kaiser J-P, Reinmann A, Bruinink A. The effect of topographic characteristics on cell migration velocity. *Biomaterials*. 2006;27(30):5230-5241. doi:10.1016/j.biomaterials.2006.06.002.

187. Chen CS, Mrksich M, Huang S, Whitesides GM, Ingber DE. Geometric control of cell life and death. *Science*. 1997;276(5317):1425-1428. doi:10.1126/science.276.5317.1425.

188. Unadkat H V, Hulsman M, Cornelissen K, et al. An algorithm-based topographical biomaterials library to instruct cell fate. *Proc Natl Acad Sci U S A*. 2011;108(40):16565-16570. doi:10.1073/pnas.1109861108.

189. Jeon H, Hidai H, Hwang DJ, Grigoropoulos CP. Fabrication of arbitrary polymer patterns for cell study by two-photon polymerization process. *J Biomed Mater Res Part A*. 2009;9999A:NA - NA. doi:10.1002/jbm.a.32517.

190. Lindström S, Andersson-Svahn H. Overview of single-cell analyses: microdevices and applications. *Lab Chip*. 2010;10(24):3363. doi:10.1039/c0lc00150c.

191. Altschuler SJ, Wu LF. Cellular Heterogeneity: Do Differences Make a Difference? *Cell*. 2010;141(4):559-563. doi:10.1016/j.cell.2010.04.033.

192. Coussens LM, Fingleton B, Matrisian LM. Matrix metalloproteinase inhibitors and cancer: trials and tribulations. *Science*. 2002;295(5564):2387-2392. doi:10.1126/science.1067100.

193. Yuan H, Fernandes H, Habibovic P, et al. Osteoinductive ceramics as a synthetic alternative to autologous bone grafting. *Proc Natl Acad Sci*. 2010;107(31):13614-13619. doi:10.1073/pnas.1003600107.

194. Gonsalves K, Halberstadt C, Laurencin CT, (Editor) LN, eds. *Biomedical Nanostructures*. John Wiley & Sons, Ltd.; 2007.

195. Wu S, Serbin J, Gu M. Two-photon polymerisation for three-dimensional micro-fabrication. *J Photochem Photobiol A Chem*. 2006;181(1):1-11. doi:10.1016/j.jphotochem.2006.03.004.

196. Straub M, Nguyen LH, Fazlic A, Gu M. Complex-shaped three-dimensional microstructures and photonic crystals generated in a polysiloxane polymer by two-photon microstereolithography. *Opt Mater (Amst)*. 2004;27(3):359-364. doi:10.1016/j.optmat.2004.07.013.

197. Kim W-S, Houbertz R, Lee T-H, Bae B-S. Effect of photoinitiator on photopolymerization of inorganic-organic hybrid polymers (ORMOCER). *J Polym Sci Part B Polym Phys*. 2004;42(10):1979-1986. doi:10.1002/polb.20063.

198. White TJ, Liechty WB, Guymon CA. The Influence of N-Vinyl Pyrrolidone on Polymerization Kinetics and Thermo-Mechanical Properties of Crosslinked Acrylate Polymers. *J Polym Sci Part a-Polymer Chem*. 2007;45:4062-4073. doi:10.1002/pola.22173.

199. Granchak V. M, Kondratenko PA, Sherstyuk VP, Dilung II. Mechanism of Polymerization of Vinyl Monomers initiated by Benzophenone and its Derivatives. *Polym Sci*. 1980;22(8):2045-2052.

200. Guthrie J, Jeganathan MB, Otterburn MS, Woods J. Light screening effects of photoinitiators in UV curable systems. *Polym Bull*. 1986;15:51-58. doi:10.1007/BF00263492.

201. Sabnis AR. Cytotoxic evaluation and factorial analysis of three-dimensional photopolymerizable thermoresponsive composite nanoparticle hydrogels for controlled drug delivery in restenosis and wound healing. 2007. http://search.proquest.com/docview/304707768.

202. Williams CG, Malik AN, Kim TK, Manson PN, Elisseeff JH. Variable cytocompatibility of six cell lines with photoinitiators used for polymerizing hydrogels and cell encapsulation. *Biomaterials*. 2005;26(11):1211-1218. doi:10.1016/j.biomaterials.2004.04.024.

203. Nanoscribe. Data sheet - Photonic Professional GT. http://www.nanoscribe.de/files/8414/3798/6567/DataSheet_Photonic_Professional_GT.pdf. Accessed April 5, 2015.

204. Nanoscribe. Data sheet - Photonic Professional. http://www.nanoscribe.de/files/7914/0169/2326/DataSheet_Photonic_Professional.pdf. Accessed April 5, 2015.

205. Jipa F, Marian Zamfirescu, Velea A, Popescu M, Dabu R. Femtosecond Laser Lithography in Organic and Non-Organic Materials. In: Sumi P, ed. *Updates in Advanced Lithography*. Intech; 2013:65-94. doi:10.5772/56579.

APPENDIX

16.1. FLUORESCENCE SPECTRA

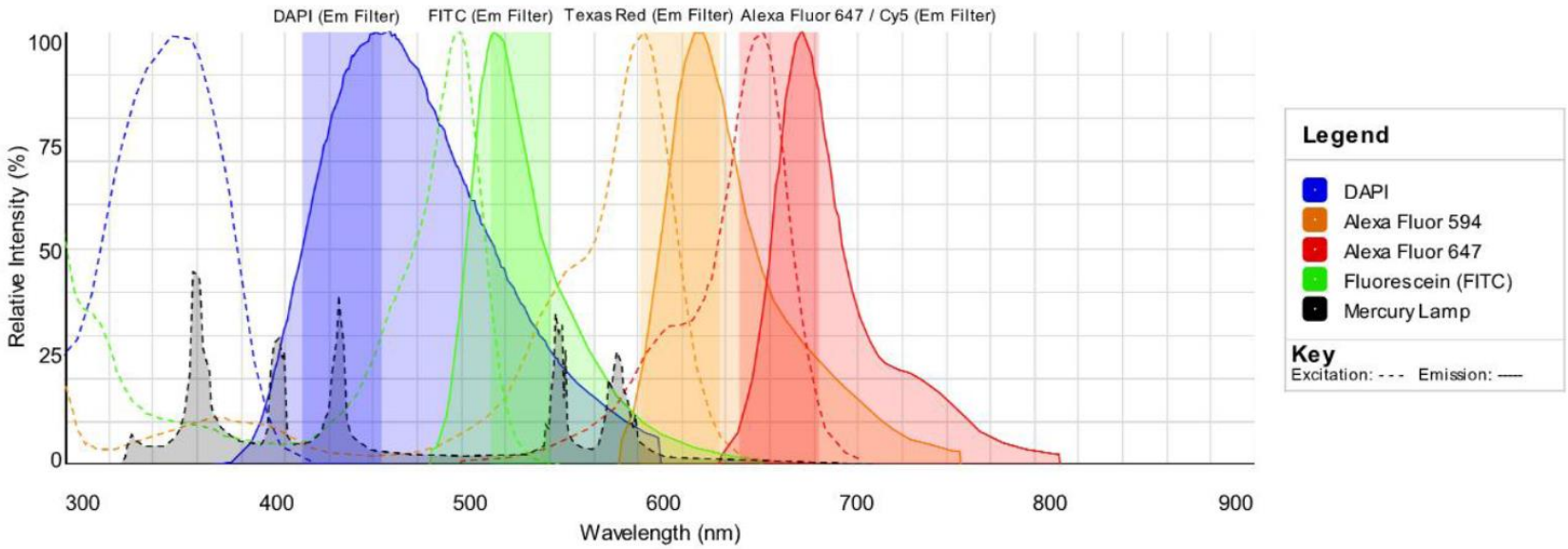

Figure 45 - Excitation and emission spectra of fluorophores used for staining. Emission spectrum of the mercury lamp used in the fluorescence microscope. Filters used for imaging of different fluorophores. Source: https://www.thermofisher.com/pt/en/home/life-science/cell-analysis/labeling-chemistry/fluorescence-spectraviewer.html?ICID=svtool&UID=3585dna

16.2. WHITE LIGHT INTERFEROMETER HEAT MAPS AND GRAPHICS FOR POLYSTYRENE

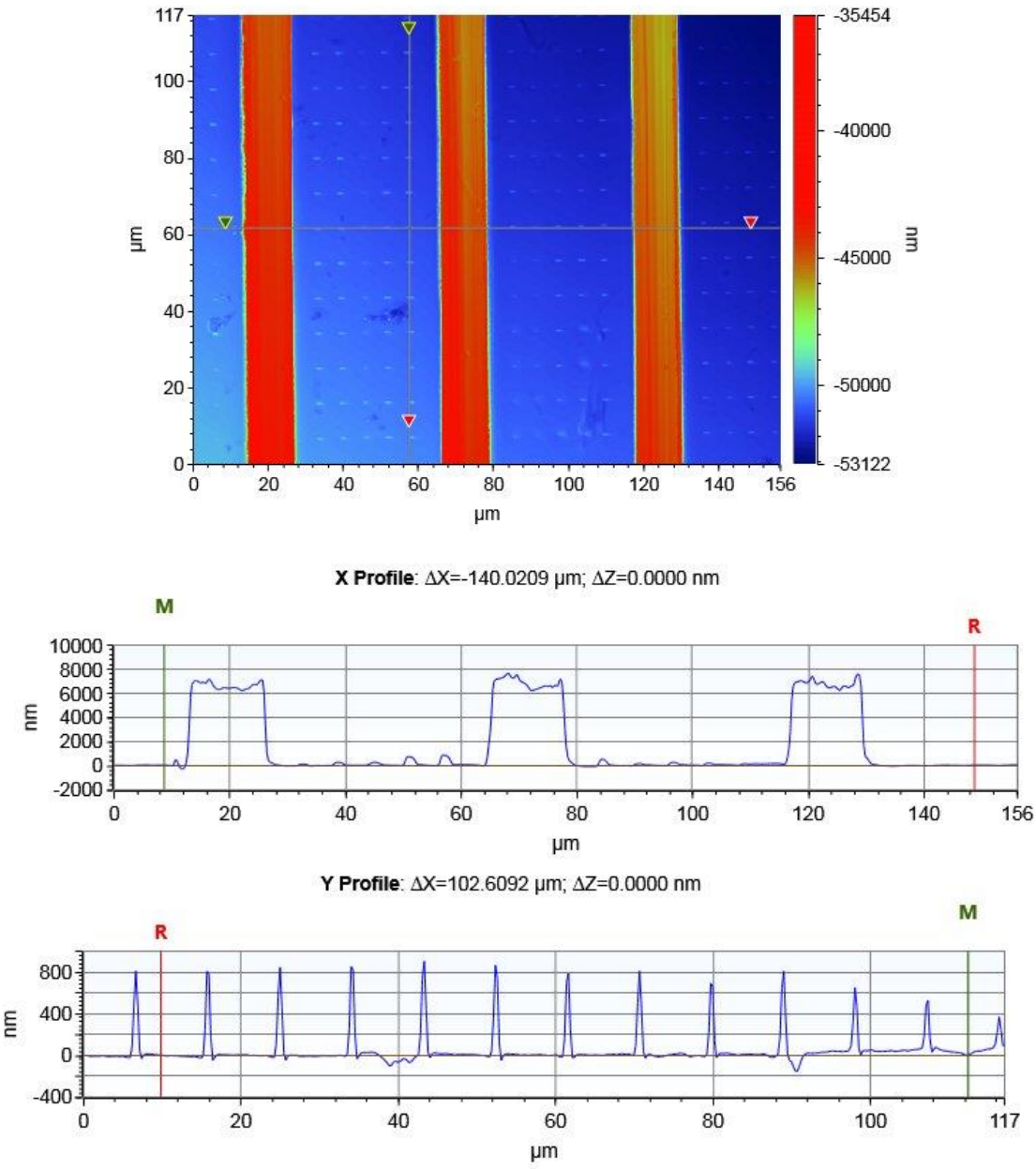

Figure 46 – Heat map and peak graphics obtained by white light interferometry for a Polystyrene imprint.

16.3. WHITE LIGHT INTERFEROMETER HEAT MAPS AND GRAPHICS FOR POLY(LACTIC) ACID

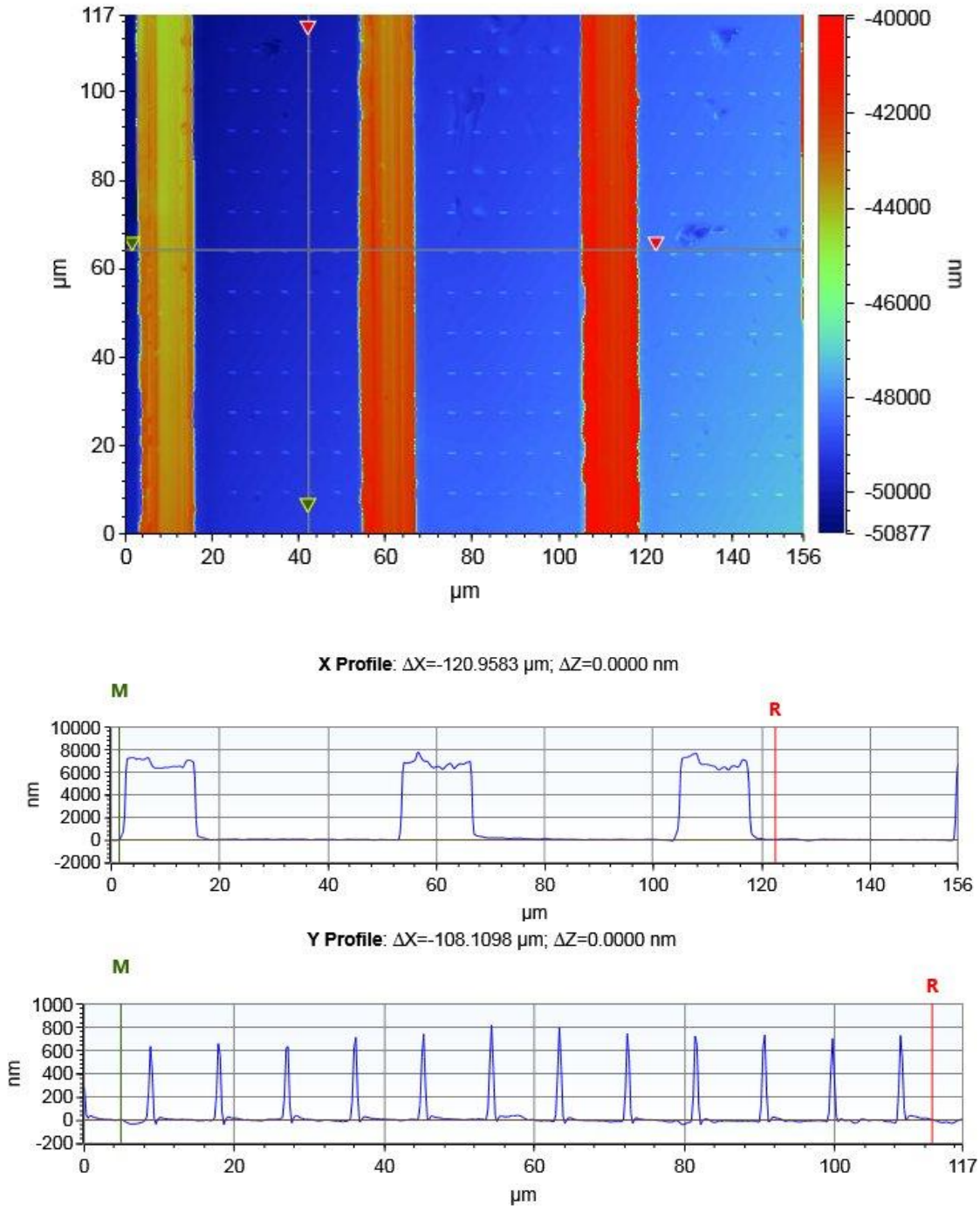

Figure 47 - Heat map and peak graphics obtained by white light interferometry for a Poly(lactic) acid imprint.

16.4. ABSORPTION SPECTRA FOR IRGACURE 2959

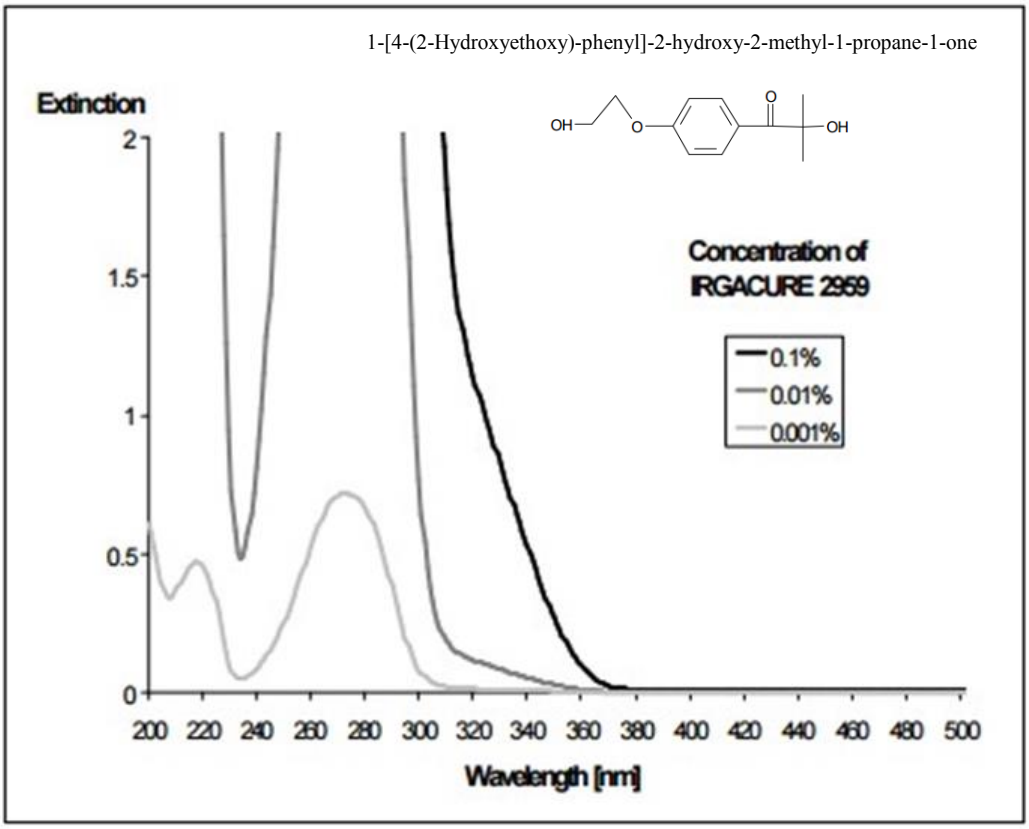

Figure 48 - Absorption Specta (% in Acetonitrile) of Irgacure 2959 photoinitiator, from Ciba Specialty Chemicals. Source: http://www.xtgchem.cn/upload/20110629045632.PDF

16.5. ABSORPTION SPECTRA FOR BENZOPHENONE DERIVATIVE

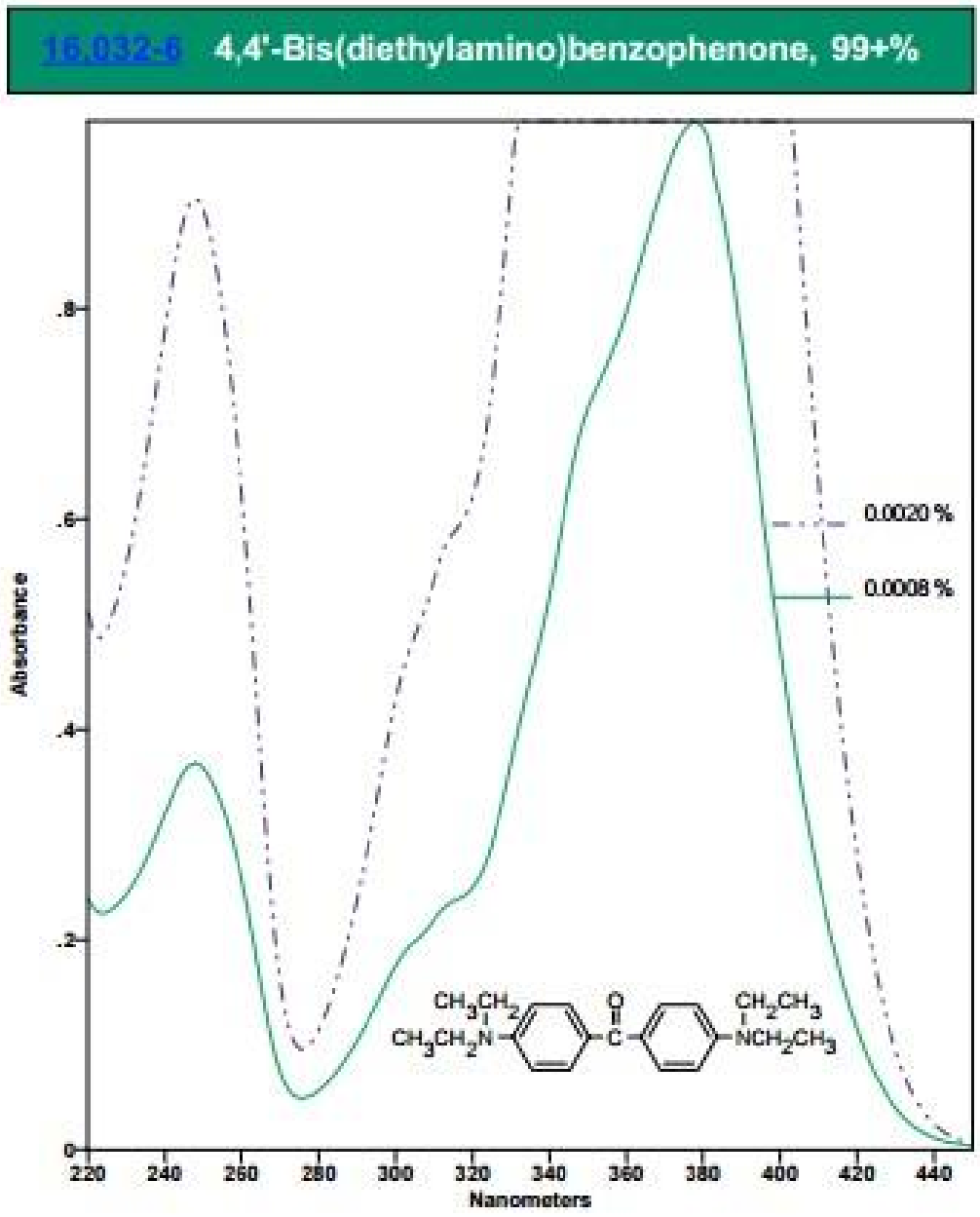

Figure 49 – Absorption spectra of 4,4'-Bis(diethylamino)benzophenone photoinitiator from Sigma-aldrich. Source: https://www.sigmaaldrich.com/content/dam/sigma-ldrich/docs/Aldrich/General_Information/photoinitiators.pdf